Towards CMUT for Neurostimulation

30-11-2020

Eric Dijkema

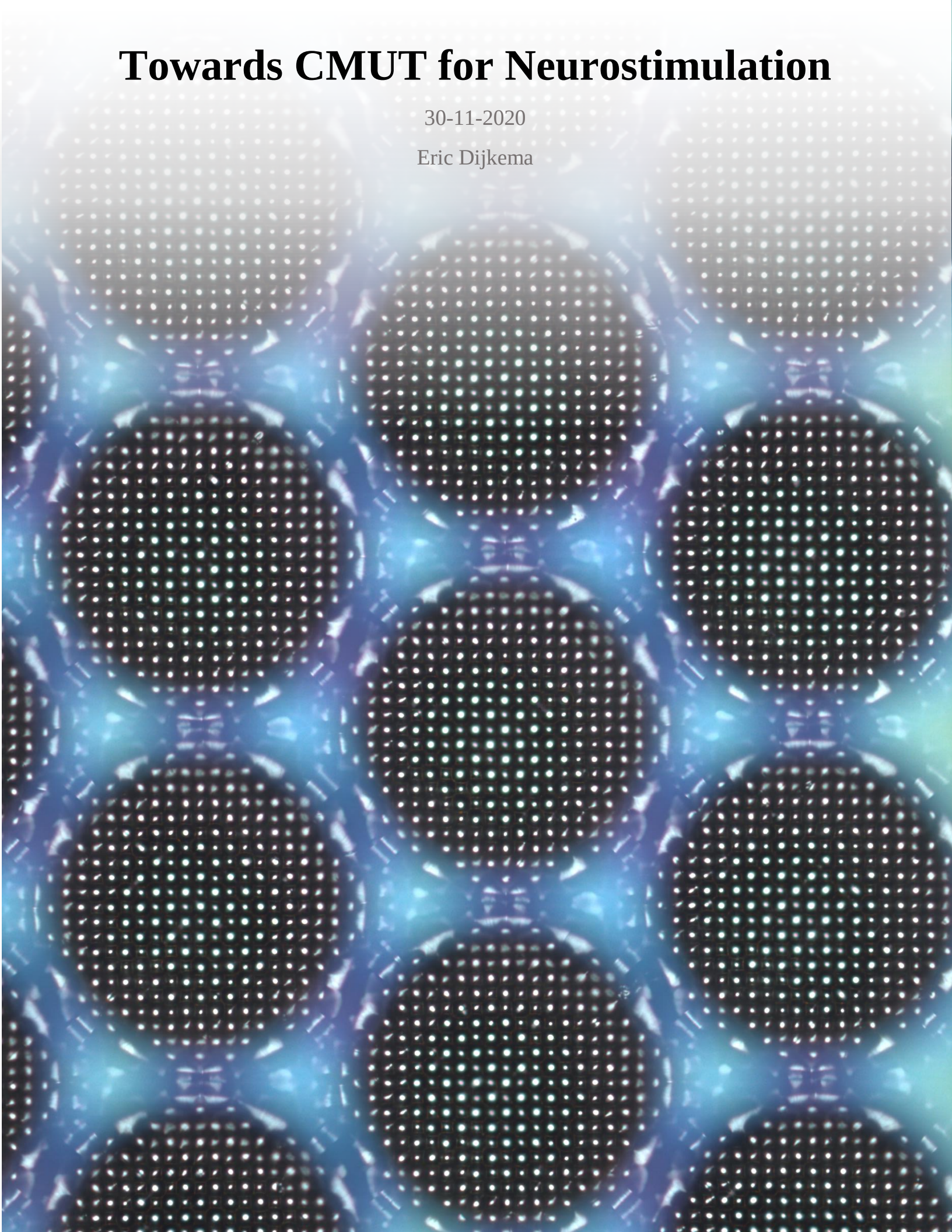

Towards CMUT for Neurostimulation

A thesis about

The Development of an Experimental Model for the Validation of Ultrasound Neuromodulation

and

Back-side Vent Etching for Low-Frequency CMUT Devices

Written by

Eric Dijkema, 4968875

For the completion of the requirements for an MSc degree in

Biomedical Engineering, Medical Devices and Bioelectronics

under the supervision of

prof.dr.ir. Ronald Dekker

Graduation Committee

prof.dr.ir. R. Dekker

prof.dr. P.J. French

dr. V. Giagka

dr. Massimo Mastrangeli

Abbreviations

AP	Action Potential
CAP	Compound Action Potentials
CMUT	Capacitive Micromachined Ultrasound Transducer
DC	Duty Cycle
eCAP	Evoked Compound Action Potential
EEG	Electroencephalography
EMG	Electromyography
fMRI	Functional Magnetic Resonance Imaging
FUS	Focused Ultrasound Stimulation
HIFU	High Intensity Focus Ultrasound
I_{SPPA}	Spatial Peak Point Average Intensity
I_{SPTA}	Spatial Peak Temporal Average Intensity
LIFU	Low Intensity Focused Ultrasound
LILFU	Low Intensity Low Frequency Focused Ultrasound
MEMS	Micromachined Electromechanical System
MI	Mechanical Index
PRF	Pulse Repetition Frequency
PZT	Lead-Zirconate-Titanate
t-FUS	Transcranial Focused Ultrasound Stimulation
VEP	Visually Evoked Potential
US	Ultrasound

Abstract

Ultrasound (US) neurostimulation, the non-pharmacological, reversible excitation or inhibition of the nervous system using ultrasonic waves, is emerging as a high interest topic in neurostimulation research. In the current project, an attempt was made to demonstrate US neuromodulation in a *Lumbricus Terrestris* model of evoked compound action potentials (eCAP). Hardware and software for the electrophysiological observation of local field potentials were designed and assembled. The resulting system was used to perform mechanical, electrical and both direct and indirect ultrasonic neurostimulation experiments. It was shown electrical stimulation could be performed reliably *in-vivo* and *ex-vivo*. Mechanical stimulation only functioned *in-vivo.* Additionally, power transfer experiments showed that deeply embedded CMUT devices can be used to harvest acoustic power and use this signal to stimulate an explanted *Lumbricus Terrestris* medial nerve cord. Direct ultrasound neurostimulation was however not observed, likely due to a combination of misalignment and incorrect acoustic pressure profiles.

As an additional project, a microfabrication step was designed and performed for the etching of high aspect-ratio silicon bulk structures for the backside venting of low frequency CMUT devices. A two-step process deep reactive ion etch (DRIE) was attempted where smaller features were first introduced into the silicon (phase A) and then advanced using a larger etch frame (phase B). It was shown that phase A etching could be performed adequately, resulting in high quality deep silicon etch profiles with minimal tapering and an excellent etch rate. However, phase B etching resulted in the consumption of side-walls and removal of previously etched features. It is likely some slight adjustments to the passivation stage of the DRIE process would result in successful completion of this fabrication step.

Acknowledgements

First and foremost, I would like to thank Ronald Dekker for presenting me with the opportunity to work under his supervision for this year. It was a pleasure to come to Eindhoven and work at Philips. For the most part, Shinnosuke Kawasaki functioned as my daily supervisor, and I want to thank him for the guidance and lessons in electronics he has provided me with. His modifications to the recording electronics circuitry and design of the PCBs were essential for creating a functional device. Sparring session with him have generated many of the ideas presented here, and I wish him a flawless continuation of his doctoral research. Concerning the work I have done in the cleanroom, Eugene Timmering and Jian Li have been indispensable. They were both willing to go out of their way to help me learn new skills and solve practical problems, something I am very grateful for. Finally, I want to thank all the interns at Philips I have met during this period, both within and outside the department of Microsystems and Devices. Youri, Joshua, Sevda, Indu, Dino, Gayatri, Jia, Katerina and Marta were wonderful to have around. Being able to share both moments of struggle and success with them truly made this year a memorable experience.

Contents

Towards CMUT for Neurostimulation **2**
Abbreviations 3
Abstract **4**
Acknowledgements **4**
Contents **5**
List of Figures and Tables **7**
Introduction **9**
Background and Justification **12**
Theory of Ultrasound 12
Ultrasound Parameters *12*
Ultrasound Neuromodulation Mechanisms of Action 14
Mechanical Activation *14*
Thermal Inhibition *15*
Parametric Observations *15*
Research Models for US Neuromodulation 16
Animal Studies *16*
Human Studies *16*
Methods **17**
Lumbricus Terrestris as a Neural Model for Evoked Compound Action Potentials *17*
Handling of Lumbricus Terrestris *18*
Medial Nerve Cord Explantation Protocol *18*
Electrical Stimulation as Verification Method *19*
Recording Electrophysiological Responses *20*
Digitization and Software *21*
***In-vivo* Experiments** **23**
Methods 23
Stimulation Protocol *23*
Results 25
Mechanical Stimulation *25*
Electrical Stimulation *26*
Ultrasound Stimulation *26*

Incorporating Experimental Insights into Future Experiments 27
***Ex-vivo* Experiments 28**
Methods 28
Schlieren Experiments 29
Ultrasound Power Transfer 32
Results 34
Electrical Stimulation 34
Ultrasound Stimulation 35
Schlieren Imaging 35
Ultrasound Power Transfer / Indirect US Stimulation 36
Discussion 37
Through-Wafer Etching for LF-CMUT 39
Introduction to Low-Frequency CMUT 39
Methods 41
Results 44
Front Side Processing of Membrane Structures 44
Experimental Etch 1 45
Experimental Etch 2 46
Experimental Etch 3 47
Experimental Etch 4 48
Discussion 49
Conclusion 50
Appendix A: Software 51
LabVIEW code documentation 51
VI Overview 51
User Manual 52
User Interface 53
LabVIEW Code Documentation 55
Appendix B: Transducer Characterization 61
Methods 61
Intensity Measurements 61
Coupling Cone 61
Results 62
Influence of the Coupling Cone 62

1 MHz Transducer Characterization *63*
5 MHz Transducer Characterization *64*
Appendix C: Lithography Masks **66**
Appendix D: Frontside Processing Cross-sections **67**
Appendix E: Backside Processing Cross-sections **68**
References 69

List of Figures and Tables

Figure 1 – Overview of general invasiveness versus spatial resolution for neurostimulation techniques in four different physical domains. **9**
Figure 2 – Example of Philips CMUT array. **10**
Figure 3 – Example of a signal used to drive an ultrasound transducer. **13**
Figure 4 - Ultrasonication causes depolarization of neuron bilipid membranes through several mechanical mechanisms. **14**
Figure 5 - Cross-section of *Lumbricus Terrestris.* Stained with silver proteinate and magnified 100X. **17**
Figure 6 – Examples of electrical stimulation waveforms as generated by the neuroboard. **19**
Figure 7 – Schematic of the single-channel CAP recording prototype. **20**
Figure 8 – Schematic of the final design of a single neuroboard amplification channel. **21**
Figure 9 – Diagram showing all hardware parts and their connectivity used for neurostimulation experiments. **22**
Figure 10 – Photograph of *Lumbricus Terrestris* undergoing electrical stimulation trial. **23**
Figure 11 – Photographs of *in-vivo* ultrasound neurostimulation experiments. **24**
Figure 12 – Evoked CAP resulting from mechanical and electrical stimulation *in-vivo.* **25**
Figure 13 – Successful neuroboard recording of electrically evoked compound action potential in *Lumbricus Terrestris.* **26**
Figure 14 – Simplified schematic illustrating amplifier shunting used in the neuroboard prototype. **27**
Figure 15 – Photograph of explanted *Lumbricus Terrestris* medial nerve cord under ultrasonication and cross-section of acoustic coupling cone. **28**
Figure 16 – Visualization of 5 MHz ultrasound waves using Schlieren optics. **29**
Figure 17 – Photograph of Schlieren optics setup. **30**
Figure 18 – Photograph of work area for Schlieren imaging during FUS. **31**
Figure 19 – Ultrasound-to-electrical stimulation setup. **33**
Figure 20 – Example of a successful *ex-vivo* electrical stimulation trial. **34**
Figure 21 – Photographs of explanted *Lumbricus Terrestris* medial nerve cords under 1 MHz ultrasonication. **35**
Figure 22 – Successful indirect electrical stimulation trials in a *Lumbricus Terrestris* explanted medial nerve cord. **36**
Figure 23 – Cross-section view of a CMUT operating in collapse mode. **39**
Figure 24 – Micrograph of a single Philips CMUT. **40**
Figure 25 – Illustration of dry etching using the Bosch process. **41**
Figure 26 – Illustration of two-step DRIE process. **42**
Figure 27 – Micrographs of front side structures. **44**
Figure 28 – Results of first silicon deep etch (40 minutes) as SEM cross-sections. **45**
Figure 29 – Results of second silicon deep etch (40 minutes) as SEM cross-sections. **46**
Figure 30 – Results of third silicon deep etch (70 min) as SEM cross-sections. **47**
Figure 31 – Light-microscopy images of 3A structures after fourth etch experiment. **48**

Figure A.1 – UI front panel with example data. **53**
Figure A.2 – UI of stimulation tab. **54**
Figure A.3 – Settings UI. **54**
Figure A.4 – Main structure of LabVIEW program. **55**
Figure A.5 – Initialization subVI. **56**
Figure A.6 – Electrical stimulation pulse generator. **57**
Figure A.7 – Custom DAQ output. **58**
Figure A.8 – Electrical stimulation selector. **59**
Figure A.9 – Filesave subVI. **59**
Figure A.10 – Snapshot subVI. **60**
Figure B.1 – Illustration of hydrophone measurement hardware. 6**1**
Figure B.2 – Results of hydrophone measurements for 1 MHz piezoelectric transducer **62**
Figure B.3 – Results of hydrophone voltage sweep measurements (1V – 10V) for 1 MHz piezoelectric transducer. **63**
Figure B.4 – Results of hydrophone voltage sweep measurements (1V – 10V) for 5 MHz piezoelectric transducer. **64**
Figure B.5 – Results of hydrophone voltage sweep in pressure. **65**
Figure C.1 – Lithography mask drawings. **66**
Figure D.1 – Cross-section illustrations of structural front side processing steps. **67**
Figure E.1 – Cross-section illustrations of structural backside processing steps. **68**

Table 1 – FDA regulation maximum acoustic output exposure levels for diagnostic ultrasound. **13**
Table 2 – Earthworm saline recipe. **18**
Table 3 – Waveform parameter sets used for *in-vivo* US neurostimulation trials. **24**
Table 4 – Result summary of success rates for mechanical, electrical and ultrasonic stimulation modalities *in-vivo.* **25**
Table 5 - Waveform parameter sets used for *ex-vivo* US neurostimulation trials. **28**
Table 6 - Waveform parameter sets used for *ex-vivo* US neurostimulation trials in Schlieren setup. **29**
Table 7 – Result summary of success rates for electrical, ultrasonic and power transfer stimulation modalities *ex-vivo.* **34**
Table 8 – Summary of processing steps performed on front side of process wafers. **43**
Table 9 – Summary of processing steps performed on backside of all wafers. **43**
Table 10 – Recipe-specific etch rates for silicon and silicon oxide as calculated for experiment 1. ..... **45**
Table 11 – Recipe-specific etch rates for silicon and oxide as calculated from experiment 2. ..... **46**
Table 12 – Recipe-specific etch rates for silicon and oxide as calculated from experiment 3. ..... **47**

Introduction

Neuromodulation, or neurostimulation, is the external, non-pharmacological modulation of behavior of the nervous system. Considering the fact that neurons transfer information by means of action potentials, which are a manifestation of electrical, mechanical and chemical effects, neuromodulation can also be defined as the employment of physical methods to change these properties in neurons. Neuromodulation is not a novel process. The first documented case of electrical neuromodulation stems from 15 AD, when applying shocking fish to the skin was shown to relieve pain locally (Stillings, 1971). Nowadays, electrical neurostimulation is commonly used in the clinic to treat a range of pathologies such as neuropathic pain, cardiac arrhythmia and Parkinson's Disease (Khedr et al., 2005; Munhoz et al., 2016). Besides clinical use, neurostimulation techniques are extensively used for neuroscientific inquiry. Functional brain mapping and behavioral research rely heavily on both electrical and optogenetic neuromodulation.

Neuromodulation techniques can be subdivided by the physical phenomenon used for stimulation, namely optical, magnetic, electrical or sonic stimulation. Optogenetics, in which light-sensitive proteins are expressed and stimulated in neurons, can be applied to specific neural populations with high selectivity. However, this method requires the viral manipulation of DNA in target neurons. Magnetic methods such as Transcranial Magnetic Stimulation (TMS), although low in spatial resolution, are completely non-invasive and considered to be safe. Several modalities of electrical neuromodulation exist, mostly characterized by their invasiveness and spatial resolution. The closer a stimulation electrode is situated to a target, the higher the resolution will be. However, there is an obvious tradeoff between invasiveness and resolution: getting close to tissue requires (deeper) implantation of electrodes, which increases invasiveness. Currently, the most efficacious neurostimulation therapies, such as deep brain stimulation (DBS), are also the most invasive. A common goal in medical device research and development is reducing invasiveness with minimal loss of efficacy and resolution.

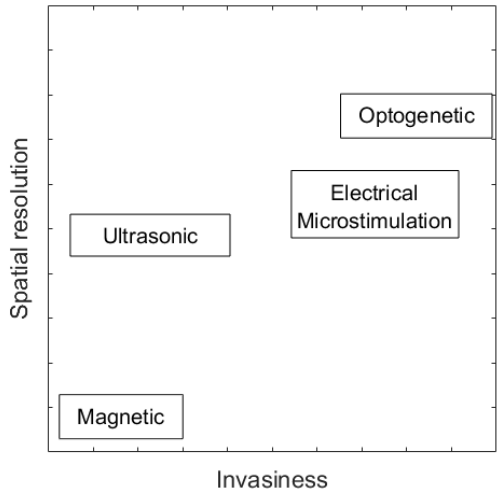

Figure 1 – Overview of general invasiveness versus spatial resolution for neurostimulation techniques in four different physical domains.

Ultrasound (US) neurostimulation is emerging as a high resolution, minimally invasive alternative to electrical or magnetic methods. The first observation that ultrasound could elicit responses in neural tissue similar to those observed in electrical stimulation was done in 1929. It was found that passing ultrasound through cardiac, smooth muscle and neural tissue causes observable excitation (Harvey, 1929). Over the next 80 years, only a handful of ultrasound neuromodulation experiments were published. Scientific interest in the subject was minimal until 2008, when it was shown that low intensity, low frequency ultrasound (LILFU) could safely and reversibly trigger action potentials in mouse brains (Tyler et al., 2008). More importantly, a mechanism of action was hypothesized. Tyler showed that voltage-gated sodium and calcium channels are at least partly responsible for neural excitation under ultrasonication. This was an important step in the elucidation of US neuromodulation, as it was the first mechanistic proof of the effect. Since then, several other mechanisms have been proposed, which are discussed later in this text. More often than not, US for neuromodulation is focused into a small volume. US waves can be focused mechanically by utilizing a lens or concave transducer. Additionally, electrical focusing can be achieved with an array of transducers. By introducing a phase delay between individual elements, a focal point or line can be generated, which has a much smaller volume and higher intensity than an analogues unfocused beam. This can be highly advantageous if high intensities and spatial resolution are required, which is the case for ultrasound neuromodulation. Interventional procedures performed with focused ultrasound are generally referred to as Focused Ultrasound Stimulation (FUS). Ultrasound neuromodulation is quickly becoming a popular topic, with academics and companies all around the world researching its capabilities.

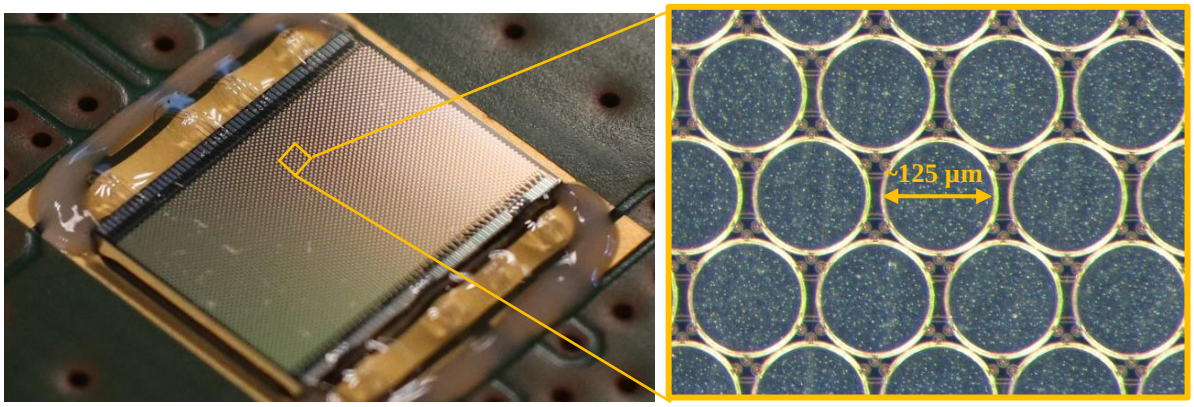

Figure 2 – Example of Philips CMUT array. **a)** Photgraph of PCB-mounted high frequency CMUT array. **b)** Micrograph of individual CMUT elements.

Coincidentally, ultrasound hardware is undergoing a technological revolution. After several decades of research, capacitive micromachined ultrasound transducers (CMUT) are reaching a point of maturity, outperforming traditional piezoelectric transducers in many aspects. As the name suggests, these devices make use of a capacitive mechanism to generate ultrasound, instead of the traditional piezo-electric approach. Two parallel plates separated by an air gap act as capacitive elements that vibrate when an AC signal is applied. CMUTs are fabricated using micromachining techniques traditionally used for the production of integrated circuits such as lithography, wet- and dry etching and thin film deposition. This makes devices very thin and production easily scalable. Other advantages are a lower operating voltage and the ability to integrate devices with electronics on the same die. Additionally, the absence of toxic materials allows for implantation into the body. Ultrasound is currently used almost exclusively as an imaging technique, with the exception of high intensity focused ultrasound (HIFU) ablation. However, if ultrasound neuromodulation is established as a robust neurostimulation modality, CMUT devices may find a myriad of new applications in the medical domain. One can imagine small, wearable devices that simultaneously image and stimulate target nerves. However, significant technological and medical research is still required to make such applications feasible.

This thesis documents two different but somewhat related research projects. For this reason, the thesis has been split into two separate chapters, discussing their respective topics. For the first project, the focus was on neurostimulation. The goal was to create a setup to allow the performance of ultrasound neurostimulation experiments. Because of the legal and practical limitations of animal research, the wish emerged for an experimental setup that could be used to show US neurostimulation efficacy in-house. As a neural model, the *Lumbricus Terrestris* or earthworm was chosen, and the project was concerned with developing hard- and software for simple electrophysiological observations in addition to performing *in-vivo* and *ex-vivo* experiments. As a secondary project, work was done on the design of a CMUT fabrication step. In order to produce low-frequency CMUT devices, which are preferred over high frequency CMUTs for certain applications, additional design considerations come into play. For example, lower frequency devices require a larger membrane. These large membranes displace more air, and the efficiency of ultrasound output is thus inversely related to the rigidity of the air gap. In other words, lower frequency devices require a large reservoir of air to function properly. One solution is to introduce vent holes in the device, allowing for the relief of pressure generated by the CMUTs. A fabrication method to etch vent holes from the back of silicon wafers to surface-micromachined CMUT structures was investigated.

Background and Justification

Theory of Ultrasound

Sonic waves with frequencies above the human audible range of 20 kHz classify as ultrasound (US). Ultrasound finds many applications in the fields of medicine, biotechnology and chemistry, amongst others. In the clinic, it provides a safe non-radiative and non-ionizing method of real-time imaging. Most commonly, it is used to visualize unborn babies and monitor their development in a process called obstetric ultrasonography. However, ultrasound can be employed in an interventional manner as well, as opposed to diagnostic imaging. Through several mechanical and thermal mechanisms, ultrasound can induce changes and facilitate certain therapeutic processes in the human body, one of which is neuromodulation. Neuromodulation is the non-pharmacological, reversible intervention into the nervous system. By inhibiting or exciting specific neural populations, a myriad of biological effects can be achieved. The recent discovery that low intensity ultrasound can reversibly elicit action potentials (APs) in living subjects has triggered a resurgence in the field of ultrasound neuromodulation research (Tyler et al., 2008).

Ultrasound Parameters

To understand US and the way it behaves in different circumstances, it is important to understand the different parameters that define the properties of an US wave. First, the *center frequency* or resonance frequency is the frequency at which an US transducer most efficiently translates electrical energy to mechanical energy. In other words, when driving an US probe at its center frequency, minimal energy is lost to heat as compared to other frequencies.

The acoustic impedance of a material is a useful metric because it is related to the transmission and reflection of sonic waves when passing from one material to another. For example, when ultrasound waves travel from a low impedance material to a material with high acoustic impedance, a large fraction of the energy is reflected instead of transmitted. Additionally, impedance is related to the absorption of energy when waves travel through a medium. It is calculated as follows.

Eq. 1
$$Z = \rho \cdot v$$

Where Z is the acoustic impedance, ρ the density in kg/m^3 and v the velocity of sound in m/s. The acoustic impedance consists of a real (resistive) part and an imaginary (reactive) part, shown in *equation 2*.

Eq. 2
$$Z = R + iX$$

Because ultrasound is an acoustic phenomenon, it causes pressure differences. However, measures of ultrasonic magnitude are often reported as *intensities* rather than pressure. Several different definitions of ultrasonic intensity exist. All of these are expressed as power over area, generally in W/cm^2. Important measures of intensity are the spatial peak point average intensity (I_{SPPA}) and spatial peak temporal average intensity (I_{SPTA}), which are defined as follows:

Eq. 3
$$I_{SPPA} = \frac{PII}{PD}$$

Eq. 4
$$I_{SPTA} = PII \cdot PRF$$

Where PII is the pulse intensity integral, calculated as:

Eq. 5
$$PII = \int_{t_2}^{t_1} \frac{P^2(t)}{Z_0}\, dt$$

Here, P is the instantaneous pressure and Z_0 the impedance of the medium. It is crucial to know the intensity when using ultrasound for any kind of application, because sufficiently high intensities can cause damage to the medium. This is especially important in medical ultrasound. Another metric that is essential for the safe use of clinical ultrasound is the mechanical index (MI). It represents the presence of mechanical bioeffects in tissue such as cavitation. For this reason, the United States Food and Drug Administration (FDA) has formulated upper limits for both the intensity and MI from a safety point of view (table 1)

Eq. 6
$$MI = \frac{P_n}{\sqrt{f_c}}$$

Here, MI is the dimensionless mechanical index, P_n the negative-peak pressure in MPa and f_c the center frequency of ultrasound in MHz.

For many applications, US transducers are operated in pulsed mode. Some transducers, especially when operating at high intensities, cannot sustain continuous output and will overheat and eventually burn when driven for too long. Additionally, continuous sonication may supply excessive energy to the tissue, possibly causing damage or other unwanted effects. In pulsed US, the *pulse repetition frequency* (PRF) indicates the number of US pulses generated each second. *Duty cycle* (DC) is the ratio of time the transducer is on as compared to the time it is off. In figure 3, an example of a 50% DC pulse train is illustrated. A 100% DC corresponds to continuous ultrasound. The duty cycle is calculated as follows:

Eq. 7
$$DC = PRF \cdot PD \cdot 100$$

Use	**I_{SPTA}** (mW/cm^2)	**I_{SPPA}** (W/cm^2)	**MI**
Peripheral Vessel	720	190	1.9
Cardiac	430	190	1.9
Fetal Imaging & Other	94	190	1.9

Table 1 – FDA regulation maximum acoustic output exposure levels for diagnostic ultrasound. (FDA, 2019)

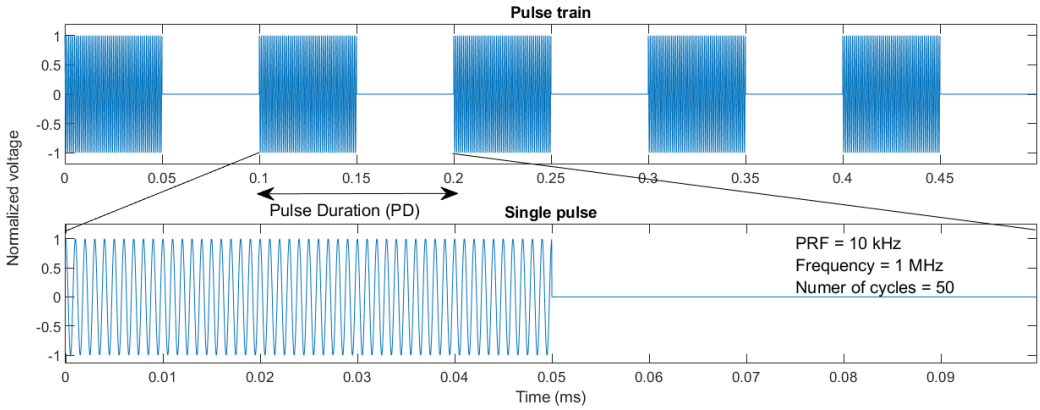

Figure 3 – Example of a signal used to drive an ultrasound transducer at DC = 50%, PRF = 10 Hz, f = 1 MHz

Ultrasound Neuromodulation Mechanisms of Action

After nearly a century since the first observation, a clear picture of the biophysical mechanisms responsible for ultrasonic neuromodulation is still absent. However, a handful of experiments have demonstrated and hypothesized possible mechanisms. Ion channels are the main cellular components responsible for the generation of action potentials, and the equations postulated by Hodgkin and Huxley are an excellent approximation of the electrodynamics of action potentials (Hodgkin et al., 1952). Following their theory, the idea that ultrasound-induced action potentials are due to the opening and closing of ion channels is an obvious candidate mechanism. Indeed, it has been shown that Na^+ channels, those which are responsible for the depolarization phase of the AP, can be forced open by ultrasound (Tyler et al., 2008). Thus, by applying ultrasound of the correct frequency and sufficient intensity, the potential of neurons is raised towards or even across the threshold voltage, resulting in increased excitability or newly generated (*de-novo)* action potentials.

Mechanical Activation

Other than through the opening of ion channels, ultrasound can also induce ionic transients by opening membrane pores, fittingly named sonoporation (Ohl et al., 2006). Because an ion gradient exists across neuronal membranes, the existence of a pore will cause a disruption in the steady-state transmembrane potential by increasing ionic fluxes. Although the exact sonoporation mechanisms are unknown, it has been shown that the chance for a pore to form is highly correlated to the presence of microbubbles. These vapor-filled microbubbles are generated by rapid changes in acoustic pressure, a process called cavitation. However, cavitation is generally considered an unwanted effect in neuromodulation because it can permanently rupture cells and damage tissue. Sonopores can also be generated by acoustic streaming, which is a fluid stream generated by high intensity acoustics. This may cause shear stresses in the cell membrane, which at sufficient intensity can open a pore in the membrane (Wu, 2018). Several types of sonoporation effects have been observed in neurons, ranging from permanent depolarization to reversible depolarization through re-sealing of the membrane (Qin et al., 2014). Because a goal of neuromodulation is to be reversible in nature, it is essential that effective and safe parameters be determined to avoid harmful amounts of cavitation.

The bi-lipid membranes separating the inside of a neuron from the extracellular space function as a type of capacitance, and they can accurately be modelled as such (Alvarez et al., 1978). It has also been shown that conformational changes of these membranes result in a change of capacitance (Taylor et al., 2017). This results in a capacitive current, directly influencing the potential of the cell. Because ultrasound can change the conformational state of cells by both the acoustic radiation force as well as thermal energy, it is likely that the resulting capacitive currents contribute to US neuromodulation.

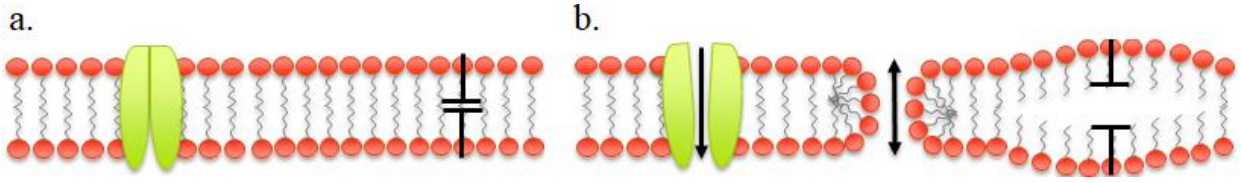

Figure 4 - Ultrasonication causes depolarization of neuron bilipid membranes through several mechanical mechanisms. Arrows indicate ion flux **a)** Resting state membrane with closed ion channels and absence of membrane deformation. **b)** Ultrasound causes specific ion channels to open, pores to form and membrane deformations resulting in a change in capacitance.

A final hypothesis for the mechanical activation of nerves through ultrasound is the membrane wave. Elastic waves related to action potentials, which travel down the axon during the impulse have been identified. These waves are accompanied by electrochemical and conformational changes in the neuron (El Hady et al., 2015) and can be elicited by mechanical stimulation. Although it has not yet been experimentally confirmed that when an US wave couples into such a membrane wave, it could influence its excitability or even elicit de-novo APs (Andersen et al., 2009).

Thermal Inhibition

A likely non-mechanical mechanism is thermal modulation. Perturbation of the homeostatic temperature of nerves has been observed to have significant consequences, effecting synaptic transmission, postsynaptic integration and both the generation and conduction of APs (Montgomery et al., 1990). These effects are generally inhibitory, as they hinder the physiological functioning of nerves. US is well known for its ability to cause large thermal effects, and neuromodulation observed in some studies has been attributed to thermal instead of mechanical changes to the neuron. (Constans et al., 2018). When conduction FUS experiments, it is important to rule out thermal contributions either by calculating or measuring the rise of temperature in the sonicated tissue.

Finally, an interesting mechanism was proposed in 2018, when researchers found that some neuromodulatory effects were not caused by direct activation of the target area, but through an auditory mechanism (Guo et al., 2018; Sato et al., 2018). Because the pulse repetition frequency of experimental FUS protocols is often in the audible range, sonication is capable of activating the cochlea, which in turn causes activity in the auditory cortex. Through a startle reflex, sufficient auditory activation can lead to motor activity. Because many *in-vivo* US neuromodulation studies employ motor cortex activation and EMG as a means of verifying efficacy, the conclusions of direct causal stimulation drawn from these studies may require reinterpretation. Additionally, future studies will need to eliminate the cochlear pathway in order to draw reasonable conclusions from their data. However, it is clear that this mechanism is not solely responsible for all observed effects, simply because many *ex-vivo* and *in-vitro* studies have shown neural activation from ultrasound, in which case the cochlear auditory pathway is completely absent. Additionally, as a reaction to Guo et al, a study in genetically deaf mice was performed to rule out this auditory mechanism. Results showed that wild-type mice and deaf mice have similar EMG responses to FUS, ruling out auditory activation (Mohammadjavadi et al., 2019).

Parametric Observations

Based on previous observations that more acoustic intensity is required to elicit action potentials at higher frequencies, one study investigates the influence of frequency and intensity on FUS efficacy in mouse brains. (Ye et al., 2016). Previous results were confirmed by showing that increasing US intensity increases efficacy, with higher frequencies requiring significantly higher intensities (Ye et al., 2016). Several variables related to US frequency are named and investigated as possible contributors, such as sonication duration, focal spot size, particle displacement, cavitation, radiation force and heating. It is concluded that the cavitation index and particle displacement explain most of the variance in the data and are likely the mechanisms responsible for frequency-dependent stimulation efficacy.

The acoustic radiation force (ARF) is the physical phenomenon when an acoustic wave encounters an object and transfers wave momentum to the object. ARF in liquids also causes particle displacement, termed acoustic streaming. Work by Menz et al has shown that the ARF is a major contributor to US neuromodulation, especially at higher frequencies. They have shown that high frequency ultrasound (43 MHz) is still capable of eliciting neural response in the *ex -vivo* retina, while cavitation events are completely absent (M. D. Menz et al., 2019; Mike D. Menz et al., 2017). In fact, efficacy increases at higher frequencies, directly contrasting results found by Ye (Ye et al., 2016). This could indicate the predominant mechanism

responsible for US neuromodulation differs between stimulated tissue type and anatomical location. ARF phenomena are likely to contribute to US neuromodulation by generating membrane capacitive currents in combination with sheer-stress related sonoporation (Prieto et al., 2013).

Research Models for US Neuromodulation

Animal Studies

Early work on ultrasonic neuromodulation was performed mostly in *ex-vivo* models, namely frog sciatic nerves (Colucci et al., 2009; Harvey, 1929; Mihran et al., 1990; Tsui et al., 2005; Young et al., 1961), rat hippocampal slices (Bachtold et al., 1998), disassociated neuron cultures (Khraiche et al., 2008) and rat thymocytes (Chapman et al., 1980). Although thymocytes are not directly associated with the nervous system, the finding that ultrasonication causes changes in potassium flux is still relevant, as it is the first mention of such a mechanism in literature. During these early phases, practically nothing was known of the biophysical mechanisms behind FUS. Many researchers hypothesized a thermal mechanism of action, based on the known capability of US to rapidly heat tissue. Additionally, it was shown that many of the observed effects, especially inhibition of nerves, could be reproduced by applying heat to the tissue, suggesting a thermal instead of mechanical mechanism (Lele, 1963).

Somewhat surprisingly, most researchers transitioned to *in-vivo* models quite rapidly, even before solid proof of the physical mechanisms responsible for US neuromodulation existed. Animal models are the closest approximation of human physiology available, so translation of these studies to humans is more straightforward than for *in-vitro* or *ex-vivo* studies. Another reason for this switch to living animals is the availability of an intact central nervous system. However, electrophysiological observation of biophysical effects inside the brain or peripheral nerves is somewhat restricted to low-resolution methods, making it significantly more difficult to make mechanistic claims based on these studies. These restrictions touch on a critical shortcoming in FUS research, namely the abundance of proof-of-concepts and the scarcity of mechanistic studies.

Human Studies

Some of the earliest work investigating ultrasound neuromodulation was performed in humans. Subjects reported sensations of heat, pain, tickling and others when their arms or hands were sonicated (L. Gavrilov, 1984; L. R. Gavrilov et al., 1977). More recently, successful stimulation of the human somatosensory cortex was reported (Lee et al., 2016; Mueller et al., 2014), in addition to primary motor cortex stimulation (Ai et al., 2018). Possibly the most comprehensive human FUS trial to date shows both electrophysiological and behavioral effects. Subjects participated in a tactile discrimination task while undergoing EEG. It was shown that thalamic sonication inhibits several EEG-metrics in combination with a reduced performance on the given task. It is also the first demonstration of successful subcortical US modulation in humans (Legon et al., 2018). This demonstration of FUS in humans serves as a justification for continued research by accentuating the clinical potential of the technology.

Methods

Lumbricus Terrestris as a Neural Model for Evoked Compound Action Potentials

The *Lumbricus Terrestris*, better known as the common earthworm or Nightcrawler, was chosen as an experimental model for neurostimulation in this study. Earthworms exhibit axonal gigantism, giving them very large diameter nerve bundles relative to their body size. This makes the nerves easy to locate and explant. Especially the ventral nerve cord (VNC), which runs along the entire length of the animal, is of interest to us. It has been shown that compound action potentials (CAP) in worms can be easily elicited and recorded in living specimen and extracted ventral nerves (Jérémy Vion-Bailly, 2015; Shannon et al., 2014; Vion-Bailly et al., 2019). These signals are generated by the simultaneous firing of a large ensemble of neurons, making the amplitude orders of magnitude higher than an individual action potential (AP). Earthworms are readily available, easy to keep, low-cost and possess lenient regulatory status. Earthworms also do not fall under the Dutch Law of Animal Testing *(Nederlandse Wet op de Dierproeven, BWBR0003081 1, Article 1b)* due to being a non-cephalopod mollusk. This means that no restrictions are imposed on research with these animals in terms of ethical permission, lab-requirements, personnel training, etc. These combined characteristics make earthworms an adequate candidate for simple neural models.

However, anatomical differences between mollusk nerves and mammalian nerves will pose a challenge for the translation of results from a worm model to application in humans. The most notable difference is the gangliated and segmented nature of the ventral nerve cord. Specifically, the VNC is composed of repeating segmented structures. These segments contain ganglia, groups of neural cell bodies responsible for relaying information between the VNC and sensorimotor neurons. The segments are separated by thin layers of tissue, which practically function as synapses (Bullock, 1945). Thus, axons are kept relatively short and information between them is transmitted synaptically. This is in stark contrast with human nerves, which can have uninterrupted axon lengths of over a meter. Another relevant attribute of the *Lumbricus* nervous system is the difference in conduction velocities between different fibers. Due to its larger diameter, the median fiber conducts action potentials significantly faster that the two lateral fibers (Yoshida et al., 2009). When conducting *in-vivo* neurostimulation experiments this means that two compound action potentials with different velocities can be observed. They serve as validation that recorded signals are indeed action potentials. Additionally, by determining the conduction velocity of each AP, they can be attributed to specific nerve bundles.

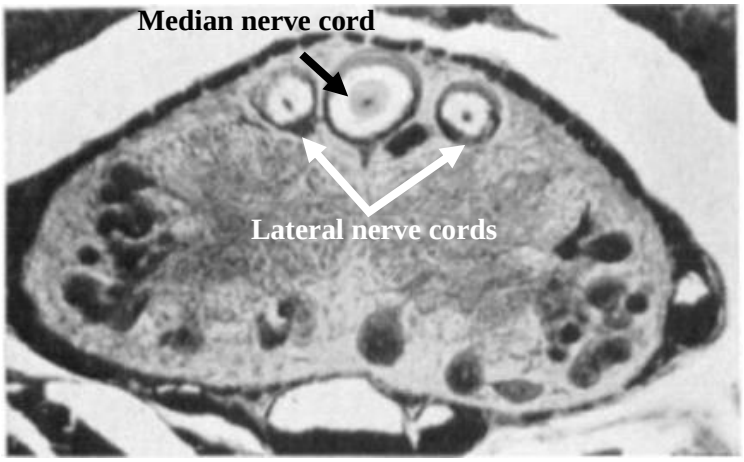

Figure 5 - Cross-section of *Lumbricus Terrestris.* Stained with silver proteinate and magnified 100X. Combined median and lateral nerve cords comprise the ventral nerve cord (VNC), visible at the top of the image. Adapted from Bullock (Bullock, 1945).

Handling of *Lumbricus Terrestris*

For each trial, mature *Lumbricus Terrestris* worms (N = 10) were obtained from a local distributor of fishing bait (Dierenspeciaalzaak Pierre Beelen, Eindhoven). Animals were kept in humidified (>65%, boiled tap water), enriched soil in a ventilated PET jar at 4°C. If unused for over two weeks, they were released.

In the case of *in-vivo* experiments, the animal was anaesthetized by immersion in a 10% isopropanol solution, diluted with buffered earthworm saline (table 2). Immersion persisted until no muscular response was given to physical stimuli to either end of the animal. Worms were then rinsed and dried, before being placed on a recording platform. Whenever the animal showed spontaneous muscular activity, anesthesia was repeated until requirements were met.

- For the first iteration of these experiments, two pairs of pins were placed through the animal on both sides (posterior/anterior) into a rubber platform as to both mechanically fix the animal and to function as recording and stimulating electrodes. Pins on one side were connected to a custom-built single channel amplifier capable of recording potentials in the order of microvolts. The other pins were connected to a function generator to electrically stimulate the neuron.
- The second, more advanced version of the experiment employed a printed circuit board (PCB) with golden line-electrodes as a tissue-electrode interface, relieving the requirement of piercing the animal.
- *Ex-vivo* experiments were performed on explanted medial nerve cords.

Medial Nerve Cord Explantation Protocol

A significant amount of experiments was performed on explanted medial nerve cords, the biggest and easiest to reach bundle of nerves in the *Lumbricus Terrestris*. Animals were anesthetized for at least 10 minutes, or until all muscular activity had seized, after which they were rinsed, dried and placed on a rubber dissection platform ventral side down. A dissection pin was placed in the anterior end of the animal to fix the worm to the platform. A small incision was made in the posterior end, revealing the digestive tract and septa connecting it to the interior wall of the animal. Using a pair of surgical scissors, the skin was cut along the entire length of the animal, effectively opening up the dorsal side of the animal. Then, by pinning the skin to the rubber platform and cutting the septa, all the internal organs were revealed. Carefully cutting away the digestive tract with a small scalpel gives access to the medial nerve cord, which lays on the ventral interior wall. Nerves were carefully lifted with tweezers starting at the posterior end, cutting away the connective tissue underneath until the full nerve could be lifted. It is important to moisturize the nerve periodically by placing it on the substrate. Explanted nerves were placed in saline until used, generally within 30 minutes.

Name	**Concentration (mM)**
NaCl	25
K_2SO_4	2.5
Na_2SO_4	30
$MgSO_4$	0.5
$CaCl_2$	10
Tris	5
Glucose	5

Table 2 – Earthworm saline recipe (pH = 7.4) used to dilute anesthetics and store nerves. (Storey, 1989).

Electrical Stimulation as Verification Method

Electrical stimulation is the most common form of neuromodulation and is relatively simple to perform. By applying short low voltage pulses to neural tissue, neurons can be depolarized and thus brought closer to their action potential threshold. Even though the focus of the current project is on FUS, it is essential to have a robust reference such as electrical stimulation to verify proper functionality of the used specimen, neural interface and amplification electronics. Thus, prior to US stimulation, each specimen was stimulated electrically. Initial *in-vivo* stimulation waveforms consisted of a single sinusoidal cycle, generated by a function generator (Agilent 33210A). However, the majority of electrical stimulations was performed with unbalanced biphasic square waves, such as shown in figure 6. For a recorded response to be counted as a CAP, several criteria needed to be met. These criteria are based on known characteristics of action potentials, namely conduction, consistency and all-or-nothing behavior.

- **Conduction**: Within the same bundle, CAPs are conducted at relatively constant velocities along the axon length. It can therefore be expected that, when recording with equally spaced electrodes, signals show up at subsequent electrodes at equal time intervals.
- **Consistency**: Successful stimulation with a given electrical pulse should be repeatable within a relevant timeframe, with similar results.
- **All-or-nothing Behavior:** Neurons fire only when the membrane potential is depolarized to the threshold potential, typically situated at -55 mV in mammalian nerves. Subthreshold stimulation results in no firing at all, making APs behave in a binary or "all-or-nothing" fashion. Stimulation should therefore not result in a graded response, but in a CAP or nothing at all.

Electrical stimulation can be controlled by either voltage, current or charge. In our case, voltage-controlled stimulation was chosen. Current- and charge-controlled stimulation have several benefits such as higher power efficiency and causing less damage to living tissue. However, due to the acute nature of the performed experiments, power efficiency and moderate tissue damage are not a significant concern. Additionally, the hardware used to run these experiments natively supports voltage-controlled outputs, whereas current- and charge-controlled stimulation would require additional circuitry.

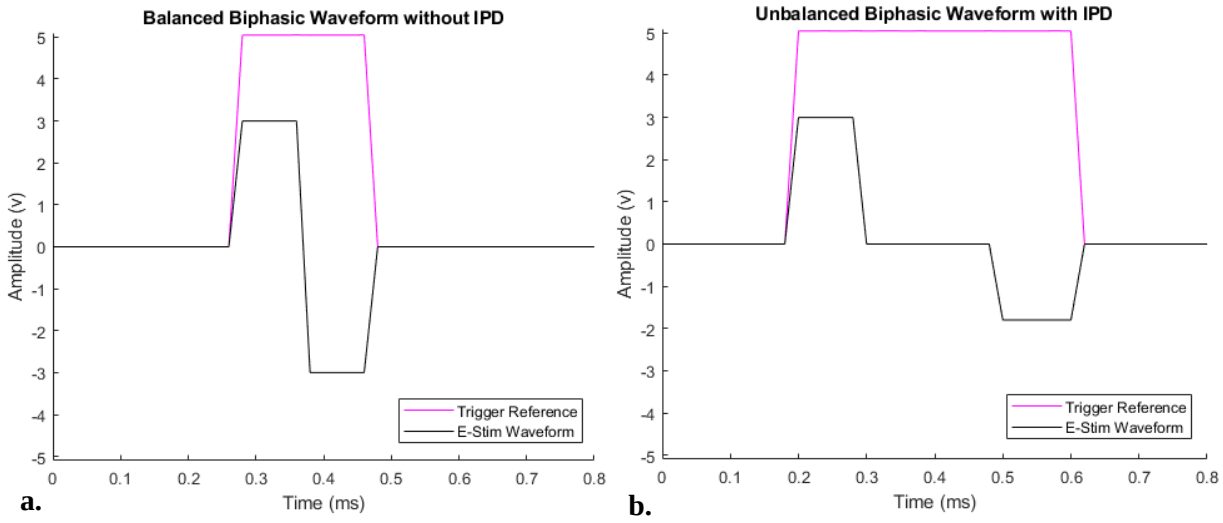

Figure 6 – Examples of electrical stimulation waveforms as generated by the neuroboard. **a)** Simple balanced waveform, meaning the positive and negative phase are of equal amplitude and length. **b)** Waveform used in experiments covered in this report. The second phase is wider (x1.2) and lower in amplitude (x0.6), and a 100 µs interphase delay exists between the phases. This helps membrane potentials to return to neutral values more quickly in addition to reducing the electrical artifact.

Recording Electrophysiological Responses

To verify neural spiking, compound action potential (CAP) recordings were performed. CAPs can be observed by recording the local field potential (LFP), which is an electric field generated by the summated activity of neural ensembles. A prototype single-channel amplification device was designed and assembled for this purpose. It encompasses a two-stage operational amplifier circuit that uses a low input-noise differential amplifier (Analog Devices, AD623) combined with a secondary amplifier (Texas Instruments, TLC2272). Together, these devices amplify the input signal approximately 800-fold. The output signal was digitized at 50 kHz and acquired with a data acquisition system (National Instruments, NIDAQ USB-6259), connected to a laptop running a custom written LabVIEW 2018 program (Appendix A).

The initial neural interface consisted of steel needle electrodes inserted close to the ventral nerve cord and pushed into the rubber platform underneath the specimen. However, this method proved to introduce electrical noise and possibly nerve damage due to blind insertion of electrodes. Thus, a non-invasive approach was chosen in the form of a one-dimensional array of gold line electrode pairs on a printed circuit board (PCB) (figure 10). Additionally, a more robust, multichannel device was designed and assembled on a PCB.

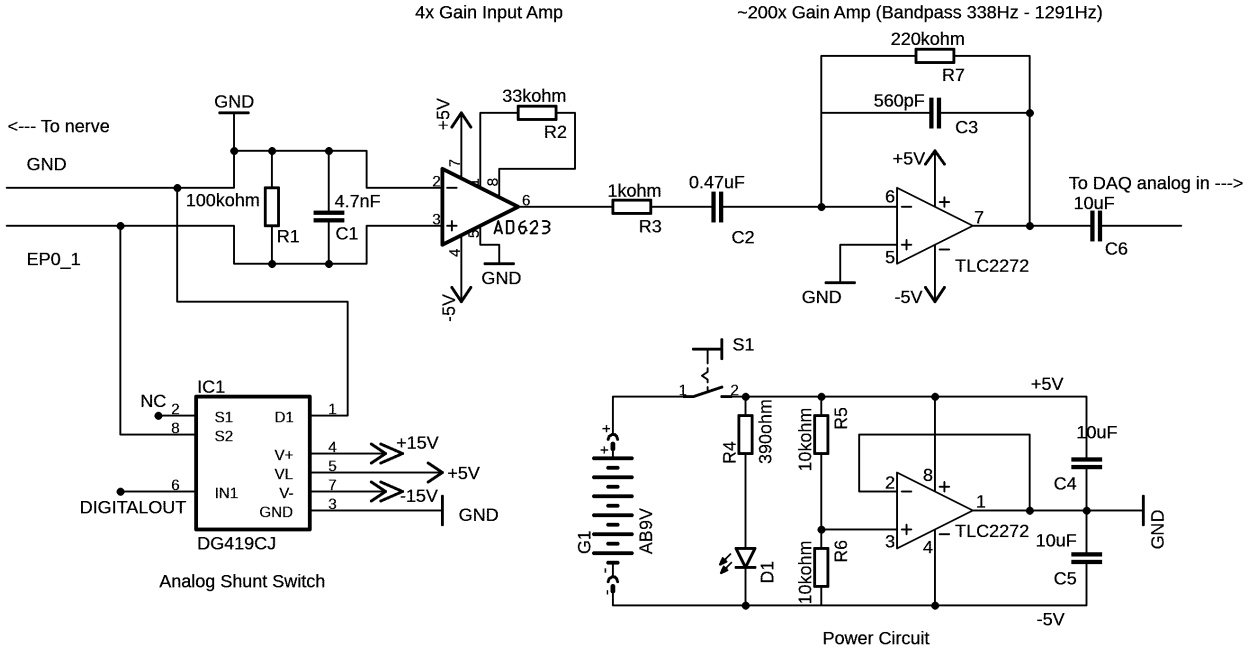

Figure 7 – Schematic of the single-channel LFP recording prototype, including shunt switch and power circuitry.

This multichannel amplification board contains four circuits as shown in figure 8. Neural interfaces can be connected to the board by means of a ribbon cable. Additional ribbon cables enable direct connection to the data acquisition system.

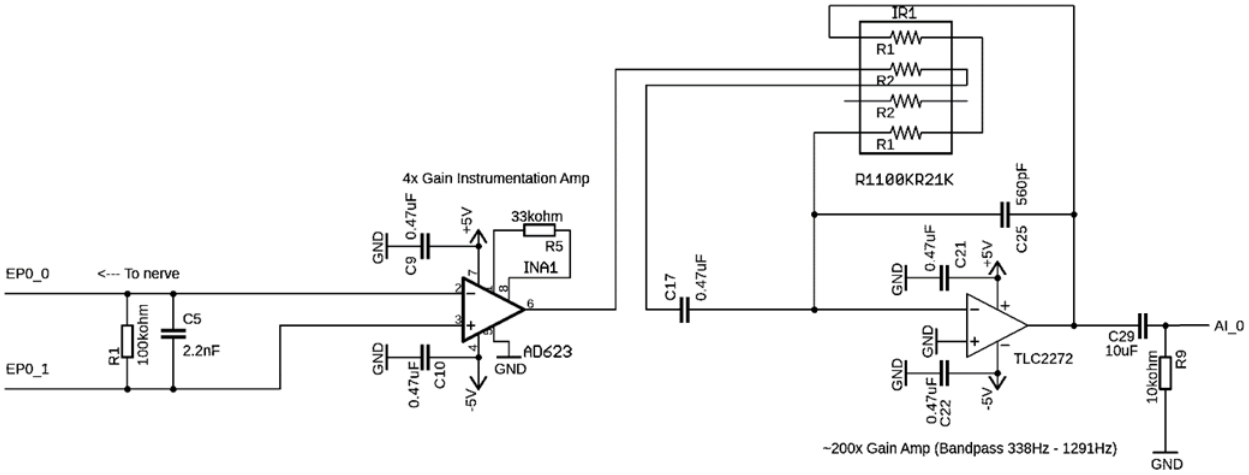

Figure 8 – Schematic of the final design of a single neuroboard amplification channel.

Digitization and Software

Software for the data acquisition system was written in LabVIEW 2018 (National Instruments, Austin TX). The program facilitates stimulation with both electrical and ultrasonic modalities, while simultaneously digitizing, recording and displaying data output from the amplification board. For electrical stimulation, customized square waveforms can be generated with variability in amplitude, duration, balancing, interphase delay and the number of pulses. Additionally, the channel used for stimulation can be selected. When a stimulation protocol is triggered, a snapshot of the resulting electrophysiological effect is displayed to verify the efficacy of stimulation, allowing for rapid experimentation with immediate feedback. Snapshots are recorded in a file separate from the main recording file to reduce file size and facilitate easier processing. A more elaborate discussion and full documentation of the software can be found in Appendix A.

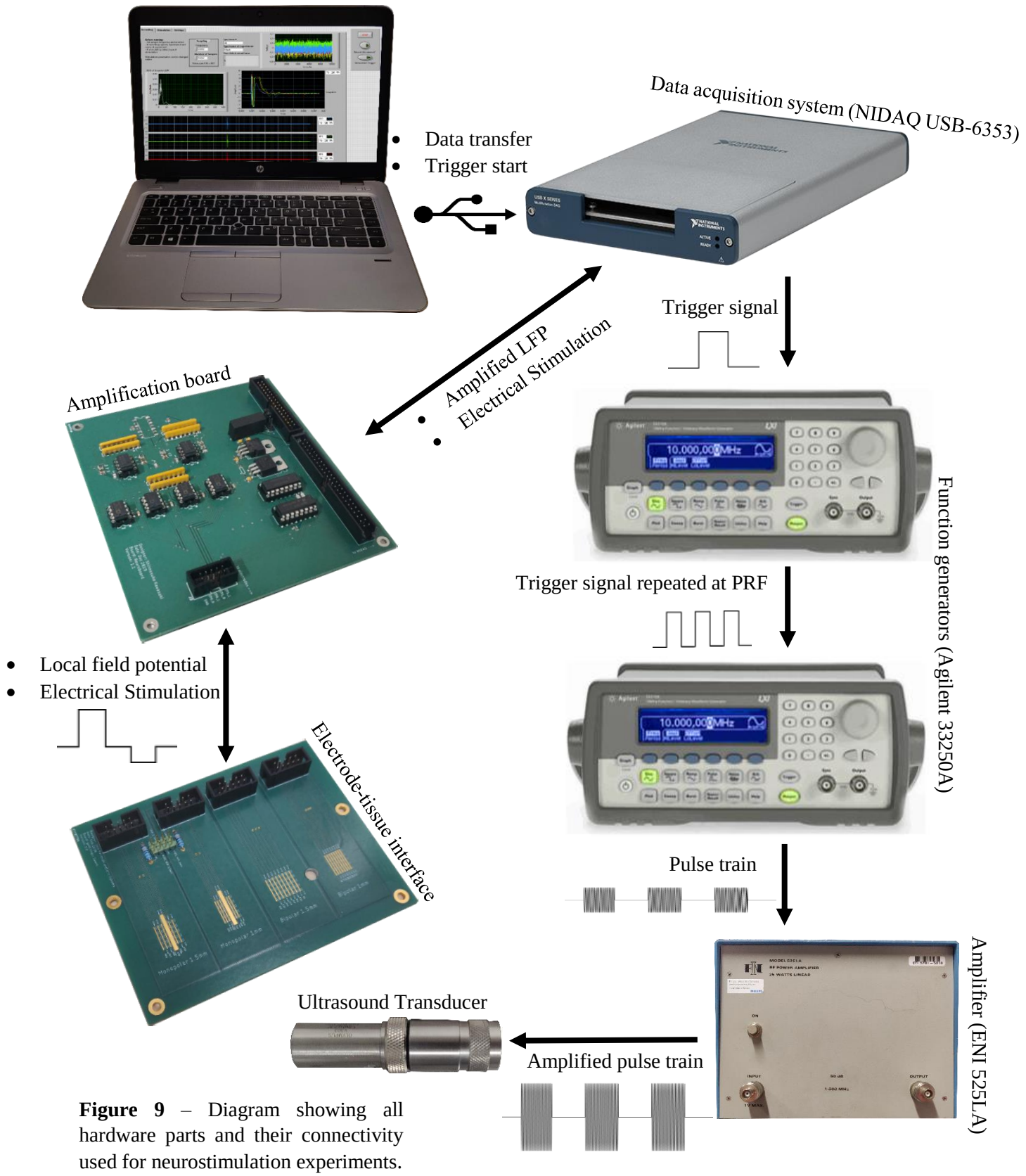

Figure 9 – Diagram showing all hardware parts and their connectivity used for neurostimulation experiments.

In-vivo Experiments

Methods

Several types of neurostimulation were performed. The simplest form of "neurostimulation" is mechanicalstimulation. By simply touching the animal on the anterior or posterior end of its body, a large assembly of mechanoreceptors is activated, in turn causing a startle reflex. This startle reflex travels along the medial nerve cord and can be recorded as a CAP. This type of signal can only be elicited in live animals, due to the absence of mechanoreceptors in explanted nerves. To stimulate electrically, a biphasic low-voltage pulse is applied to the animal or explanted nerve. Precise parameters (duration, voltage, burst, balancing) were determined by incrementally increasing these values until a neural response is observed. Electrical stimulation results are used to verify the physiological functioning of nerves before applying ultrasound. Specimen that showed neural response to electrical stimulation were subjected to ultrasound stimulation by a piezoelectric probe. Two MHz-range frequencies were explored, namely 1 MHz and 5 MHz.

Stimulation Protocol

In-vivo experiments were possible due to the easy-to-reach nature of the ventral nerve cord, requiring no surgical intervention to stimulate or record. The goal of these first experiments was to verify the functionality of the recording device. Mechanical and electrical stimulation were performed to generate evoked compound action potential (eCAP) responses. Mechanical stimulation was performed by touching the anterior end of a specimen with a plastic pipette. The material is purposely non-conductive because preliminary trials showed that touching with a conductive material introduced significant 50 Hz mains noise. Electrical stimulation entailed applying a single sinusoidal cycle of varying amplitude and length to determine eCAP thresholds.

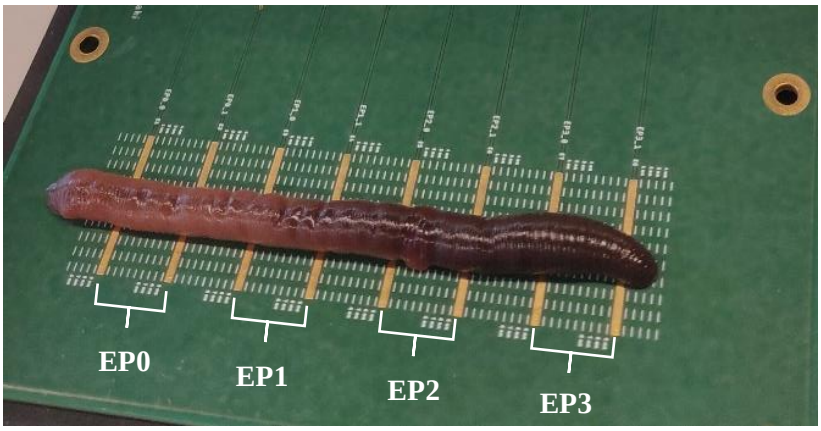

Figure 10 – *Lumbricus Terrestris* undergoing electrical stimulation trial with inter-electrode distance of 10mm. Electrode pairs (EP) are marked.

Ultrasound stimulation was performed with a focused 5 MHz piezo-electric probe (V310, Olympus). Probes were connected to a 25W 50 dB RF amplifier (ENI 525LA), which is connected to a waveform generator (Agilent 33210A*)* outputting a sinusoidal 5 MHz signal with an amplitude between 1 V_{pp} and 10 V_{pp} (see figure 9). A sonication strategy was devised based on previous research showing positive results for pulsed US neurostimulation of earthworms with a duty-cycle of 15% (Jérémy Vion-Bailly, 2015). Additionally, higher duty cycle protocols were experimented with, since 50% and higher duty-cycles have been correlated to increased excitation (Naor et al., 2016). Table 3 shows an overview of all performed strategies. A manual XYZ stage was used to align US probes with respect to the specimen in the case of pulsed stimulation. During continuous stimulation, the probe was manually moved over the worm to "scan" for the nerve, using recorded CAPs as an indication for proper alignment.

Frequency (MHz)	N_{cycles}/pulse	Pulse Repetition Frequency (Hz)	Duty Cycle (%)
5	6000	125	15
5	20000	125	50
5	N.A.	N.A.	100
5	2500	1000	50

Table 3 – Waveform parameter sets used for *in-vivo* US neurostimulation trials. Number of cycles and PRF are not applicable (N.A.) for continuous output.

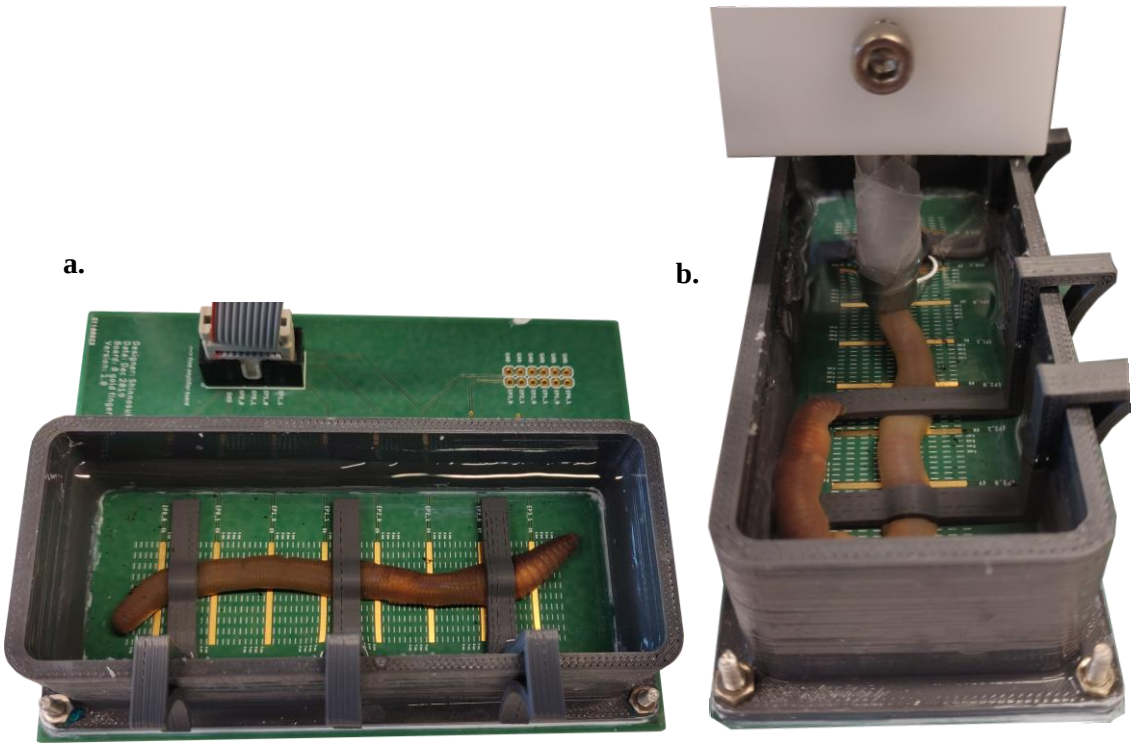

Figure 11 – Photographs of *in-vivo* ultrasound neurostimulation experiments. **a)** *Lumbricus Terrestris* submerged in saline, while custom made brackets keep the animal connected to gold line electrodes. **b)** Specimen under 5 MHz sonication.

Results

Both mechanical and electrical stimulation methods succeeded in eliciting CAP waveforms. Applied ultrasound did not result in excitation. A total of 42 trials were performed *in-vivo*. In most cases, two or three modalities were tested per animal. Stimulation success was 69% for mechanical stimulation (29/42), 51% for electrical stimulation (19/37), and 0% for US stimulation (0/23).

	Single-channel trials (N)	**Stimulation success (N, %)**	**Multichannel Neuroboard trials (N)**	**Stimulation success (N, %)**
Mechanical	33	24 (73%)	9	6 (67%)
Electrical	26	10 (38%)	9	9 (100%)
Ultrasonic	16	0 (0%)	7	0 (0%)

Table 4 – Result summary of success rates for mechanical, electrical and ultrasonic stimulation modalities *in-vivo*.

Mechanical Stimulation

The first trials had only one goal: to verify the functionality of the recording device. Literature suggests that anaesthetized worms, although immobile, still exhibit reflex-mediated neural responses to touch. Indeed, after several trials we were able to show consistent neural firing as a direct result of mechanically stimulating either end on the anterior-posterior axis. Figure 12.a shows an example of successfully evoked CAPs. These results indicate that the amplification board functions as expected.

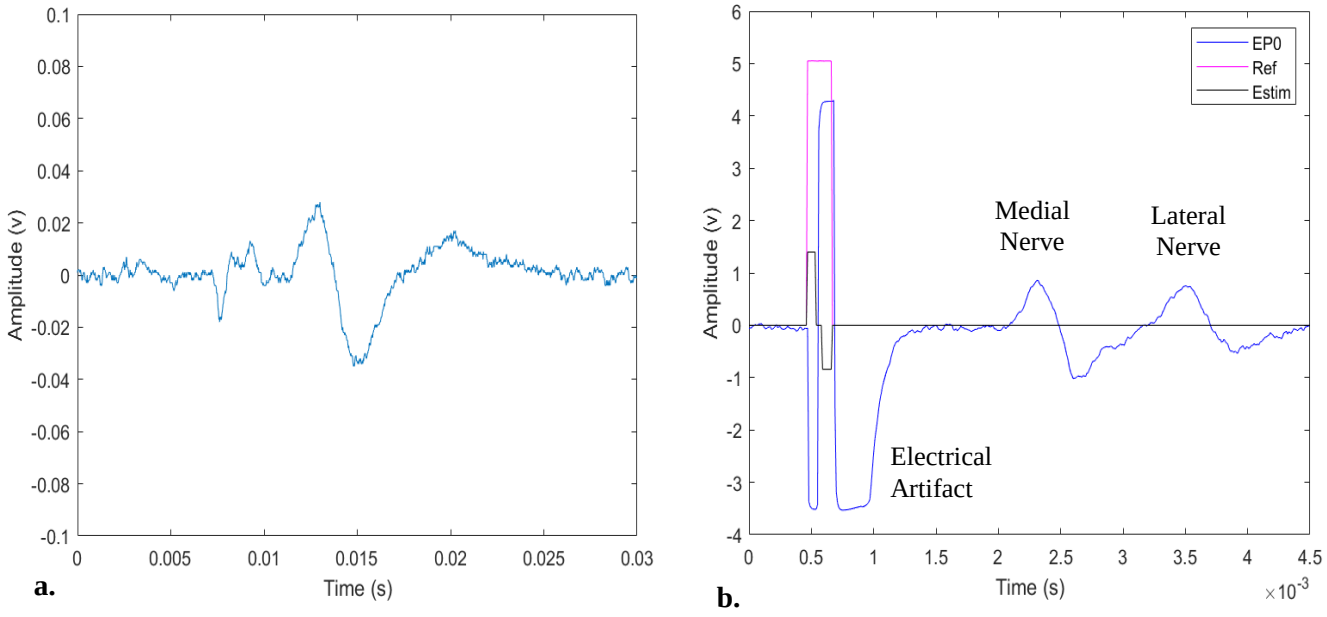

Figure 12 – Evoked CAP resulting from mechanical and electrical stimulation *in-vivo*. **a.** Mechanical stimulation only results in excitation of neurons expressing mechanosensitive ion-channels, whereas electrical stimulation recruits any type of neuron. Because the CAP amplitude is related to the number of simultaneously firing neurons, mechanical stimulation generates eCAP signals that are orders of magnitude lower than electrical eCAPs. **b**. One of the few *in-vivo* electrical stimulation trials with clear, high amplitude action potentials that are separated in time. Medial and lateral nerve bundle contributions can be distinguished due to a difference in conduction velocities.

Electrical Stimulation

Electrical stimulation has proven itself to be an adequate method for the verification of neural functioning. Low success rates for the single channel device can be explained by the electrodes used, namely iron needles which were likely covered with an oxide. After introducing gold electrodes the success rate increased to 100%.

Problems with stimulating electrically immediately became apparent from the presence of a large electrical artifact. Due to the ion-rich internal environment of earthworms, a relatively low resistance path is present between stimulating and recording electrodes. Small electrical fields near recording electrodes were amplified to the maximum operating range of the amplifiers (5V), thus rendering them unusable. In some cases, artifacts lasted long enough to obscure any local field potentials generated by action potentials (figure 13). This restricted identification of eCAPs, and thus resulted in data inaccuracy. However, in most cases at least one channel was far away enough from electrical stimulation to be mostly unaffected by it. It was also found that moisture on the skin of the animal significantly increased the amplitude and duration of electrical artifacts. In some trials, medial- and lateral nerve contributions could be distinguished by their differential conduction speed (figure 12.b).

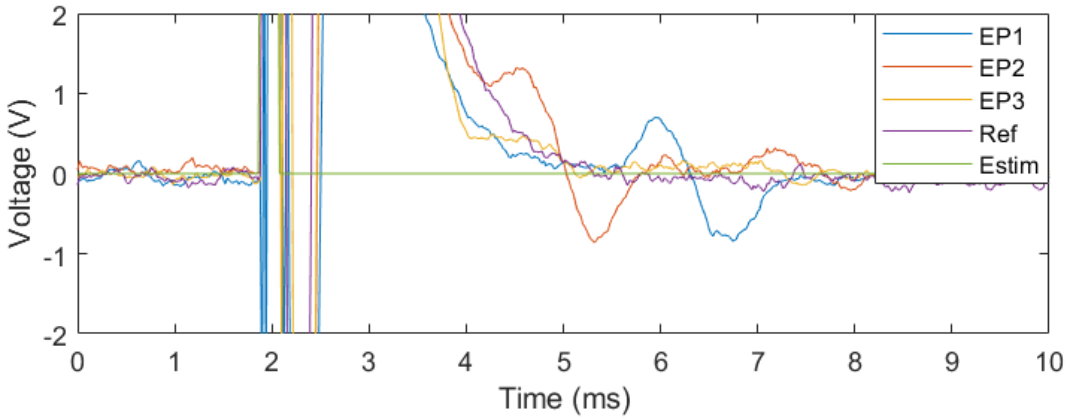

Figure 13 – Successful neuroboard recording of electrically evoked compound action potential in *Lumbricus Terrestris*. Expected signal on EP3 (yellow) is obscured by the electrical artifact.

Ultrasound Stimulation

Initial results showed significant electrical coupling between the transducer and recording electrodes, shown by electrical artifacts repeating at the PRF. A need for electrical isolation was bared, and transducers in all following experiments were encapsulated in parafilm, a blend of wax and polymers. Unfortunately, no positive results could be observed for *in-vivo* ultrasound neuromodulation.

Incorporating Experimental Insights into Future Experiments

Although *in-vivo* experiments did not yield positive results with regards to FUS, several clear problems were identified, to be solved in order to move further. Primarily, a solution to the failure of ultrasound to excite nerves needs to be found. Several aspects of the experiment were identified as potential failure modes, with the most important one being alignment. Due to the small scale of both the sonic focal point (~200 µm) and nerve cord (~100 µm), manual alignment with minimal visual cues is very challenging (Bähring et al., 2014). Exposing the nerve cord could help with alignment, although it would introduce problems in terms of tissue degradation, salinity and acoustic coupling.

Secondly, the electrical artifact observed during most trials requires reduction. As previously mentioned, a resistive path between stimulating- and recording electrodes is the cause of this artifact. Because of the high degree of amplification, operational amplifiers are quickly saturated and take a significant time to return to neutral values. These two causes hint towards two solutions: reducing the conductive path or preventing op-amps from reaching saturation values. The latter was tried first: analog switches were added to the circuit board, which shorted input lines when activated. Shorted op amps output zero, preventing saturation of the subsequent amplification stage. However, trials with this setup showed an additional artifact, namely that of the switching itself. From this observation, it was concluded that the conductive path between stimulating and recording electrodes needed to be eliminated, making the switch to explanted nerves an easy choice.

For the transition to an *ex-vivo* model, several adjustments were made. Primarily, the inter-electrode distance was reduced significantly, from 10 mm to 1 mm. Explanted nerves tend to contract and become much shorter than in physiological conditions, thus restricting the possible length of electrode arrays. A coupling cone was 3D-printed to facilitate acoustic coupling, and an explantation protocol was written and verified.

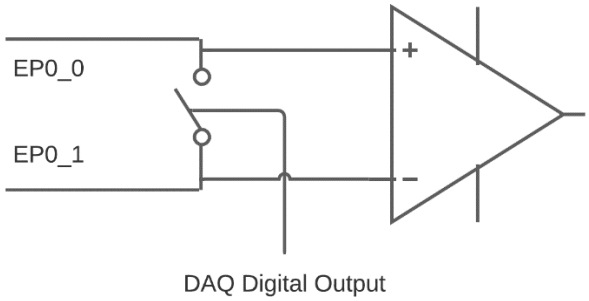

Figure 14 – Simplified schematic illustrating amplifier shunting used in the neuroboard prototype. DAQ digital output is synchronized with the stimulation trigger, ensuring amplifier inputs are shorted during stimulation. EP0_0 and EP0_1 refer to a pair of interface electrodes.

Ex-vivo Experiments

Methods

Ex-vivo trials required a different approach. Where in previous experiments the intact body of the animal was used to couple a transducer acoustically to the nerve, the absence of a body in *ex-vivo* experiments requires another method of coupling. For this, a 3D-printed coupling cone was used, specifically designed for the used probes. The cone is attached to the front of the transducer and filled with ultrasound gel, which has a similar acoustic impedance to biological tissue. It also functions as a visual waveguide (figure 15). Another issue with explanted nerves is their tendency to lose moisture quickly by evaporation, so periodic application of saline is essential for the longevity of the nerve. It was also decided, based on previous FUS work done in earthworms, that a lower frequency would likely result in a higher chance of stimulation success (Jérémy Vion-Bailly, 2015; Wahab et al., 2012). Lower US frequencies generate a larger focal point and are more likely to cause cavitation events. Thus, most *ex-vivo* samples were sonicated at 1 MHz. Two pulse repetition frequencies were chosen: one was based on previous work done on the *Lumbricus Terrestris* (125 Hz), and another that has emerged as a research standard (1000 Hz). A wide range of duty cycles was chosen as to vary the ultrasound intensity. For each trial, voltage amplitude was incrementally increased from $1V_{PP}$ to $10V_{PP}$.

Frequency (MHz)	N_{cycles}/pulse	Pulse Repetition Frequency (Hz)	Duty Cycle (%)
1	400	125	5
1	1200	125	15
1	4000	125	50
1	N.A.	N.A.	100
1	50	1000	5
1	150	1000	15
1	500	1000	50

Table 5 - Waveform parameter sets used for *ex-vivo* US neurostimulation trials. Number of cycles and PRF are not applicable (N.A.) for continuous output.

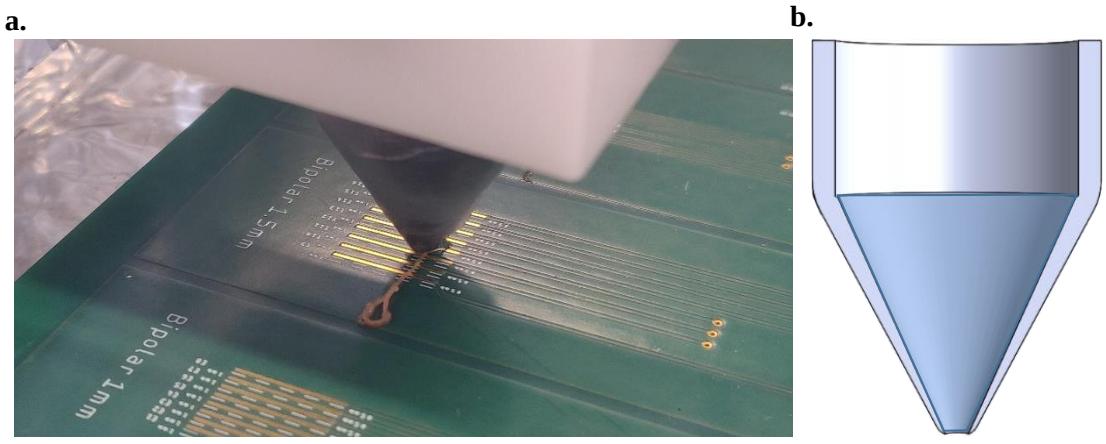

Figure 15 – **a)** Photograph of explanted *Lumbricus Terrestris* medial nerve cord under ultrasonication. The transducer is suspended above the interface PCB and coupled to the nerve through a coupling cone. The nerve makes contact with gold line-electrodes, which function as stimulation and recording sites. **b)** Cross-section of coupling cone. The blue volume is filled with ultrasound gel, which couples the transducer (top) to the specimen (bottom).

Schlieren Experiments

In order to avoid issues encountered in previous trials, a final experimental design was made based on an imaging technique called Schlieren photography. With Schlieren optics, differences in density can be visualized due to a relation between density and the refractive index. This allows for real time imaging of ultrasound, due to its longitudinal (compressive) waves. An example of a Schlieren image of ultrasound is shown in figure 16. An experimental setup was devised to apply ultrasound to a nerve while simultaneously imaging the process. This would allow for the alignment of the sonic focal point within the nerve in two dimensions, in an attempt to solve the problem of misalignment. In the case that a significant impedance mismatch exists between the water and neural tissue, some refraction may take place, which could be observed to verify correct alignment. Because both the stimulated part of the nerve and the transducer are submerged, no coupling issues should be expected.

Schlieren imaging requires a collimated beam of light to travel through the medium one would like to observe. The beam of light is focused into a point and blocked by a small dot or razorblade. The laser is pulsed at the ultrasound PRF, with a short delay to allow the US wave to travel. When this disturbance of refraction takes place in the medium, collimated light bends around the blocking device and is recorded by a camera. Figure 17 shows an illustration of the Schlieren setup.

Frequency (MHz)	**N_{cycles}/pulse**	**Pulse Repetition Frequency (Hz)**	**Duty Cycle (%)**
1	400	125	5
1	800	125	10
1	500	1000	50
10	8000	125	10
10	5000	1000	50

Table 6 - Waveform parameter sets used for *ex-vivo* US neurostimulation trials in Schlieren setup.

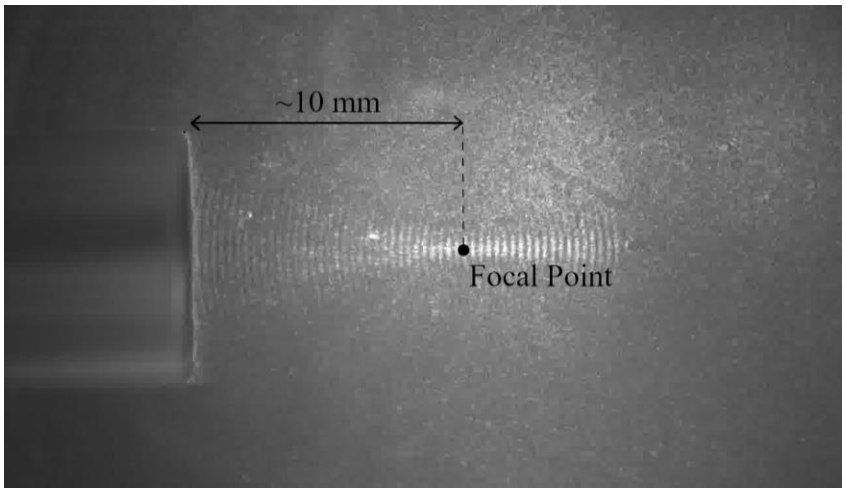

Figure 16 – Visualization of 5 MHz ultrasound waves. The image was obtained using Schlieren imaging, which is capable of imaging disturbances in refractory indexes in real time. Ultrasound waves are visible because the pressure gradient influences the refractory index of the medium. Energy is focused at approximately 10mm distance from the transducer.

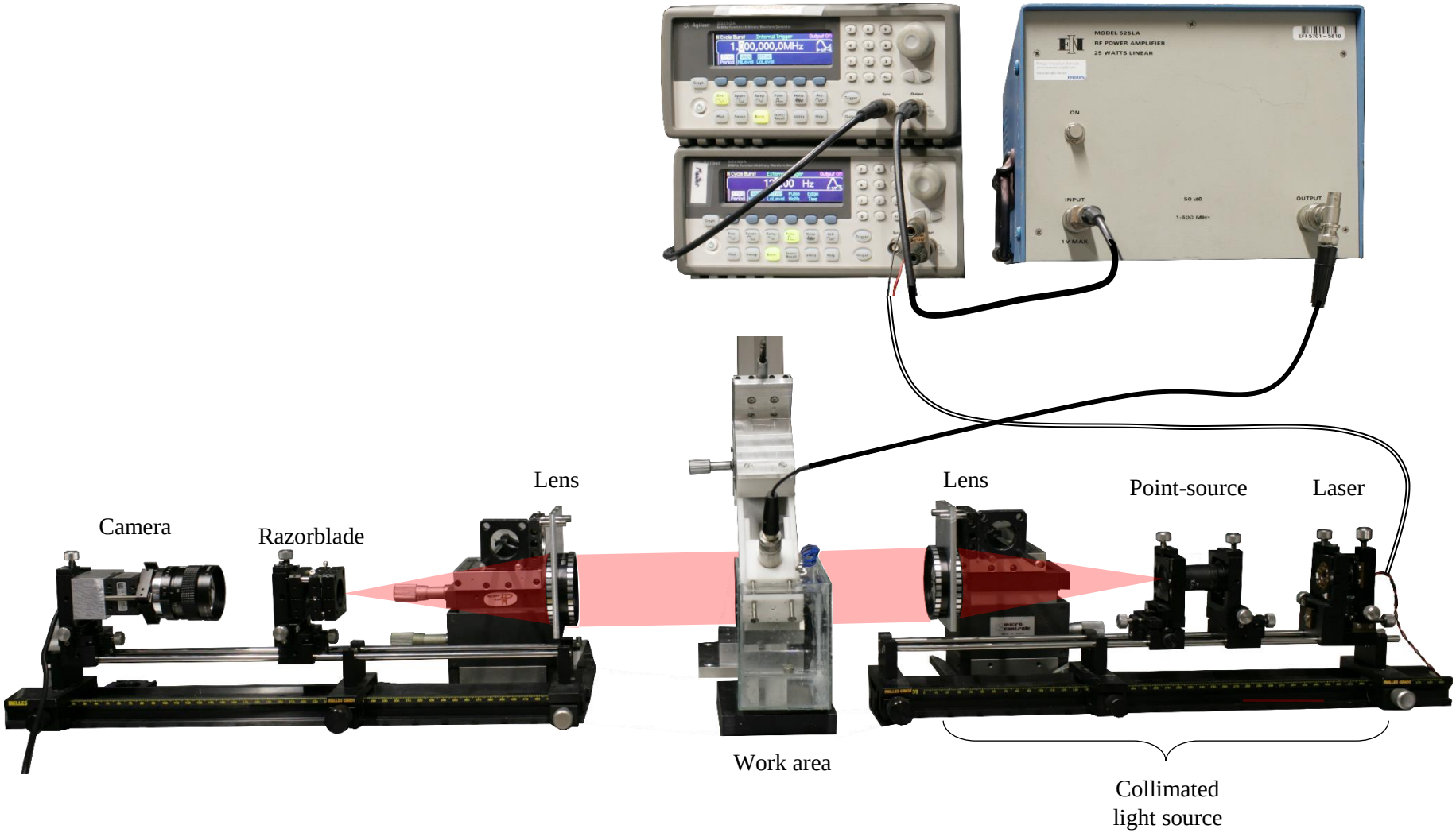

Figure 17 – Photograph of Schlieren optics setup. Light travels from right to left. Laser light is turned into a point source and parallelized by a lens, resulting in a collimated beam. This beam illuminates the work area, which contains the ultrasound probe, nerve, electrodes and is filled with saline. Then, the light is focused again and blocked by a razorblade. Ultrasound-induced changes in density cause light to refract around the razorblade and onto the camera, where it is recorded and displayed on a monitor.

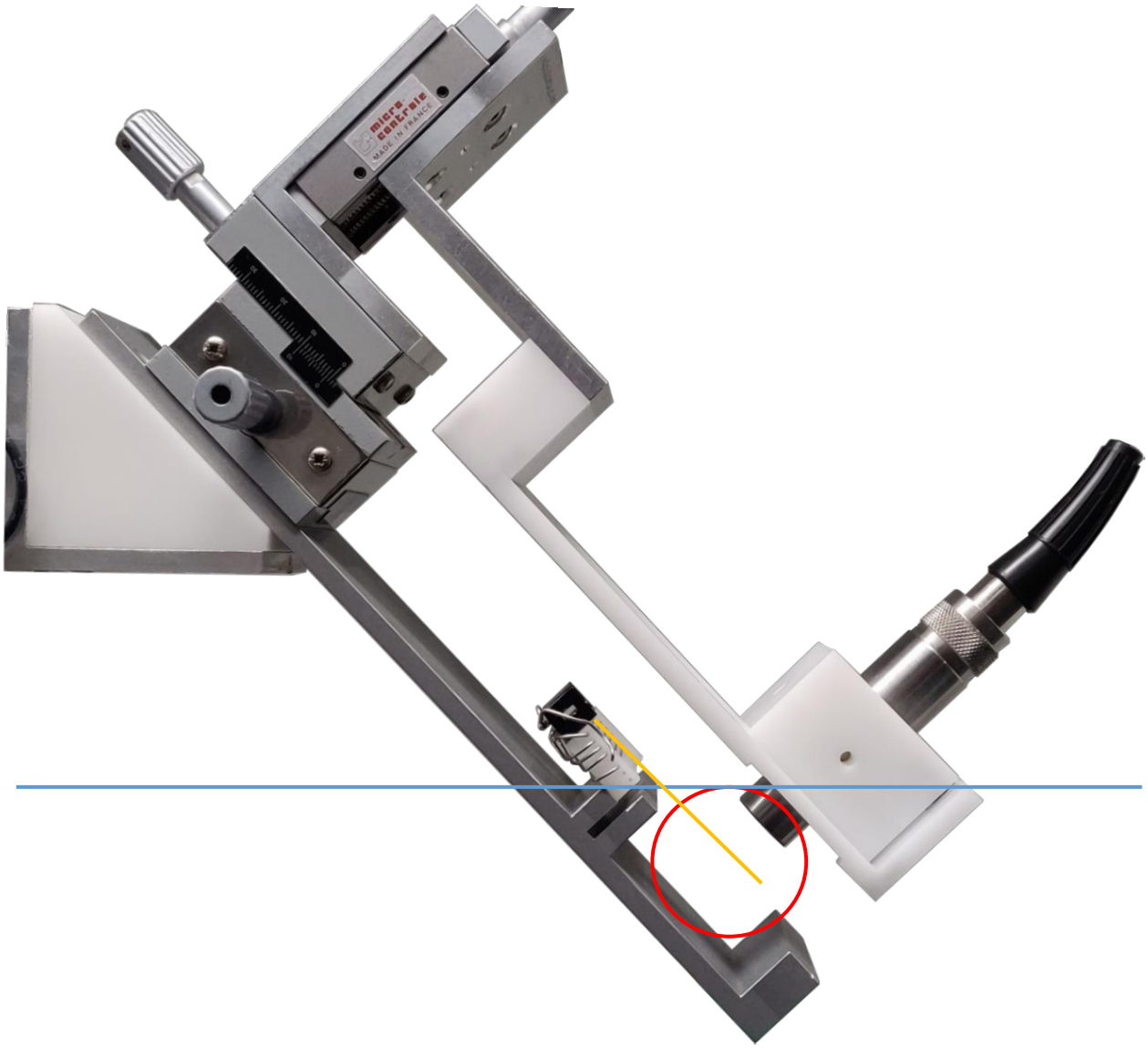

Figure 18 – Photograph of work area for Schlieren imaging during FUS. Two platforms, capable of moving relative to each other in all dimensions, are parallel suspended in saline. The blue line represents the saline level. Both platforms are slanted at a 45˚ angle to allow the nerve (yellow line) to be partly out of the saline, where four sets of electrode pairs record local field potentials. An ultrasound transducer is placed on the top platform, to be focused on the nerve. The perspective of this image is how the camera "sees" it, with the red circle indicating the image field.

Ultrasound Power Transfer

An alternative to direct US neurostimulation is electrical stimulation combined with US power transfer. When US is emitted into the body onto an implanted receiver, power can be transferred. Using this energy, electrical stimulation can be performed. Power transfer technology allows active implantable devices to function without requiring a large power storage component such as a battery. In the case for neurostimulation devices, the direct transduction of acoustic to electrical energy severely reduces the amount of electrical components required for a device to function. Several research groups have been working on miniaturized version of such devices (Piech et al., 2020). However, all currently published prototypes make use of a piezoelectric crystal as opposed to a CMUT for power harvesting. Here, we attempt to demonstrate the efficacy of CMUTs for this application.

The setup of a student studying US power transfer was combined with the neurostimulation setup. Ultrasound pulses (24 cycles, 4 MHz) were emitted through a phantom by a programmable clinical ultrasound device (Vantage, Verasonics) onto a receiving CMUT 10 cm deep into the phantom. This CMUT converted the acoustic (mechanical) energy into an electrical signal. The signal was rectified with a single diode and supplied to an electrode pair. An explanted *Lumbricus Terrestris* nerve was connected to the electrodes for electrical stimulation.

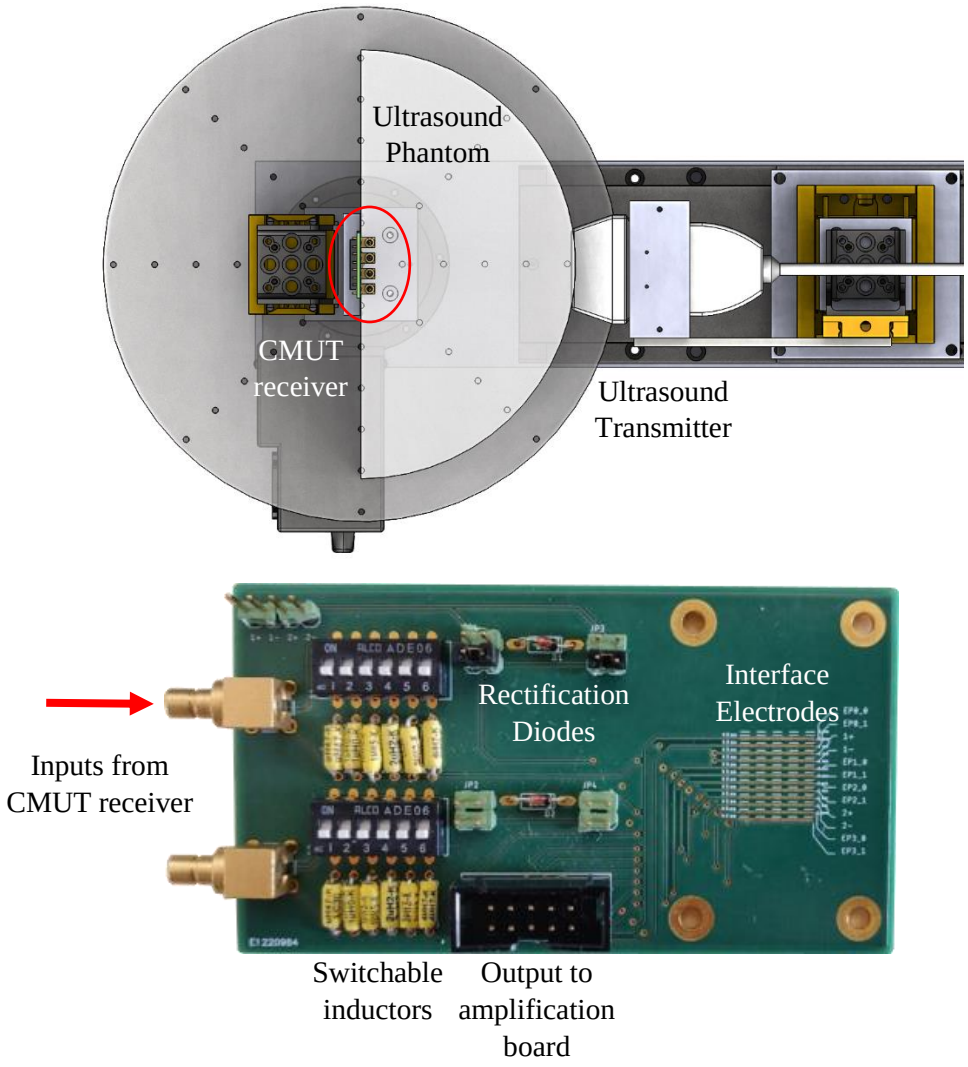

Figure 19 – Ultrasound-to-electrical stimulation setup. **a)** 3D-model of power transfer hardware. Right to left: A medical imaging probe sonicates a CMUT receiver through a phantom. Image courtesy of Y. Westhoek (Westhoek, 2020) **b)** Photograph of interface PCB used for power transfer experiments. Inductive matching is required to maximize transduction efficiency. 1+/- and 2+/- refer to stimulation channels. Designed by Shinnosuke Kawasaki.

Results

Experimentation on explanted nerves proved to be a feasible method for electrical stimulation, with a success rate of 83% (29/35). Significantly reduced noise and excellent signal amplitude were observed, resulting in an improved signal-to-noise ratio (SNR) as compared to *in-vivo* trials. Indirect ultrasound (power transfer) stimulation trials resulted in a 50% success rate (2/4), whereas direct US stimulation failed (0/25).

Stimulation modality	Trials (N)	Stimulation success (N, %)
Electrical	35	29 (83%)
Ultrasonic	25	0 (0%)
Power Transfer	4	2 (50%)

Table 7 – Result summary of success rates for electrical, ultrasonic and power transfer stimulation modalities *ex-vivo*.

Electrical Stimulation

Nerves that were stimulated electrically consistently showed clear compound action potentials. One example can be seen in figure 20. Lower voltages were required to elicit CAP responses in explanted nerves (mean 4V) than during *in-vivo* experiments (mean 7.5V). This may be attributable to the nerve being closer to stimulation electrodes, and the narrower spacing between electrodes.

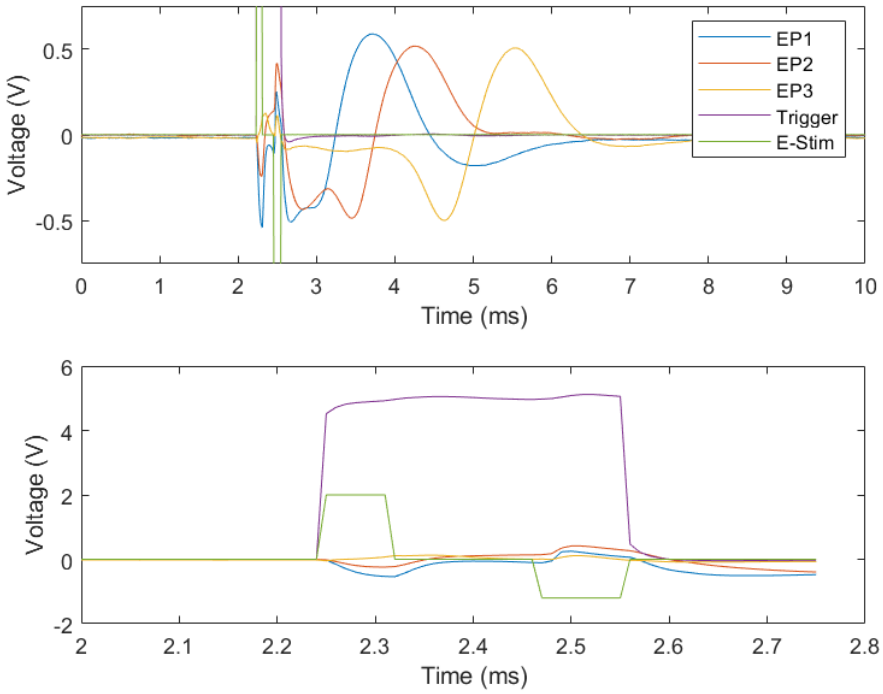

Figure 20 – Example of a successful *ex-vivo* electrical stimulation trial. **a)** Evoked compound action potential traveling through a nerve. Stimulation was performed on EP0 with the biphasic pulse shown in x.b. The temporal distance between EP2 and EP3 is twice that of the time between EP1 and EP2 due to the presence of an unused electrode pair in between EP2 and EP3, doubling the distance between pairs.

Ultrasound Stimulation

In total, 25 nerves were sonicated under varying circumstances. Just as in previous trials, the direct activation of nerves by means of ultrasound has failed in *ex-vivo* experiments.

Schlieren Imaging

It was shown that real-time imaging of the ultrasonication of explanted nerves using Schlieren optics is viable. Keeping part of the nerve outside of the saline bath and connected to electrodes, CAP recordings could be performed. Although sonication did not result in the generation of action potentials, electrical stimulation did, and CAPs could reliably be recorded. Unfortunately, no refraction could be observed when ultrasound passes through the nerve. If it did, this observation could be used to confirm proper allignment of the US focal point and the nerve. This may be different for higher frequencies. However, it is likely medial nerve cords are more sensitive to low-frequency US, following previous findings (Vion-Bailly et al., 2019).

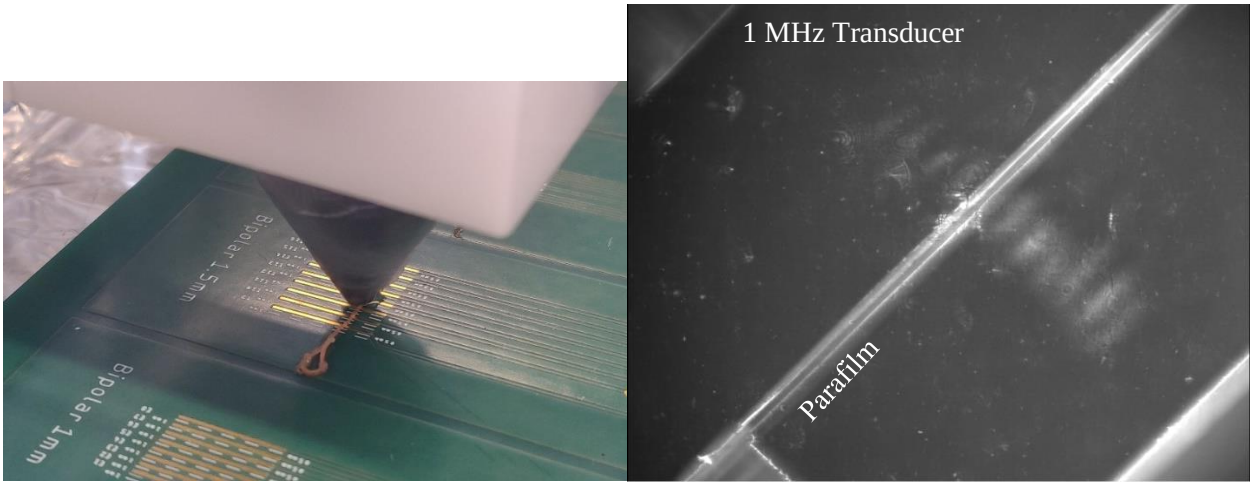

Figure 21 – Photographs of explanted *Lumbricus Terrestris* medial nerve cords under 1 MHz ultrasonication. **a)** The transducer is suspended above the interface PCB and acoustically coupled to the nerve through a coupling cone. The nerve cord is coupled to gold line-electrodes. **b)** Nerve chord under sonication. The nerve is suspended on a thin parafilm in a saline bath. Ultrasound waves were visualized using Schlieren optics. Recording electrodes are not shown.

Ultrasound Power Transfer / Indirect US Stimulation

Four power transfer experiments were conducted. Two resulted in the observation of eCAPs. Rectification of signals harvested by the CMUT array resulted in very sharp, slowly decaying waveforms of up to several volts. This is in stark contrast with the square-wave pulses preferred for electrical stimulation. The time it takes for the US pulse to travel from emitter to receiver is demonstrated by the difference in time between the onset of the reference pulse as compared to the start of the stimulation peak (figure 22).

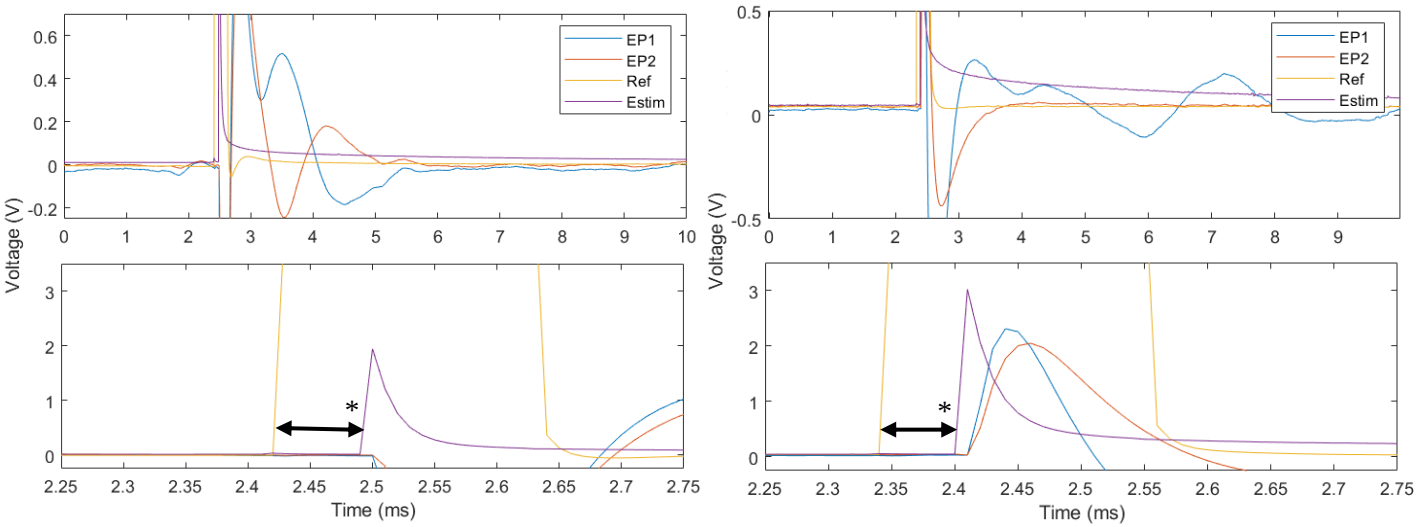

Figure 22 – Two successful indirect electrical stimulation trials in a *Lumbricus Terrestris* explanted medial nerve cord. Power for stimulation was provided by an external ultrasound probe. Upper images show a snapshot of stimulation and the immediate electrophysiological reaction. Bottom images are a magnification of the stimulation phase.

*: Ultrasound pulse travel time, approximately 80 µs.

Discussion

For the validation of ultrasound neurostimulation, an experimental setup was built. This included the design and assembly of an electrophysiological amplification board, neural interface and software. Its functionality was validated with mechanical and electrical stimulation. Four different neurostimulation modalities were performed on a *Lumbricus Terrestris* model for evoked compound action potentials. *In-vivo* trials resulted in successful mechanical and electrical stimulation. However, the goal of stimulating with ultrasound was not met. Transitioning to an *ex-vivo* model resulted in similar findings; explanted nerves showed sensitivity to electrical stimulation but not to ultrasound. Indirect ultrasound stimulation was performed by introducing power transfer. A CMUT device embedded in an ultrasound phantom functioned as a receiving transducer. By sonicating the CMUT, electrical signals were generated. After rectification, these signals were capable of eliciting CAPs in an explanted *Lumbricus Terrestris* medial nerve cord. Finally, it was demonstrated that real-time imaging of ultrasound waves with Schlieren optics is viable in combination with neurostimulation. A setup was devised to sonicate a submerged nerve, while a part of the specimen is coupled to an electrode interface out of the water. Again, no electrophysiological response to ultrasound was observed.

Although engineering objectives of this project were fulfilled by the fabrication and validation of the experimental devices, the main research goal of showing US neurostimulation is still elusive. Out of the many performed trials, none resulted in repeatable evidence of US neurostimulation, even after copying most experimental conditions from publications on US neurostimulation in worms (Jérémy Vion-Bailly, 2015; Vion-Bailly et al., 2019; Wahab et al., 2012). The authors mention waveform with frequencies around 1 MHz, with pulse repetition frequencies around 100 Hz and low duty cycles (5% – 15%) and pressures ranging 0.1 – 6.6 MPa are sufficient to reliably stimulation worm nerves. With the exception of the upper pressure ranges, these conditions were replicated.

An early error in calculating pressures and intensities caused us to assume that the used sonication protocol was indeed in this pressure range. This error was found and corrected only days before finalizing this document, leaving no time to repeat experiments. It was found that the amplifier used in the experiments does not provide sufficient power to the 1 MHz probe due to its operational bandwidth. Transducer characterization results (appendix B) show this clearly, with the maximum output of the 1 MHz probe being slightly above 3 W/cm^2, whereas the 5 MHz probe outputs nearly 100 W/cm^2 at maximum. Substitution of the amplifier or transducer may be the key to positive results in this case. Transducer characterization measurements for the quantification of the influence of using a coupling cone employed a different RF amplifier. These measurements show that a supply voltage of 1 V_{PP} result in intensity values higher than those observed when applying 10 V_{PP} to the amplifier used during most experiments. Additional experiments are planned to be performed soon, the results of which will be presented during the thesis defense

Other causes of failing to elicit CAPs ultrasonically are not ruled out. Small nerves, such as explanted peripheral nerves, are challenging to target due to the necessity to align the ultrasound focal point with the nerve in three dimensions. Some sort of verification, such as Schlieren imaging or the use of a hydrophone close to the target may prove useful. We have shown simultaneous Schlieren imaging and neural recording is feasible, and a continuation of this research line may yield interesting results. In addition to alignment, a correct design of waveforms and choice of neural model are essential to successful investigation into US neuromodulation. Although the peripheral and central nervous system of many species have shown sensitivity to ultrasound, the reason why specific waveforms elicit excitation and others do not is not completely clear. It is likely higher frequencies rely more on the ARF, while lower frequency US is thought to excite or inhibit nerves by a cavitation mechanism.

Ex-vivo trials are significantly more labor intensive than *in-vivo*, because nerves need to be explanted and quickly used. A return to an *in-vivo* model could be made if the electrical artifact problem is solved. Instead of actively shorting the amplifier input lines, a clipper circuit may be introduced to prevent saturation. Clipper circuits employ diodes to prevent voltages from crossing a certain amplitude. This threshold could be set slightly below the saturation voltage of the used amplifiers (5V). Another adjustment to electronics may be warranted in the rectification circuit used in power transfer experiments. These experiments have shown that rectifying the power-transfer signal with a single diode results in a high peak, slowly decaying waveform. Additional circuity may be added to transform the waveform more into a square wave or block pulse.

With the current setup, it seems like we are on the brink of finally seeing positive results. Most issues have been accounted for, and experiments performed in the near future will possibly lead to the observation of focused ultrasound neurostimulation. When this point has been reached, piezoelectric transducers may be substituted with CMUT devices. The Schlieren setup has been designed to fit PCB-mounted CMUT arrays in addition to the currently used piezoelectric transducers. This facilitates neurostimulation experiments with CMUTs. Phenomena such as beam steering could be visualized and correlated to differential neurostimulation. This would allow S. Kawasaki to perform US neurostimulation experiments with CMUT in-house for the remainder of his doctoral research.

It is clear much work is to be done before ultrasound can enter the ranks of neuromodulation technologies next to electrical, magnetic and optogenetic stimulation. However, when it does, it may provide a level of spatial and temporal resolution unrivalled at this level of invasiveness. Additionally, ultrasonic power-transfer may provide existing stimulation technologies with a solution to the battery problem. We have shown that a deeply implanted receiver CMUT combined with a very simple rectification circuit can provide sufficient power to evoke compound action potentials in a simple nerve model. This finding paves the way for further research into what may be called indirect ultrasonic neuromodulation.

Through-Wafer Etching for LF-CMUT

Introduction to Low-Frequency CMUT

Ultrasound waves are typically generated by applying an amplified high-frequency AC signal to a piezo-electric crystal, causing it to vibrate at the frequency of the applied signal. Commonly used piezo-electric materials for ultrasound are barium titanate ($BaTiO_3$) and lead-zirconate-titanate (PZT). An alternative approach to generating ultrasound is through a MEMS-based capacitive mechanism, by means of a capacitive micromachined ultrasound transducer (CMUT). Extensive research has been performed on the fabrication of these devices in the past decades, and it is expected CMUTs will overtake the use of piezoelectric probes in the near future. CMUTs have some significant benefits as compared to traditional piezo-electric devices, such as a wider bandwidth, lower operating voltages and a much smaller form factor. Additionally, CMUT production is easily scalable due to its microfabrication nature. However, difficulties exist for the fabrication of certain devices, specifically those capable of generating low-frequency ultrasound (< 1 MHz). The acoustic spectrum of a CMUT is determined by its membrane size and the membrane gap, with much larger membranes being required for sub-MHz US (Huang et al., 2002). Interest in low-frequency CMUT technology is mostly driven by intended air-coupled use, as opposed to immersion-probes, which are used in a gel or liquid to acoustically couple to the target structure. This is because the attenuation of ultrasound in air is proportional to the square root of the frequency, making low-frequency US much more efficient (Haller et al., 1996).

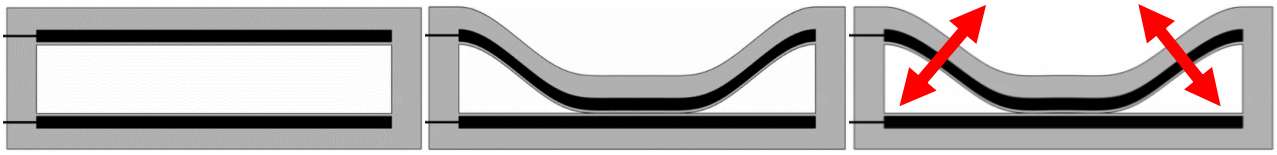

Figure 23 – Cross-section view of a CMUT operating in collapse mode. Grey areas are dielectric material; black lines represent top and bottom electrodes. **a)** Resting state with no applied voltage. **a)** CMUT is brought into collapse mode by applying a high voltage DC bias. The center of the flexible top membrane electrostatically moves to the bottom plate. Electrodes are not shorted due to a thin dielectric layer. **c)** CMUT is driven in collapse mode with an additional AC signal, causing membrane sidewalls to vibrate and generate US.

Several different processes for the fabrication of CMUTs have been developed in the past decades, which can be subdivided roughly into two categories: sacrificial release and wafer bonding. The oldest and most common of the two is the sacrificial release technique, in which a sacrificial layer is deposited on the silicon substrate. On this layer, the top membrane is created, for example by depositing silicon nitride. The sacrificial layer is eventually etched away with a wet-etch process to create an intermembrane gap. This process requires access to the sacrificial layer by means of vent holes in order to allow for the wet etching.

A different approach to CMUT fabrication involves a wafer bonding process. Different wafer bonding methods exist, but all eventually result in the permanent bonding of two wafers. In anodic bonding, electrostatic bonding is achieved by applying a high electric field between two wafers (Knowles et al., 2006). Fusion bonding or direct bonding involves the creation of Si-Si bonds between wafers by an annealing step. Finally, adhesive bonding employs intermediary adhesive layers such as polymethyl methacrylate (PMMA) (Ahmad et al., 2019). Generally, one pure silicon wafer and a silicon-on-insulator (SOI) wafer are involved in these processes. Intermembrane cavities are defined on the silicon wafer, after which the surface is bonded to the active surface of the SOI wafer, effectively sealing the cavity. The SOI wafer can then be etched until only a silicon membrane is left (Erguri et al., 2005).

In the case of low-frequency devices, additional venting is required to relieve the pressure generated by the displacement of the large top membrane. Although vent holes in the top-membrane already been demonstrated for air-coupled applications, backside venting is required in order to use LF-CMUTs in immersion. If the air gap is vented through the back side of wafer, a larger air reservoir may be connected, or devices may even be used with an open backside. The Philips CMUT production flow is based on a sacrificial release process, and thus requires vent-hole etching to make functional low-frequency devices. The goal of this project is to devise a strategy to etch these vents through the backside of the wafer, leaving the functional membrane un-perforated.

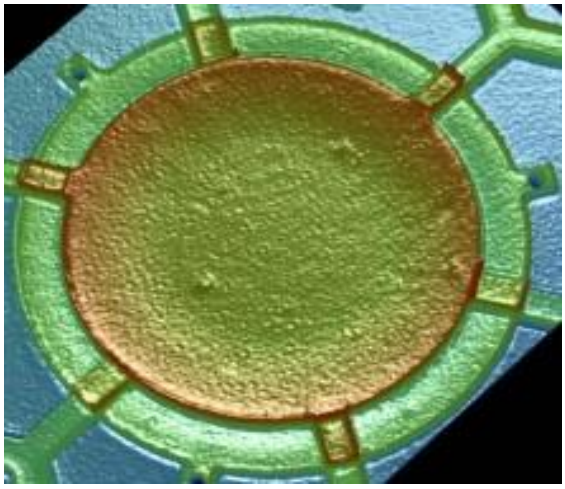

Figure 24 – Micrograph of a single Philips CMUT. Diameter of the inner drum is approximately 100 µm. Six sacrificial release wet-etch vents surround the drum.

Methods

The thickness of double-polished wafers sets the target etch depth of vent holes at 400 µm. However, etching such deep, high aspect ratio features is not straightforward. Requirements include a high etch rate specifically for silicon, a low etch rate for oxide and anisotropy. Arguably the only viable method for such an etch is the Bosch process, which is a variant of deep reactive ion etching (DRIE). This process entails a nearly isotropic plasma etch containing reactive SF_6 ions that is alternated with the deposition of a polymer (polytetrafluoroethylene, $(C_2F_4)_n$) passivation layer. Repeating these steps results in deep, very high aspect ratio etching. Reactive ions are accelerated towards the wafer, where a combination of chemical and mechanical effects result in the removal of silicon. Because of the direction of accelerated ions, mechanical etching is anisotropic and leaves sidewall layers intact. After degrading the bottom passivation layer, chemical effects come into play and silicon is etched at a high rate.

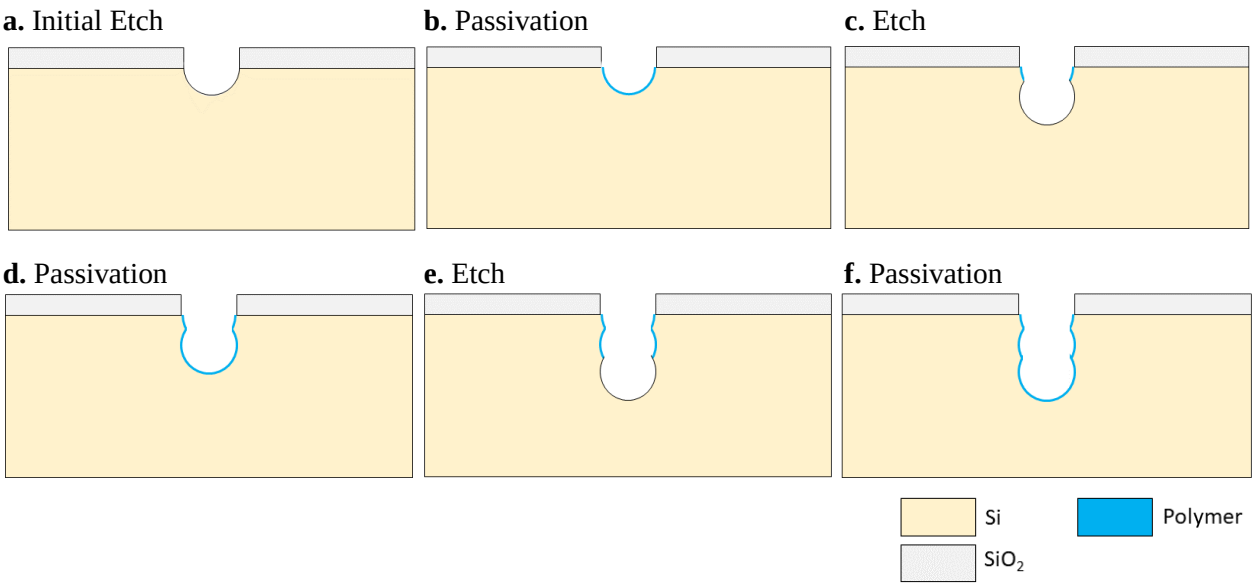

Figure 25 – Illustration of dry etching using the Bosch process. A hard mask of for example SiO_2 is used to define the features. After each etching step, a polymer layer is passivated to protect sidewalls from the isotropic etch. In reality, hese steps are repeated hundreds to thousands of times.

For the etching of backside vent holes, a range of different DRIE etch strategies was investigated in single-polished dummy wafers. Based on observed results, a preferred recipe was chosen and used to etch process-wafers. Etch times were determined based of etch rates observed after conducting preliminary experiments. In order to reduce the required etch depth a trick is used that was originally developed for the flex-to-rigid (F2R) process flow. Instead of etching features entirely through the wafer, they are etched to a certain depth, after which a wider etching window is introduced to effectively "push" the features down (see figure 26.a and 26.b). This is achieved by depositing an oxide layer on the backside of these wafers, and then etching a two-step mask into it. First, smaller features are introduced, after which a frame with equal diameter to the sacrificial layer is introduced and features are advanced onto the silicon substrate.

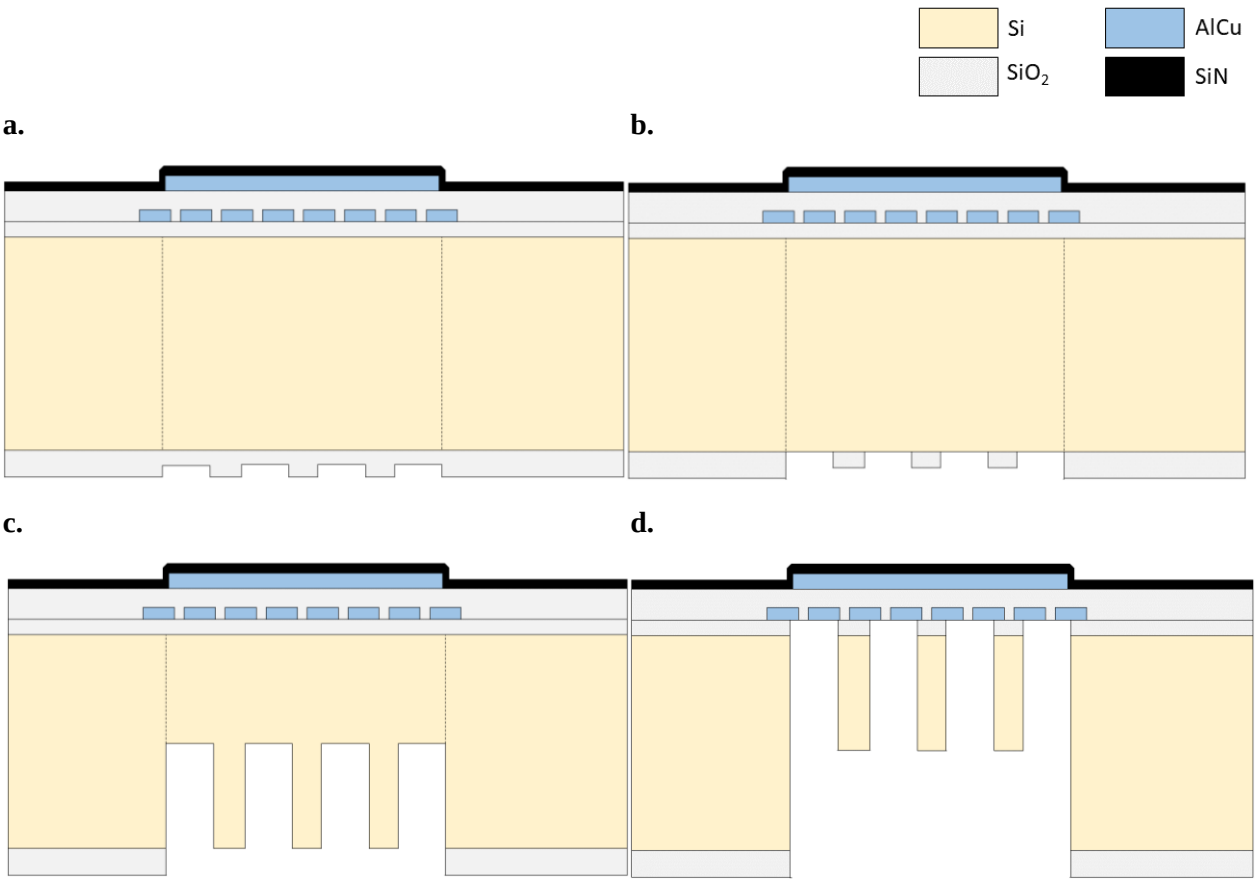

Figure 26 – Illustration of two-step DRIE process. **a)** Features are etched into the backside SiO_2 mask. **b)** Features are advanced into the oxide mask, ending on silicon. **c)** Features are etched halfway through the silicon. This is referred to as a phase A silicon etch in this text **d)** Phase B silicon etch. A larger frame with a diameter equal to the sacrificial layer is opened to allow features to reach target depth with a limited aspect ratio. The complete illustrated process flow can be found in appendix X.

Step number	Description	Processes
1	Etch 3D-allignent markers	Lithography, wet etch
2	Deposit oxide layer for DRIE etch stop	SiO_2 PECVD (1000 nm)
3	Define embedded metal mask	AlCu Sputtering (190 nm), lithography, wet etch, resist strip
4	Deposit oxide layer	TEOS (200 nm)
5	Define sacrificial layer	AlCu sputtering (500 nm), lithography, wet etch, resist strip
6	Deposit oxide layer	SiO_2 PECVD (50 nm)
7	Deposit membrane layer	SiN PECVD (4x 1475 nm)

Table 8 – Summary of processing steps performed on front side of process wafers.

Step number	Description	Processes
1	Define phase A hard mask	SiO_2 PECVD (2000 – 4000 nm), lithography, dry etch (1000 – 2000 nm), resist strip
2	Define phase B hard mask	Lithography, dry etch (1000 – 2000 nm)
3	Deep silicon etch phase A	Si DRIE (200 µm), SiO_2 dry etch (0 – 2000 nm)
4	Deep silicon etch phase B	Si DRIE (200 µm)
5	Etch oxide through embedded mask, landing on sacrificial layer	SiO_2 dry etch (1200 nm)
6	Sacrificial release	AlCu wet etch

Table 9 – Summary of processing steps performed on backside of all wafers. Note that photoresist is not stripped after defining the phase B hard mask. This introduces an etch buffer for the phase B etch.

Prior to fabrication, a process flowchart and lithography masks were designed. Because the current experiment builds on an existing fabrication method, previously designed masks could be used for most front side processing steps. Two additional masks were designed to facilitate the novel backside dry-etch. These masks were made to etch multiple different features on the same die, allowing the examination of different geometric and dimensional combinations of features. This resulted in a total of 12 different combinations between embedded metal masks and DRIE masks. Illustrations of the used mask can be found in Appendix B. Initial experiments were performed on single polished, 600 µm thick dummy wafers to reduce the amount of required process wafers. After determining a suitable etch strategy, the transition to front-processed wafers was made.

Results

Experimental outcomes are presented on a chronological trial-by-trial basis, because finding the correct fabrication parameters (oxide mask thickness, DRIE recipe etc.) required an iterative approach. Each experiment provided valuable information on how to continue. A total of 8 dummy wafers and 12 process wafers was processed

Front Side Processing of Membrane Structures

Processing the front side of process wafers to add the embedded AlCu mask, sacrificial layer and nitride top membrane was successful.

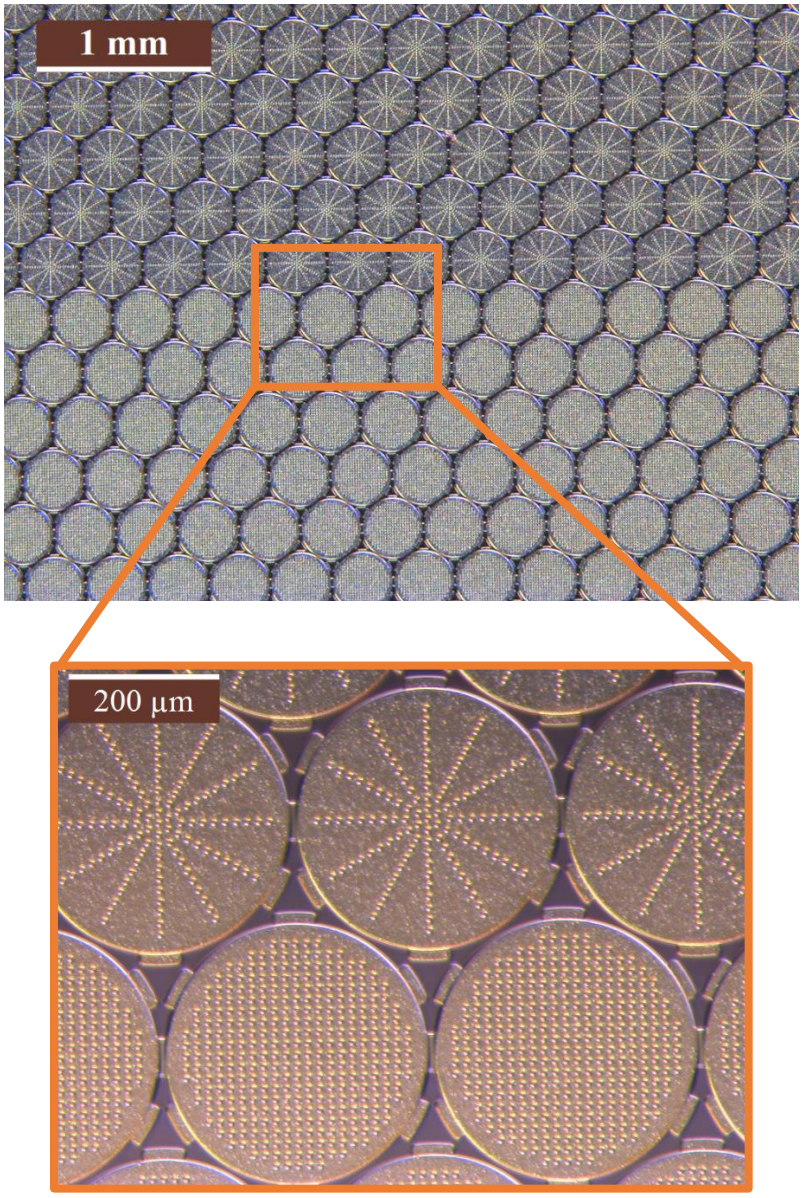

Figure 27 – Micrographs of front side structures. Embedded metal masks are visible through the nitride membrane.

Experimental Etch 1

Initial silicon deep-etch results in dummy wafers revealed several important findings for following experiments. First, simple visual inspection of etched wafers reveals an expected issue: a non-uniform etch rate exists across the wafer, clearly visualized by a color gradient due to different oxide thicknesses (figure 28.a). Although the etch is intended for silicon, the hard mask is also etched non-specifically. More importantly, the current combination of hard mask thickness (2 µm) and recipe is not sufficient. Both oxide and photoresist were consumed by dry etching before reaching the target depth of 200 µm, as revealed by spectroscopic reflectometer measurements (NanoSpec, ToHo Technology). This indicates the necessity for a DRIE recipe that has a higher specificity for Si over SiO_2, or a thicker oxide mask combined with longer etching. Additionally, a variable etch rate depending on feature size was expected. Indeed, more narrow features etch significantly slower, with the smallest features etching at approximately 60% the rate of the largest (figure 28.c). This represents a necessity to over-etch, allowing smaller features to a depth of 200 µm. A positive observation is the excellent lack of tapering. The current recipe has shown to generate very straight features, as shown by figure 28.a and 28.b.

Material	**Etch rate (nm/min)**
SiO_2 (PECVD)	20
Si	2400 - 3200

Table 10 – Recipe-specific etch rates for silicon and silicon oxide as calculated for experiment 1.

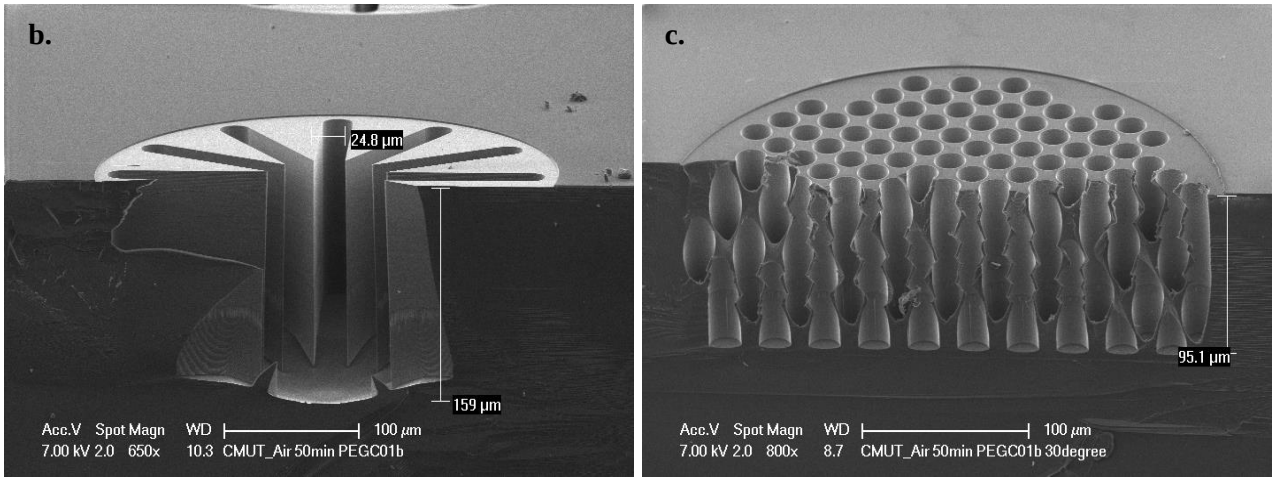

Figure 28 – Results of first silicon deep etch (40 minutes) as SEM cross-sections. **a)** Non-uniform etch rate for deep etch results in a heterogenous consumption of the oxide mask, made visible by a color gradient due to resulting difference in oxide thicknesses. **b)** SEM of cross-section for structure 1B. Due to the large connected features, etch rate for 1B is the highest out of all structures (~4 µm/min). **c)** SEM of cross-section for structure 2/3C. Small holes reduce etch rate, making this structure the slowest to etch (~2.4 µm/min).

Experimental Etch 2

Based on previous results, two additional deep etch strategies were implemented. Instead of increasing the oxide thickness, DRIE parameters were varied to attempt to increase etch specificity for Si and decrease the difference in etch rates dependent on feature size. Four dummy wafers were processed up to and including phase A Si deep etch, after which they were broken and SEM cross-section were imaged.

As can be seen in figure 29, a clearly visible problem arose. Unlike results from experiment 1, where only the expected phase A etch was visible, this recipe already shows phase B features after the first etch. The second etching phase started prematurely due to full consumption of the oxide mask. Although features are etched significantly deeper than in the previous trial, this comes with a higher etch-rate for SiO_2 as well. Thus, continuing with this recipe would require a significantly thicker oxide mask. A final observation is the inadequate etching of passivation layers, resulting in pillar-like structures. This should not present a serious challenge, as they should be removable with an additional etch.

Material	Etch rate (nm/min)
SiO_2 (PECVD)	31 - 34
Si	3000 - 4000

Table 11 – Recipe-specific etch rates for silicon and oxide as calculated from experiment 2.

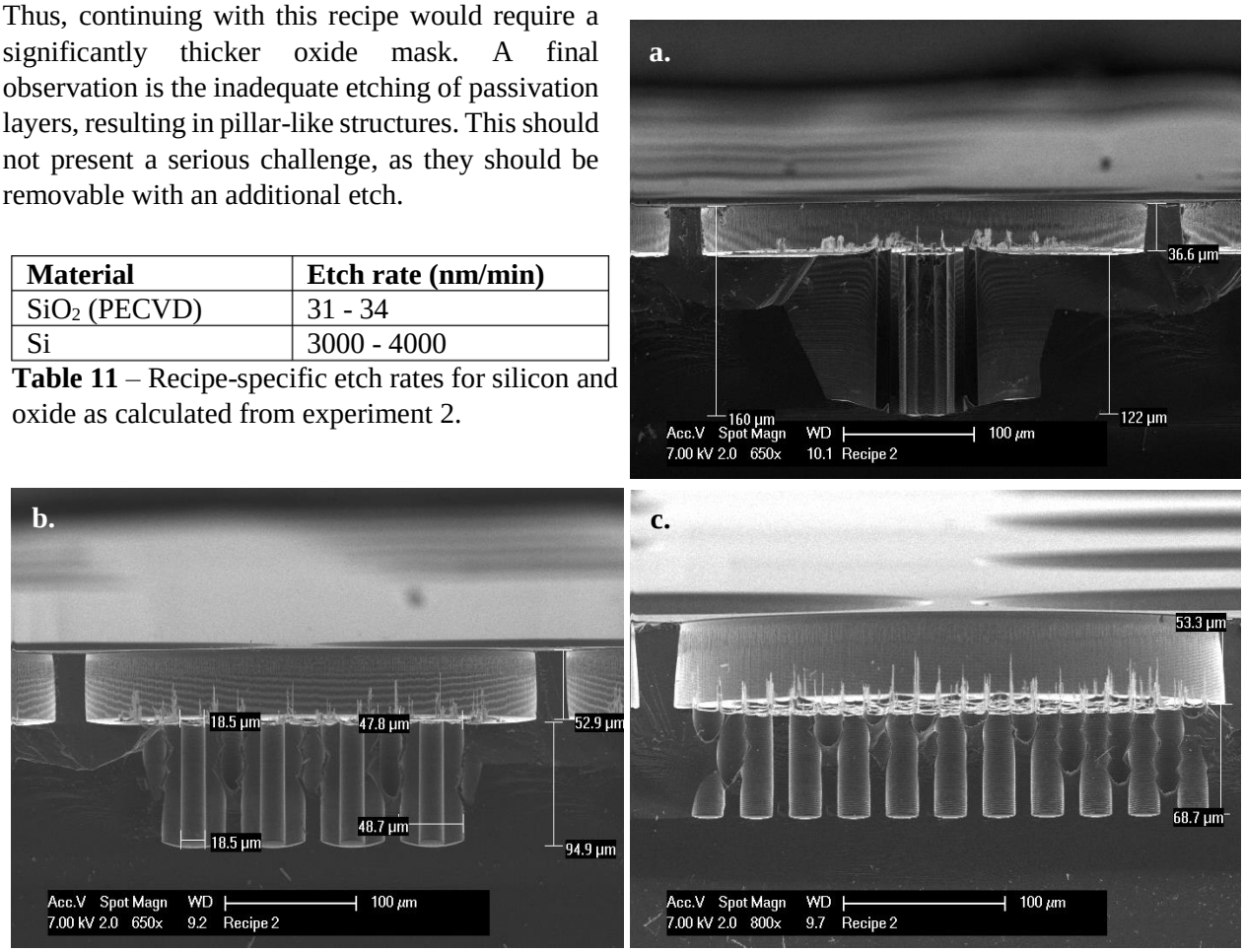

Figure 29 – Results of second silicon deep etch (40 minutes) as SEM cross-sections. All structures show premature etching of Phase B structures due to consumption of oxide mask. **a)** Cross-section of structure 1A. Total etch depth is similar to that in experiment 1. **b)** Cross-section of structure 3B. Total etch depth is nearly identical to 1A, indicating a higher uniformity in etch rate with regards to feature size. **c)** Cross-section of structure 2/3C. Total etch depth is significantly lower than for 1A and 3B.

Experimental Etch 3

Recipe 3 at 70 minutes resulted in an etch depth very close to the target. All features were etched to a depth of 200 µm +- 5%. However, SiO_2 was consumed at a rate similar to experiment 2. Combined with the longer etch time, this resulted in the early consumption of the first hardmask layer. Failures similar to experiment 2 are more pronounced here, as the majority of etch time is spent prematurely etching phase B. Additionally, tapering is a visible issue. For smaller features, structural integrity and functionality is lost due to etching of sidewalls. From current data, it cannot be concluded whether this is a result of phase A or phase B etching. These results indicate the inadequacy of this recipe for the current application.

Material	**Etch rate (nm/min)**
SiO_2 (PECVD)	31
Si	2800 - 3000

Table 12 – Recipe-specific etch rates for silicon and oxide as calculated from experiment 3.

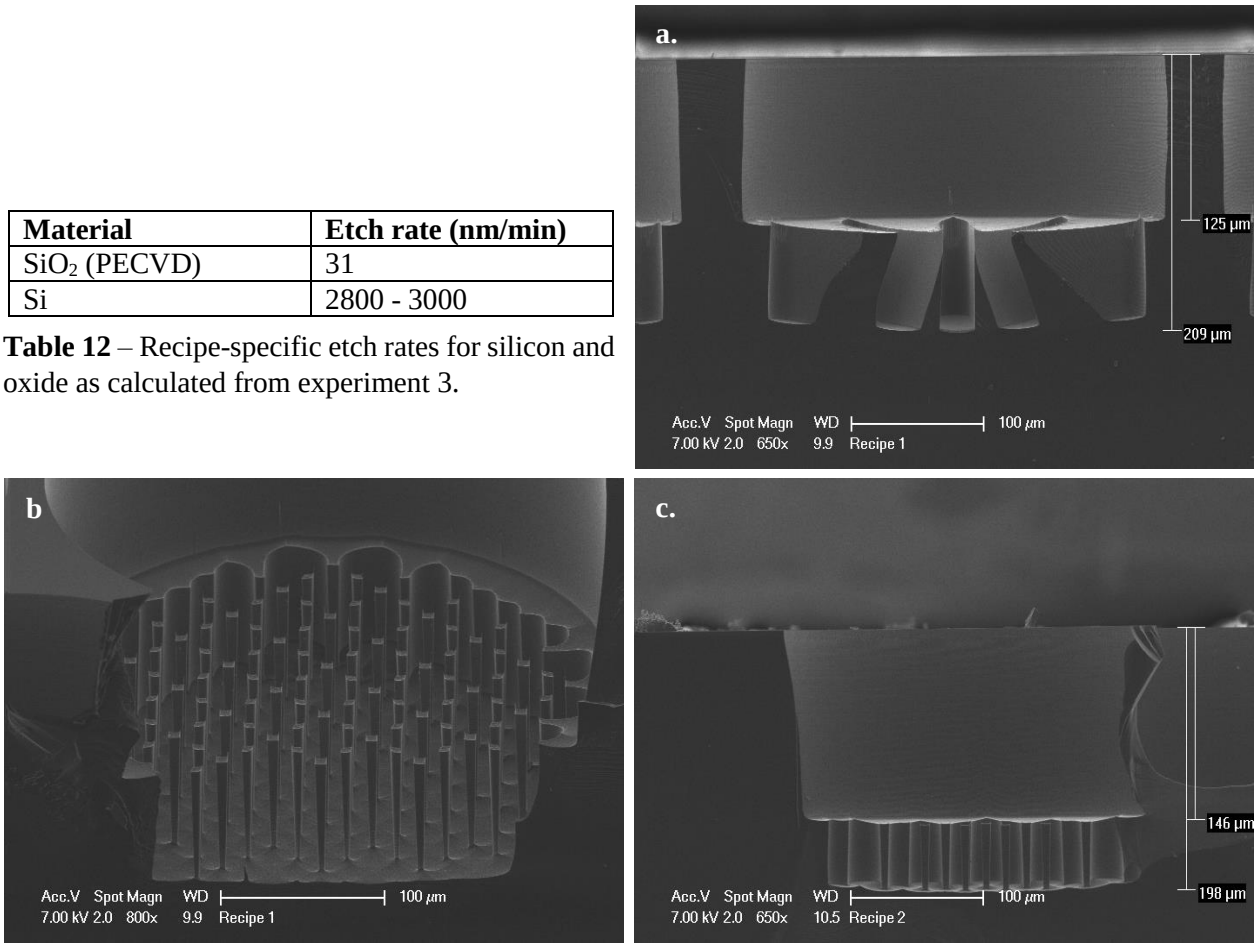

Figure 30 – Results of third silicon deep etch (70 min) as SEM cross-sections. **a)** Structure 1B. Premature phase B etching of experiment 2 is exacerbated here, as the majority of the depth is due to phase B etching, again due to total consumption of hard mask. **b)** Small features connect in the lateral dimension. This is an unwanted effect, and signifies that this recipe is not suited for this application. **c)** Structure 3B.

Experimental Etch 4

The recipe used in experiment 2 was chosen to use in further trials. One reason is the minimal difference in etch speeds between structures, with the exception of 2C, 3C and 4C structures. These are the smallest features and were included as a lower bound reference to verify the necessity of etching larger structures instead of small hole directly to the embedded mask. From this point onwards, they will not be considered anymore. The second reason for this choice of recipe is the straightness of etched features, showing almost no tapering. A downside is the relatively high etch rate for SiO_2, which means a thicker oxide layer will be necessary. Backsides of all wafers were stripped, and a 4 µm oxide layer was deposited, after which phase A and phase B hard masks were patterned and etched. The duration of phase A and B etches was increased to 52 and 60 minutes respectively.

Phase A shows performance as expected from previous results. The thicker oxide mask allowed for a deeper etch. Most features, with the exception of 2C, 3C and 4C, were etched close to the target depth (200 µm +- 5%). However, phase B etching reveals the consumption of sidewalls, which effectively removes features and renders phase A etching of no use.

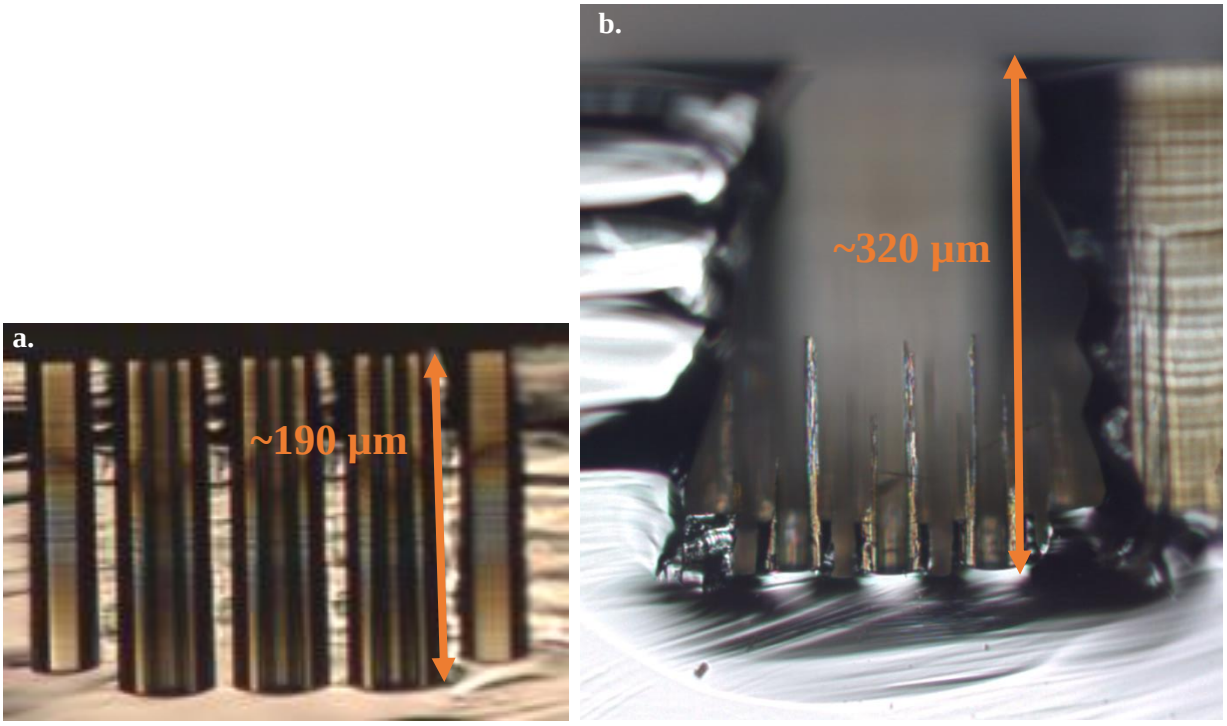

Figure 31 – Light-microscopy images of 3A structures after fourth etch experiment. Due to maintenance issues at the time of completing these experiments, SEM images could not be generated. **a)** Cross-section after phase A etch. A high quality etch is revealed, with no tapering and excellent etch depth. **b)** Cross-section after phase B etch. First, it is clear that the goal depth of 400 µm was not reached. More importantly, phase B etching has consumed sidewalls that were defined by phase A. Only slight remainders of these structures remain in the form of thin silicon pillars.

Discussion

From current results, it is clear deep reactive ion etching (DRIE) is not a straightforward process. Feature shape and size have a direct, non-linear effect on local and global etching rates. This means that nearby features affect the rate at which a certain feature is etched. The primary mechanism here is saturation of SF_6. If all injected gasses are reacting to Si, hard-to-reach structures such as deep features will etch significantly slower. Because many different feature shapes were experimented with in this trial, widely differing etch rates were observed. However, it was shown that most features can be etched deep into the silicon, with little to no tapering. Finding an etch recipe that would be suited for all combined features on these wafers is most likely a useless pursuit. Further research should choose one or several similarly performing feature shapes and focus only on those. This would allow optimization of the process flow for these specific design choices.

Attempting to perform phase B etches, in which previously etched features are advanced into the silicon, it was found that structures are mostly lost. They are consumed by this etch step, indicating inadequacy of the passivation layers. To remedy this, a new recipe would have to be developed which deposits a thicker polymer. It is possible one of the previously tested etch strategies for phase A could be suited for a phase B etch, and it is worthwhile to investigate. Because of the failure to reach embedded structures, we were not able to perform a dry-etch of the embedded SiO_2 layer, nor did the sacrificial layer get etched. However, 8 wafers with completed front-side processing and back side oxide masks remain and present an opportunity to easily continue this line of inquiry.

Conclusion

The current project entailed the design and assembly of a system capable of recording local field potentials in a *Lumbricus Terrestris* neural model for evoked compound action potentials, with the goal of showing a proof-of-concept for US neuromodulation. We were able to reliably elicit compound action potentials both *in-vivo* and *ex-vivo* with electrical stimulation. Additionally, CMUT devices could be used to harvest acoustic energy supplied by a medical probe, to be used for electrical stimulation. However, no positive results were found for direct ultrasound stimulation. Additionally, a two-step silicon deep etch for backside venting in low frequency CMUT devices was attempted. Only the first step of the process (phase A) was shown to be successful. Attempting to advance features into the silicon using a large diameter etch window resulted in consumption of smaller features and a severely limited etch rate. The latter was to be expected, since using larger masks exposes more silicon to the reactive ions, saturating them.

The maturation of CMUT fabrication and the exponentially rising interest in ultrasound neurostimulation combine to form a novel research space. The idea of miniaturized ultrasonic devices being used for power transfer, imaging and interventional sonication is certainly an exciting promise, and it is highly likely patents and research publications proposing novel neurostimulation devices will be plentiful in the near future. However, direct US neurostimulation, without transduction into the electrical domain by a receiver, is still far from being used clinically. A major reason is the lack of fundamental understanding of the biophysical mechanisms. Although several mechanisms such as cavitation and ARF induced sonoporation, ion-channel opening by shear stresses and capacitive currents have been proposed, it is still unclear to which degree each mechanism is responsible for transducing acoustic waves into ionic transients. Current data suggest a differential sensitivity to US between tissue types, which may cause trouble when translating pre-clinical findings to use in humans.

When CMUT neurostimulation devices reach a point of commercial validity, and US is further developed as a neurostimulation technology, it is likely that non-invasive, externally worn devices will employ low frequency ultrasound due to the reduced attenuation at lower frequencies, allowing deeper structures to be targeted. When very high spatial resolution is required, high frequency devices may be implanted. This may be advantageous when stimulating a highly heterogeneous structure, where the larger low-frequency focal point causes unwanted side effects. This is certainly the case for structures such as the vagal nerve, which contains efferent fibres running to almost every organ in the body, while only having an approximate cross-sectional area of 7 mm^2. In such circumstances, a cuff-shaped CMUT device may be wrapped around the nerve, allowing steered sonication from each angle.

Appendix A: Software

LabVIEW code documentation

This data acquisition and stimulation program was written in LabVIEW 2018 and consists of several Virtual Instruments (VIs), namely a main VI and several subVIs.

VI Overview

Main - Contains the general structure of the program, including all subVIs and a user interface (UI). Initializes all parameters, arrays and input tasks. Additionally, it deals with keeping the data buffer at an appropriate size and closes and clears all tasks when the program is stopped. Runs iteratively at a frequency which can be adjusted to accommodate available processing power.

Initialize Tasks - Running a data acquisition system (DAQ) in LabVIEW is done with tasks. These tasks are function- and channel specific and run through several subVIs in order to either acquire or output signals. The *Initialize Tasks* subVIs creates all necessary output tasks and assigns them to a physical channel. These channels can be specified from the main UI. Triggers are initialized for each output such that they can all fire simultaneously when the appropriate trigger signal is generated. This VI also generates an array containing information on which type of stimulation will be performed during the experiment (trigger array). This array will later be used in the *Stimulation Output* VI to trigger the specified stimulation channels. This can be either electrical or ultrasound stimulation.

Biphasic Interphase Delay Generator - Generates a biphasic square waveform used for electrical stimulation. The amplitude and width of the positive and negative phase of the waveform can be adjusted. Additionally, a delay can be introduced in between phases. Interphase delays in electrical stimulation have been shown to restore the excitation threshold of neural tissue to more normal values as compared to simple biphasic stimulation. (Merrill et al., 2005). This waveform can be adjusted online in order to perform different types of electrical stimulation in a single experiment.

Stimulation Output - Handles all outputs. This VI takes the output tasks, trigger array, biphasic waveform and several output parameters and communicates to the DAQ what to output. This is done by sequentially starting each task and finally generating the trigger signal.

Snapshot - Whenever the stimulation output button is pressed, a snapshot is taken of a specified number of samples. This allows the user to immediately see the electrical response to stimulation. Saving can be enabled so that each snapshot is automatically saved to a tab-delimited file.

Save - This VI handles file saving. It can be toggled with a button and writes acquired data to a tab-delimited file. Data is split over files of 500 megabyte to keep them manageable for post-processing.

User Manual

Prior to running the program, several settings need to be configured. Most importantly, the sampling parameters need to be set in the "Recording" tab. The sample frequency determines the highest detectable frequency as follows according to Nyquist's Theorem:

Eq. A.1
$$f_{max} = \frac{f_s}{2}$$

where f_{max} is the highest detectable frequency and f_s the sampling frequency. Since both stimulation and recording are dependent on this variable, it also sets the lower limit for stimulation durations. This means a higher f_s will allow for detection of higher frequency signals and the output of shorter pulses. However, sampling at very high frequencies inflates the size of measurement files and complicates post-processing. Additionally, depending on whether data is saved, the PC might not be able to keep up with very high sample frequencies and crash. The second sampling variable is the amount of samples recorded for each iteration. This number is inversely related to the speed at which the program runs by the following relation:

Eq. A.2
$$f_i = \frac{f_s}{N_s}$$

with f_i being the iteration frequency and N_s the number of samples acquired each iteration. Setting N_s too low will cause buffering issues. The PC running LabVIEW will not be finished with its current iteration while all samples have already been collected. This causes the DAQ to send the next samples to the PC before it is done processing the previous set and causes a buffer overflow with the following error code: *-200279*.

In case stimulation is performed, the type of stimulation (ultrasound, electrical) will need to be selected prior to running the program as well. This can be done in the second tab named "Stimulation". Finally, in the "Settings" tab, in- and output channels can be changed. In most cases, however, this will not be necessary due to the fact that they have been pre-selected for use with the Neuroboard.

While running, acquired samples will be displayed on the recording tab. The topmost graph shows samples recorded in the current iteration, and is useful for checking noise levels. Below that, two snapshot graphs can be found. By pressing "Stimulation Trigger", besides performing all pre-determined stimulation protocols, a snapshot of the moment of stimulation is taken and displayed together with the power spectral density (PSD) of channel 0 (EP0). This way, the user can immediately read out the electrical response to stimulation. On the bottom of this tab, there are four lines (one for each channel) displaying a part of the recorded data. The length of this buffer can be edited in the settings tab.

In the stimulation tab, all stimulation parameters, the electrical stimulation waveform and a snapshot window can be found. By default, all parameters are set to generate biphasic unbalanced stimulation with an interphase delay. However, the interphase delay and multipliers for the second phase of the pulse can be changed. By setting both the amplitude and width fraction to 1, a balanced biphasic waveform is generated. Setting these fractions to zero will result in a single phase waveform. By changing the interphase delay to 0, it is effectively removed from the waveform. However, this is not advised since the abrupt change of polarity can cause irreversible redox reactions in your specimen.

User Interface

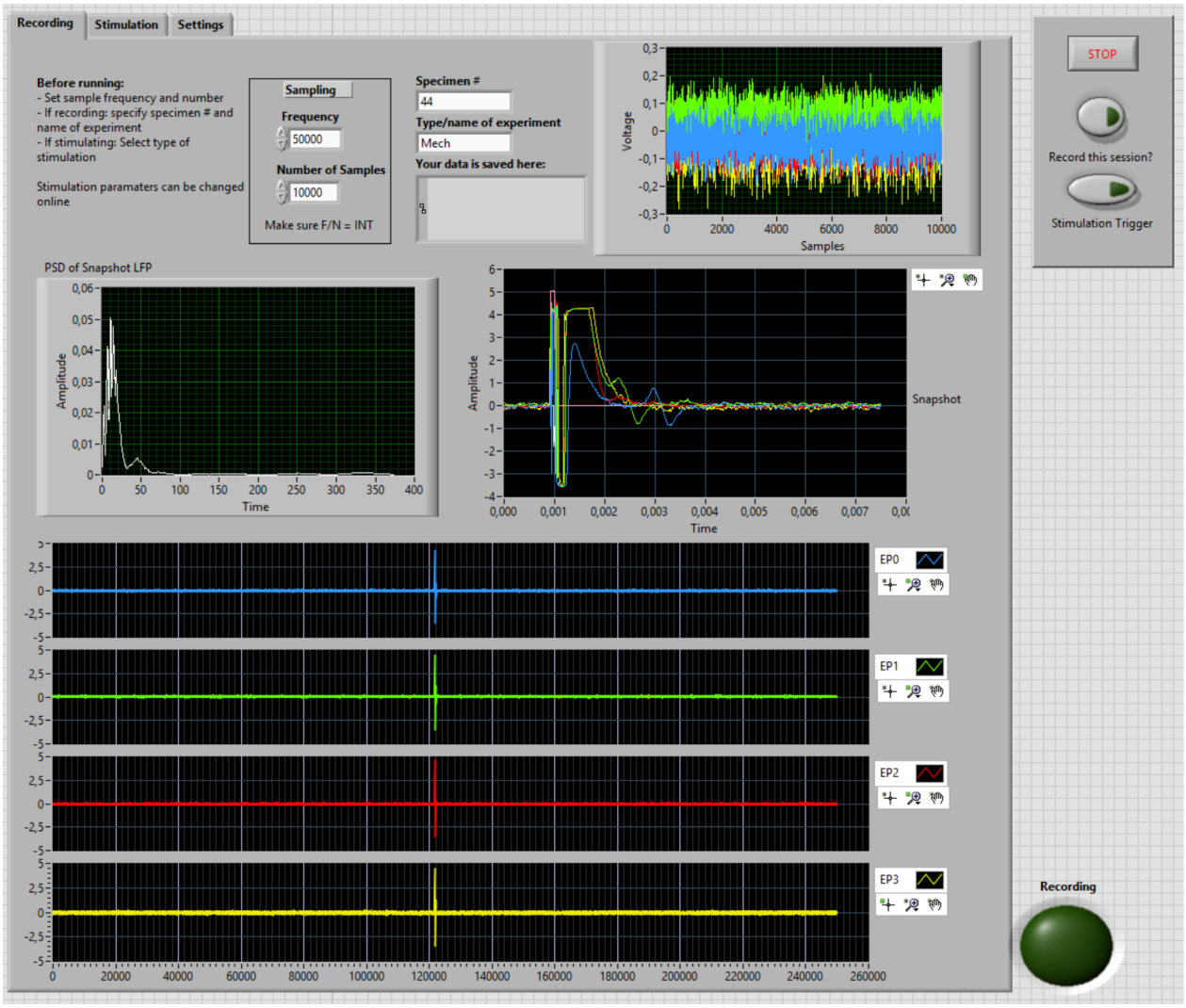

Figure A.1 – UI front panel with example data. Frequency and number of samples per package can be adjusted. Specimen number and experiment name specify the folder- and filename of the files generated when recording is enabled.

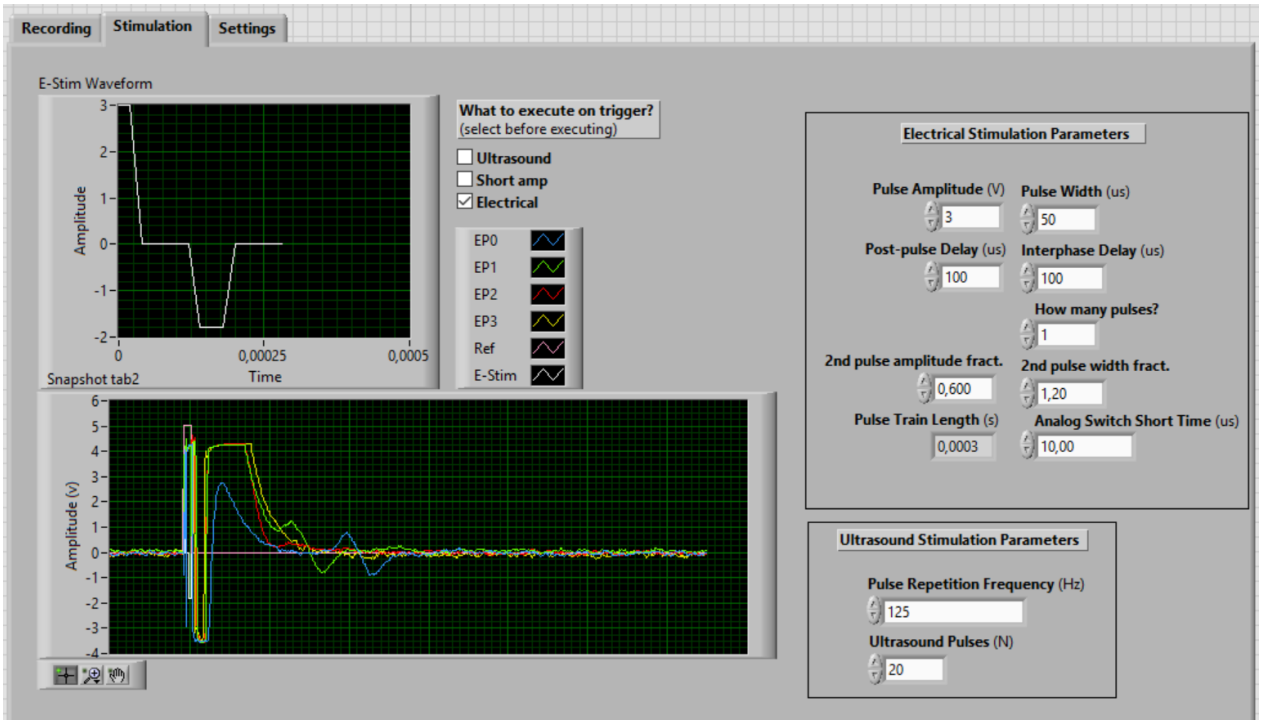

Figure A.2 – UI of stimulation tab. An example of a stimulus waveform and LFP reaction can be seem in the graphs. Here, stimulation modality and parameters can be adjusted.

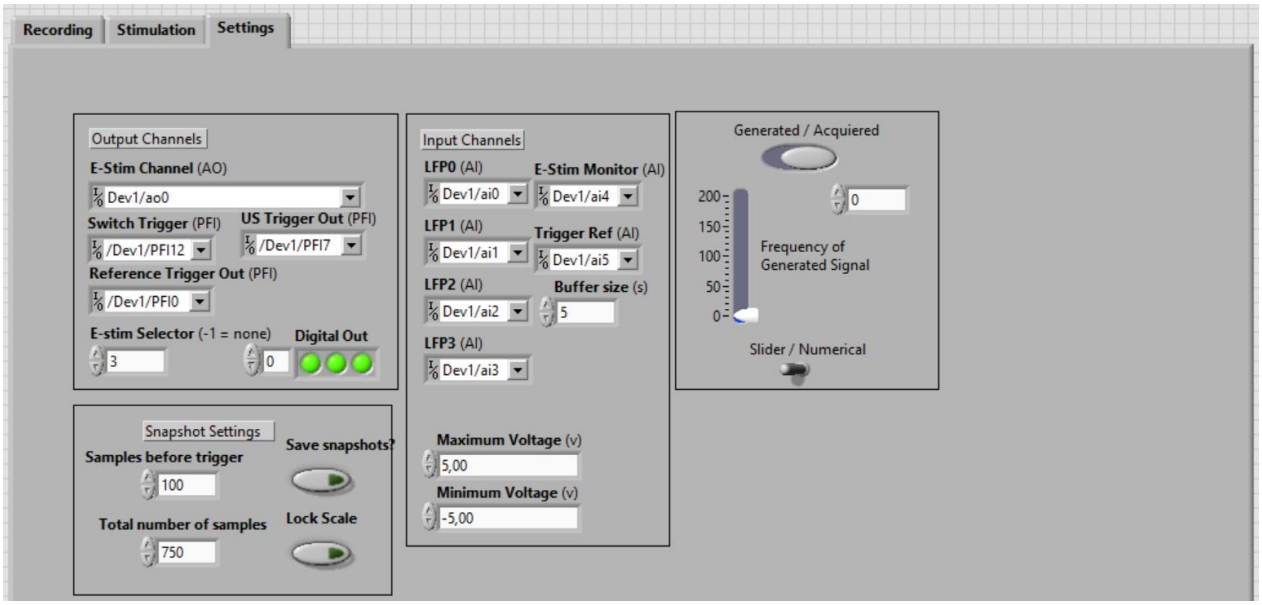

Figure A.3 – Settings UI. Physical channels and several general parameters can be set here. The channel used for electrical stimulation can be selected, together with all the output channels. Snapshot settings allow for the customization of the length and spacing of the acquired snapshot during stimulation. Enabling "Save snapshots" will automatically save each snapshot into a file separate from the main recording file. A switch labeled "Generated/Acquired" can be found on the right, and when set to "Generated", will generate a sin-wave and feed it into the data acquisition line of the program, instead of sampling data from a DAQ. This can be used for debugging or demonstration purposes.

LabVIEW Code Documentation

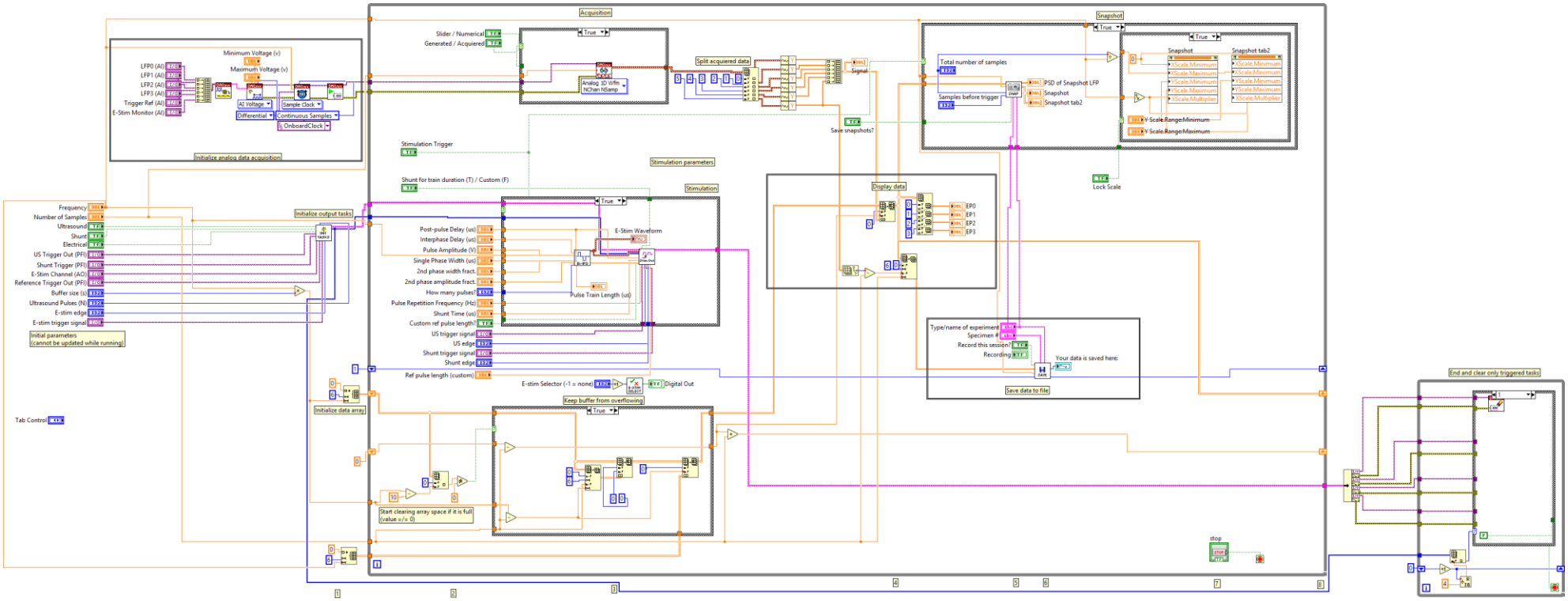

Figure A.4 – Main structure of LabVIEW program. Contains data acquisition structure, data sorting, all subVIs and all variables.

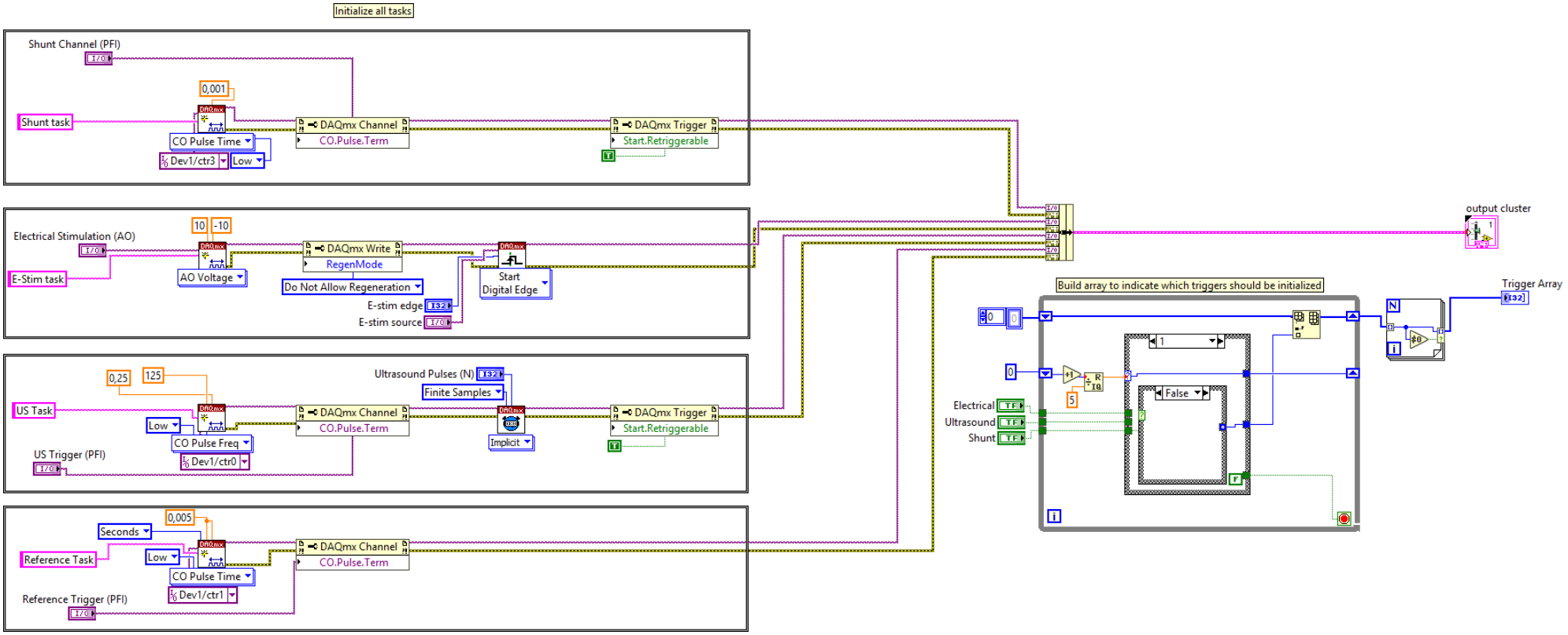

Figure A.5 – Initialization subVI. Specifies all physical in- and output channels and builds an array specifying which channels should be included in trigger signal.

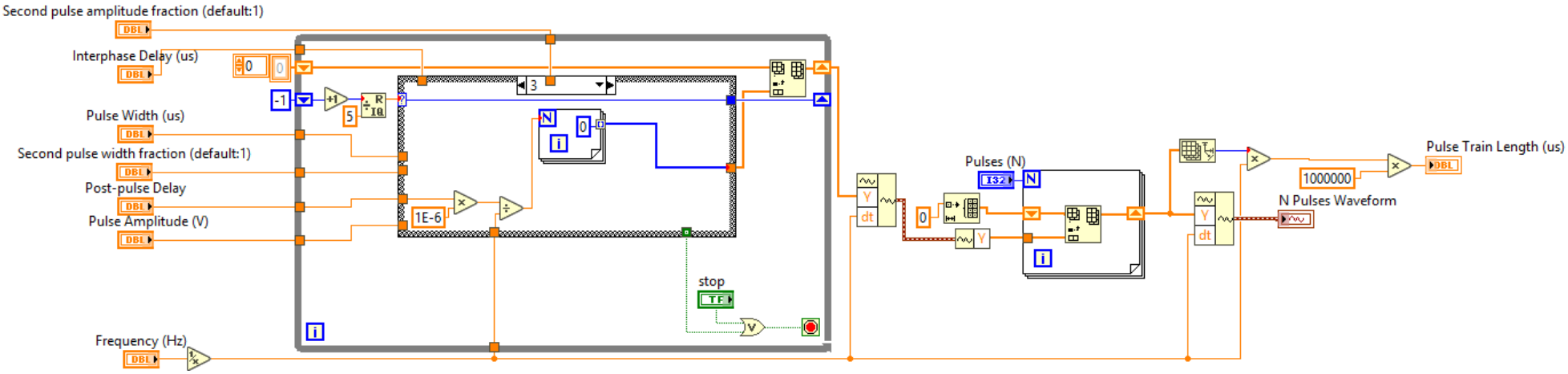

Figure A.6 – Electrical stimulation pulse generator. Builds a waveform array from several parameters.

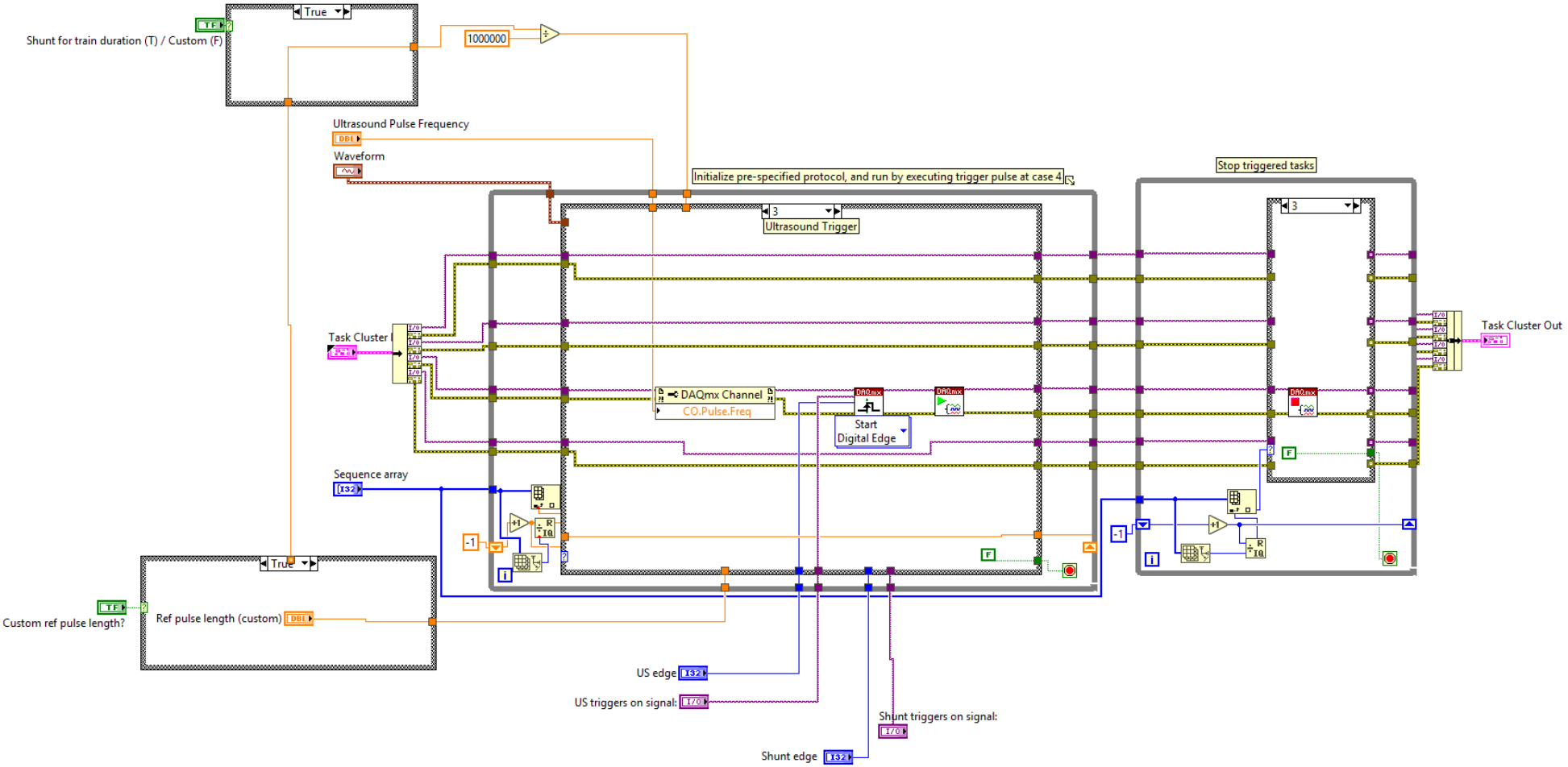

Figure A.7 – Custom DAQ output. Contains all output functions for DAQ. Uses the trigger array to determine which outputs should be activated upon trigger signal.

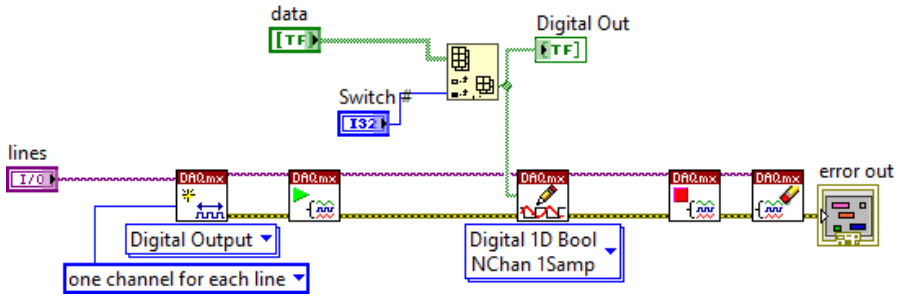

Figure A.8 – Electrical stimulation selector. Uses Boolean input to determine which electrode pair to use as stimulation channel.

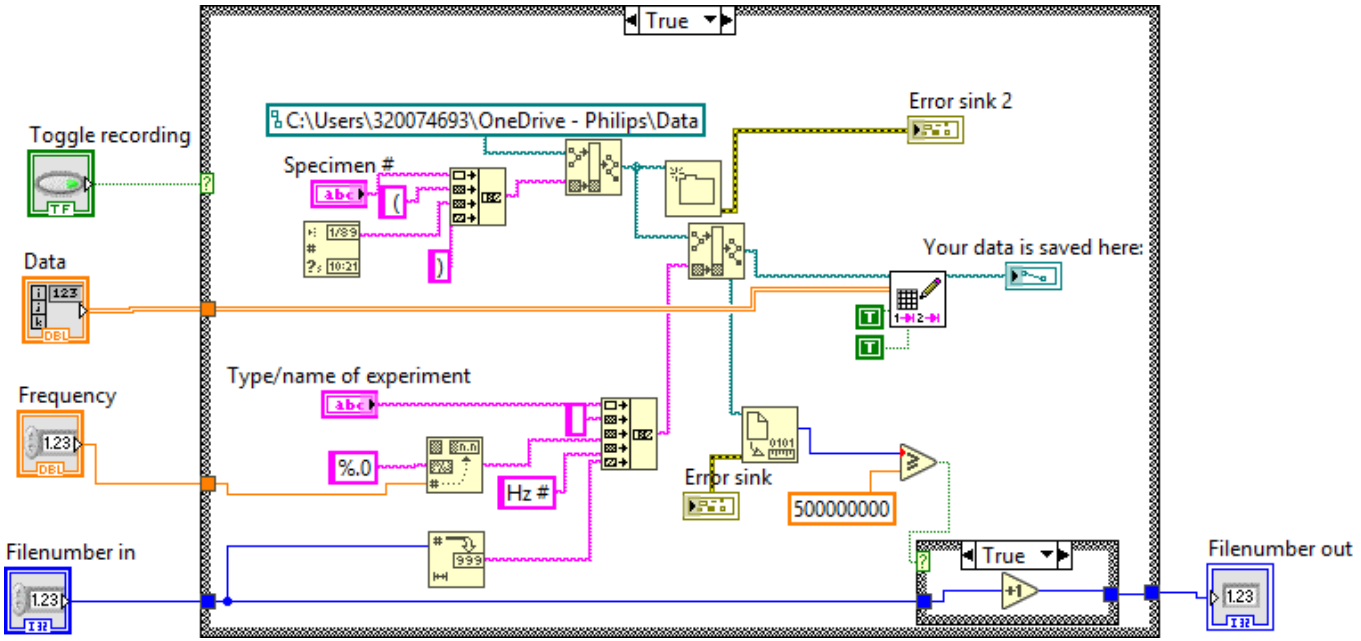

Figure A.9 – Filesave subVI. Specifies filename and path string to use when saving data.

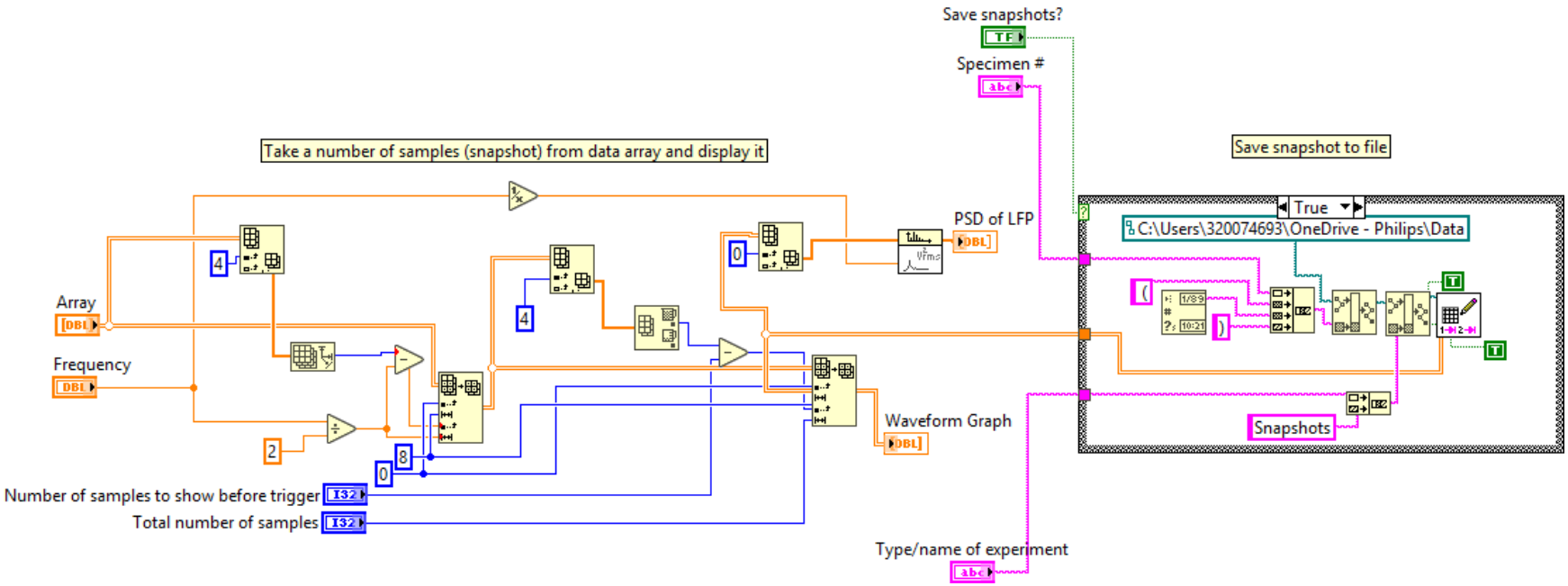

Figure A.10 – Snapshot subVI. Determines which part of acquired data to show in UI after triggering a stimulation protocol. Snapshots may be saved to a file separate from the main recording file

Appendix B: Transducer Characterization

Methods

To quantify the energy supplied to the tissue, intensity measurements were performed on all US transducers used for the neurostimulation experiments. Two different measurements were performed: the first one to verify that a coupling cone does not interfere with acoustic conduction and a second to measure the pressure at several supply voltages and coordinates. For each trial, intensity values were calculated according to equation 3 and plotted as heat maps using Matlab R2019a (The Mathworks, Natick, Massachusetts).

Intensity Measurements

The measurements were performed submerged in degassed water using an NH0500 hydrophone needle (Precision Acoustics, Dorchester UK) powered by a Hydrophone Booster Amplifier (Precision Acoustic, Dorchester UK). The transducers were driven with a 16-cycle sinusoidal waveform at their respective center frequencies using a 25W, 50 dB RF amplifier (ENI 525LA). The hydrophone needle was manually positioned at the focal point, where intensity is highest. From this point, two-dimensional scans were performed in a grid of 7 by 11 measurement points. At each point, the amplifier was driven with 10 different voltages (1V to 10V).

Coupling Cone

For experiments where specimens are not immersed in saline or water, acoustic coupling is achieved with a coupling cone filled with ultrasound gel. In order to verify that the (absence of) gel nor the sidewalls of the coupling cone interfere with acoustic conduction, two sets of intensity measurements were performed in which all parameters are kept constant except for the presence of the coupling cone. Two-dimensional scans were performed in a grid of 6 by 16 points. Pressure was measured for four different driving voltages (1V to 4V) at each point. Because the coupling cone hinders measurements between the transducer and focal point, measurement points are unavailable for that region.

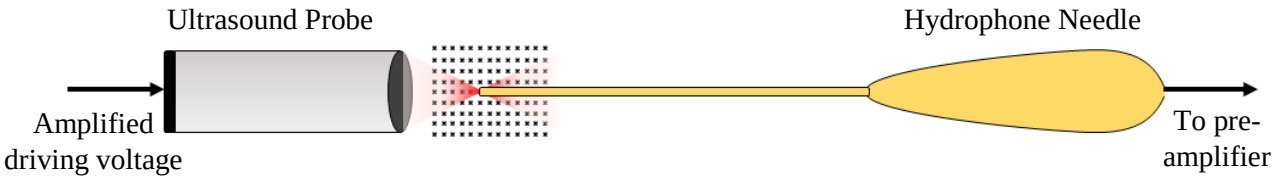

Figure B.1 – Illustration of hydrophone measurement hardware. Black crosses represent measurement locations. Not to scale.

Results

Results for the characterization of piezoelectric ultrasound probes are presented as heat maps of intensity, and graphs of the intensity versus supply voltage.

Influence of the Coupling Cone

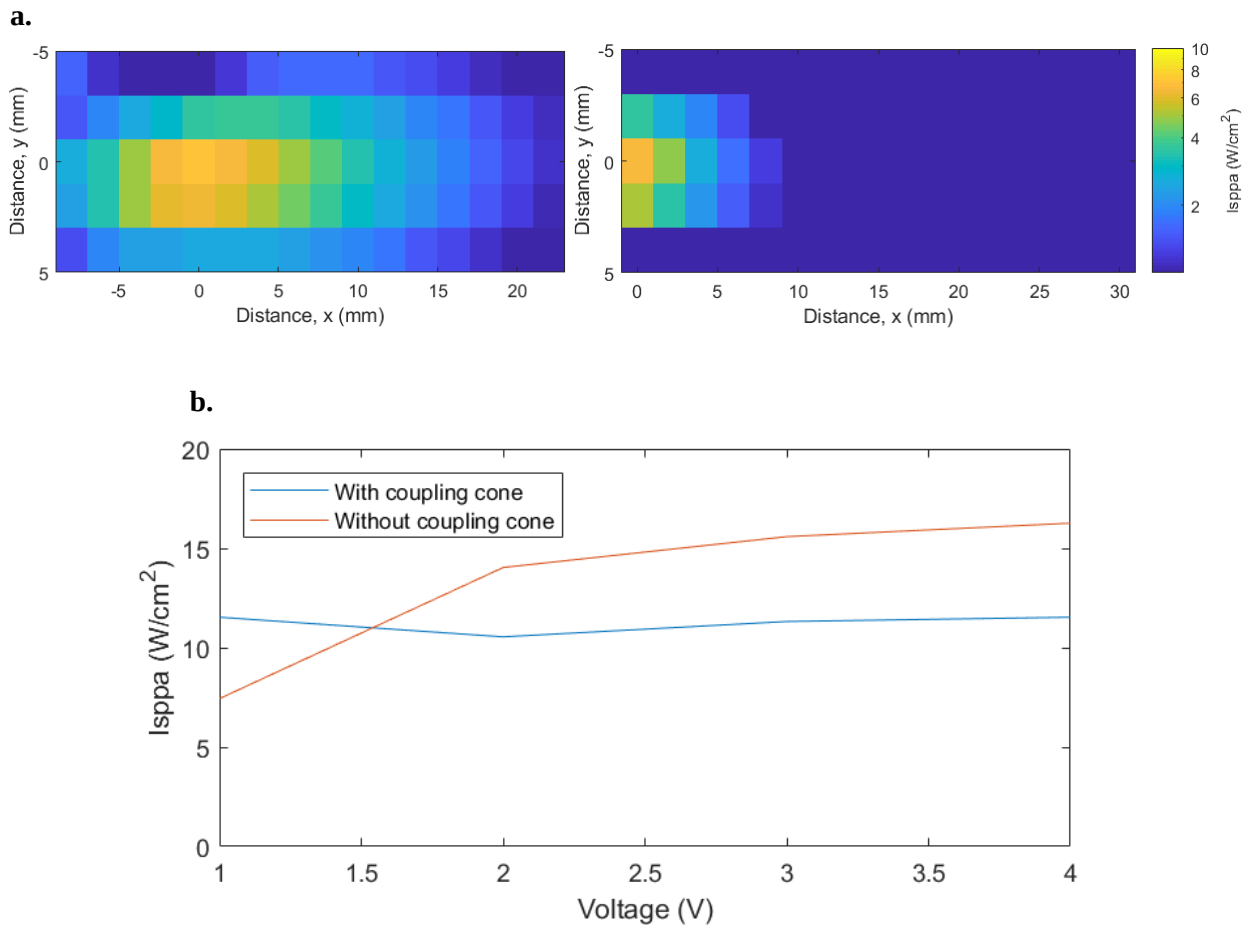

Figure B.2 – Results of hydrophone measurements for 1 MHz piezoelectric transducer (V303, Olympus) with and without coupling cone. **a)** Heatmap plots of I_{SPPA} at without (left) and with a coupling cone (right). Focal point is situated at x, y = (0, 0). Note that pressure measurements were not possible inside the cone. **b)** I_{SPPA} at the focal point as a function of voltage. The difference observed here can be explained by looking at a). The point of highest intensity is most likely contained within the coupling cone. Adjustments to the cone were made to ensure the availability of the focal point. Note that the actual voltage seen by the transducer is much higher due to amplification.

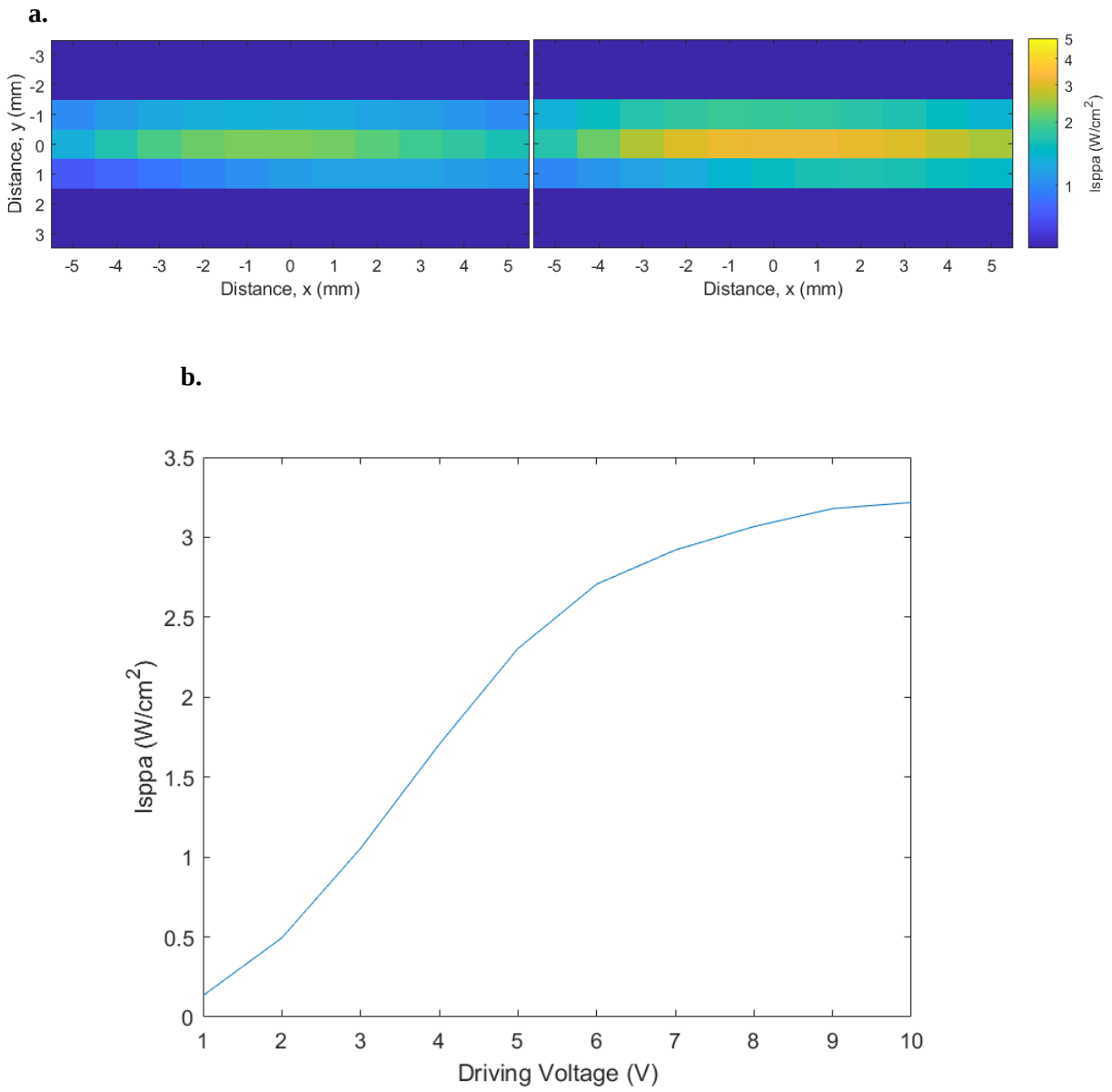

Figure B.3 – Results of hydrophone voltage sweep measurements (1V – 10V) for 1 MHz piezoelectric transducer (V303, Olympus). **a)** Heatmap plots of I_{SPPA} at 5V (left) and 10V (right). Focal point is situated at x, y = (0, 0). **b)** I_{SPPA} at the focal point as a function of voltage. Note that the actual voltage seen by the transducer is much higher due to amplification.

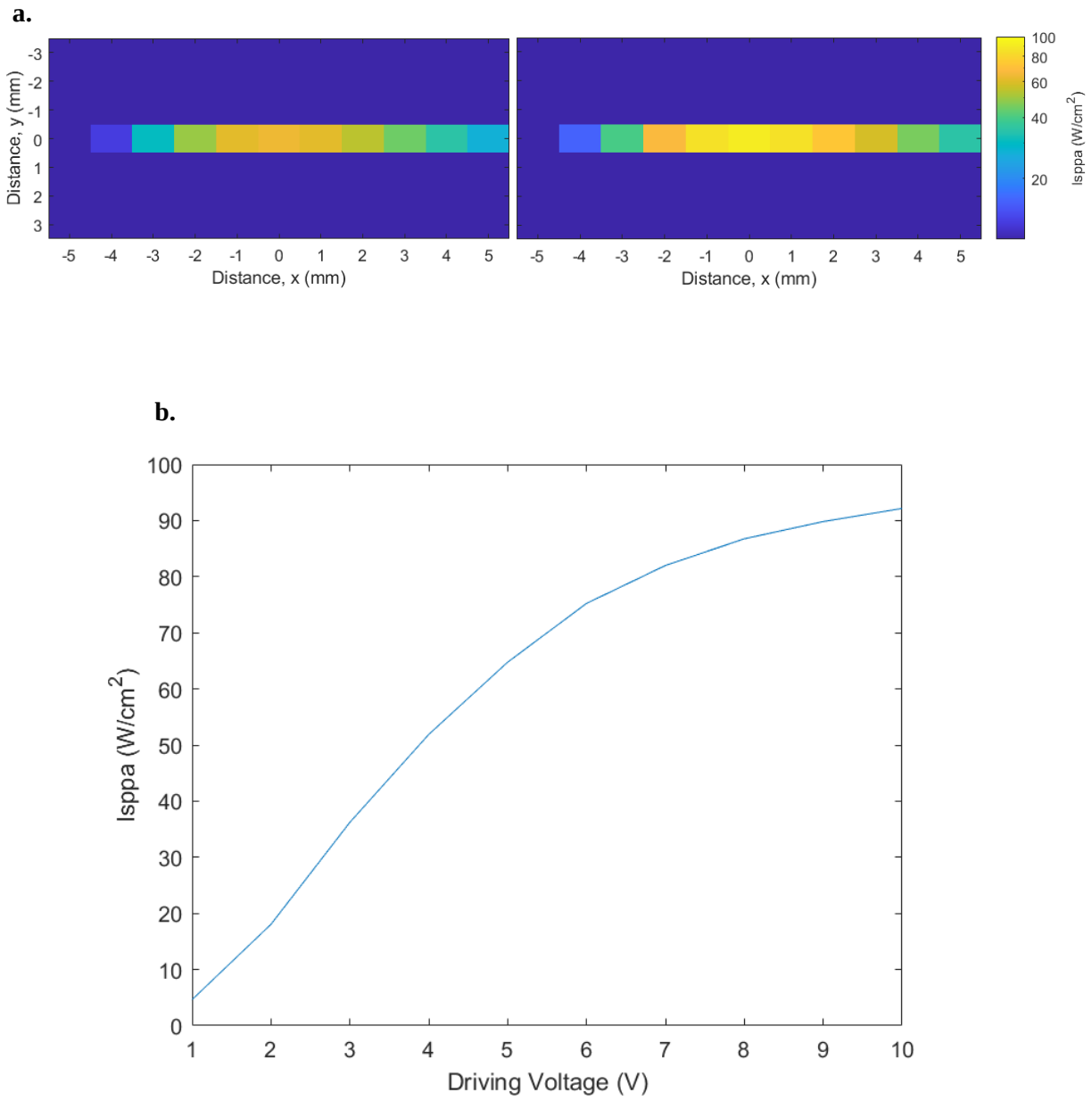

Figure B.4 – Results of hydrophone voltage sweep measurements (1V – 10V) for 5 MHz piezoelectric transducer (V310, Olympus). **a)** Heatmap plots of I_{SPPA} at 5V (left) and 10V (right). Due to the higher frequency, the 5 MHz probe has a narrower focal point than the 1 MHz probe. Focal point is situated at x, y = (0, 0). **b)** I_{SPPA} at the focal point as a function of voltage. Note that the actual voltage seen by the transducer is much higher due to amplification.

a.

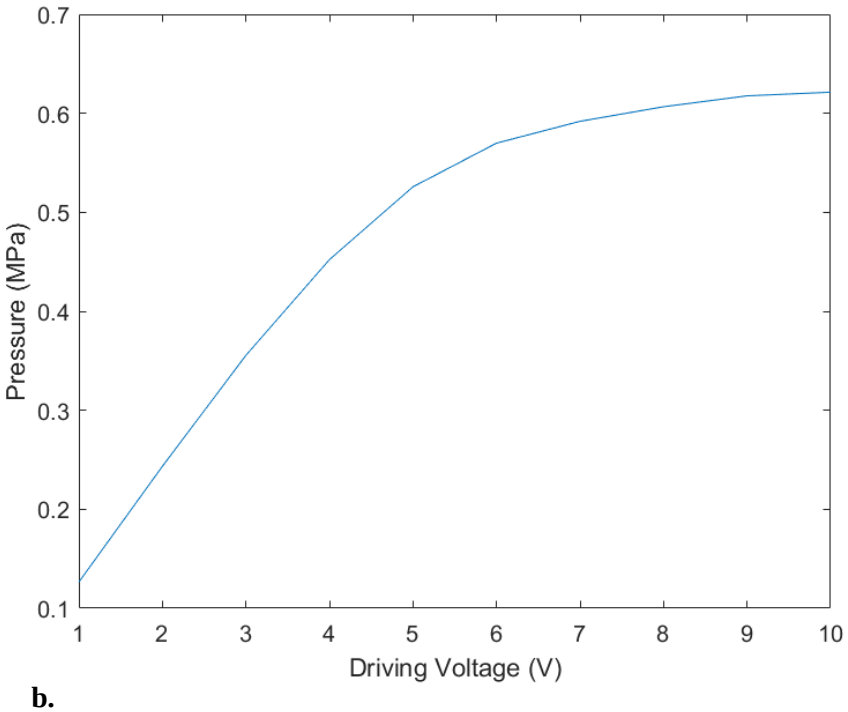

b.

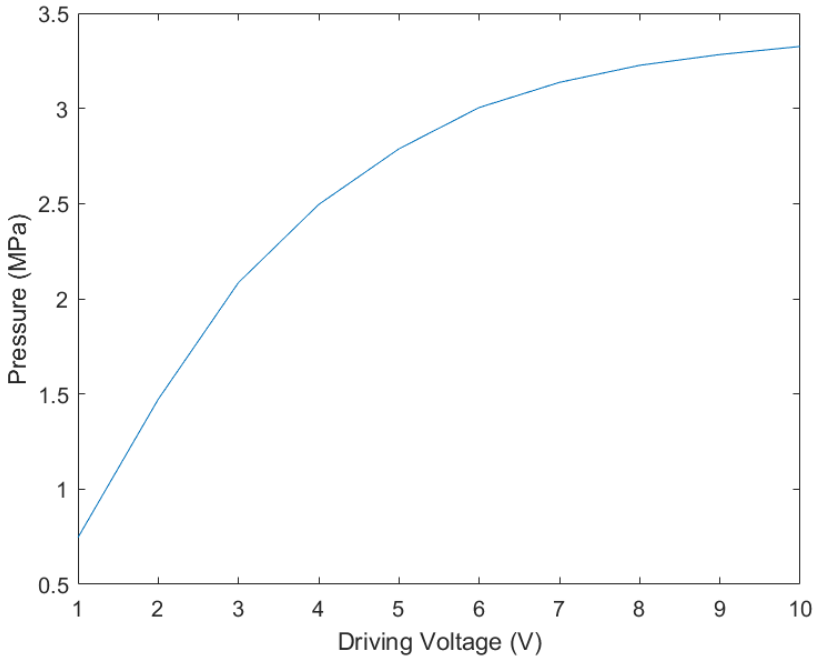

Figure B.5 – Results of hydrophone voltage sweep in pressure. **a)** Pressure versus supply voltage for 1 MHz probe. **a)** Pressure versus supply voltage for 5 MHz probe.

Appendix C: Lithography Masks

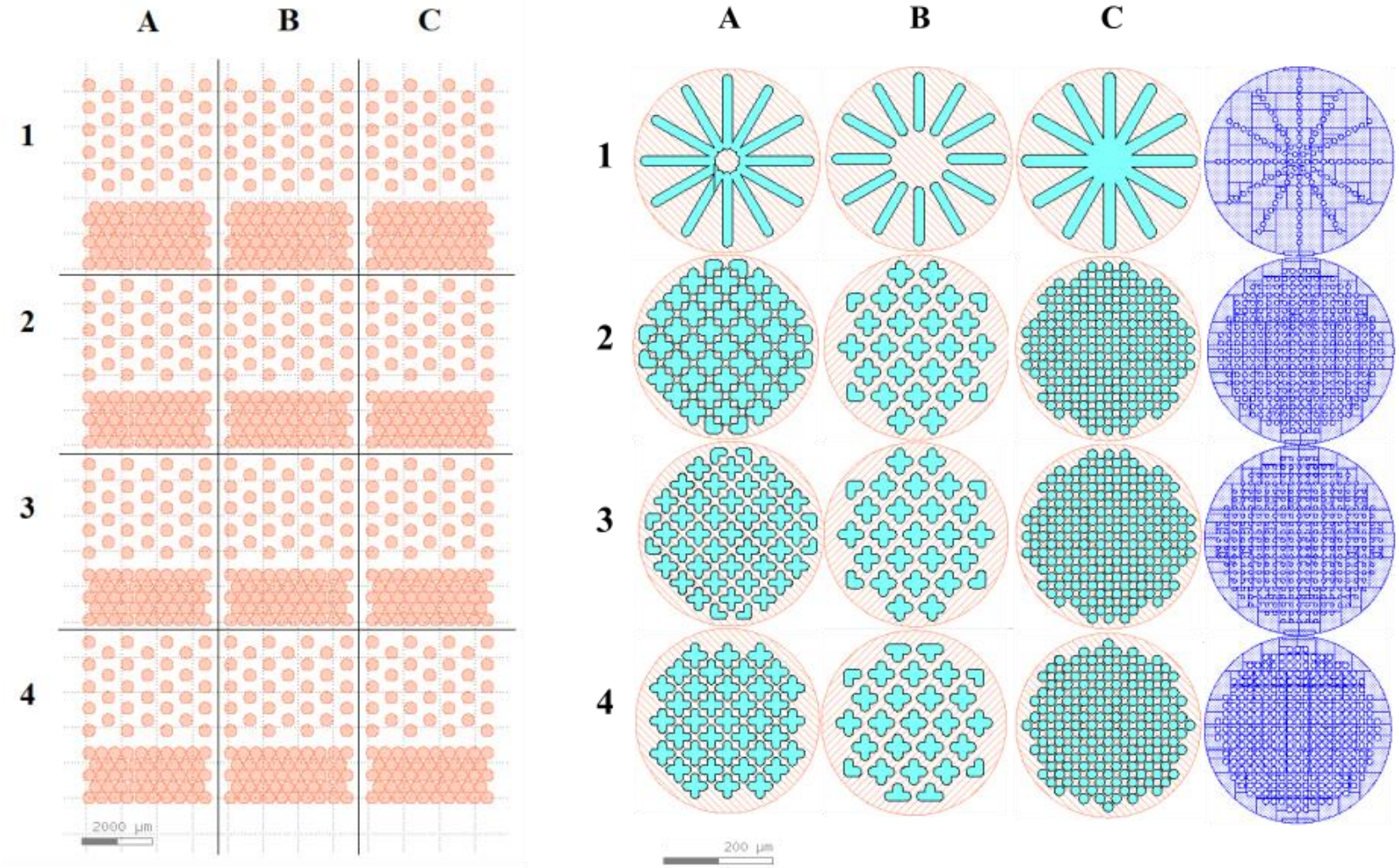

Figure C.1 – Left: Die layout for lithography masks. Each portion of the raster corresponds to a phase A structure and an embedded metal mask (blue masks, right). This results in a total of 12 different combinations of structures and embedded mask. The phase B etch mask is shown as striated circles behind phase A features.

Appendix D: Frontside Processing Cross-sections

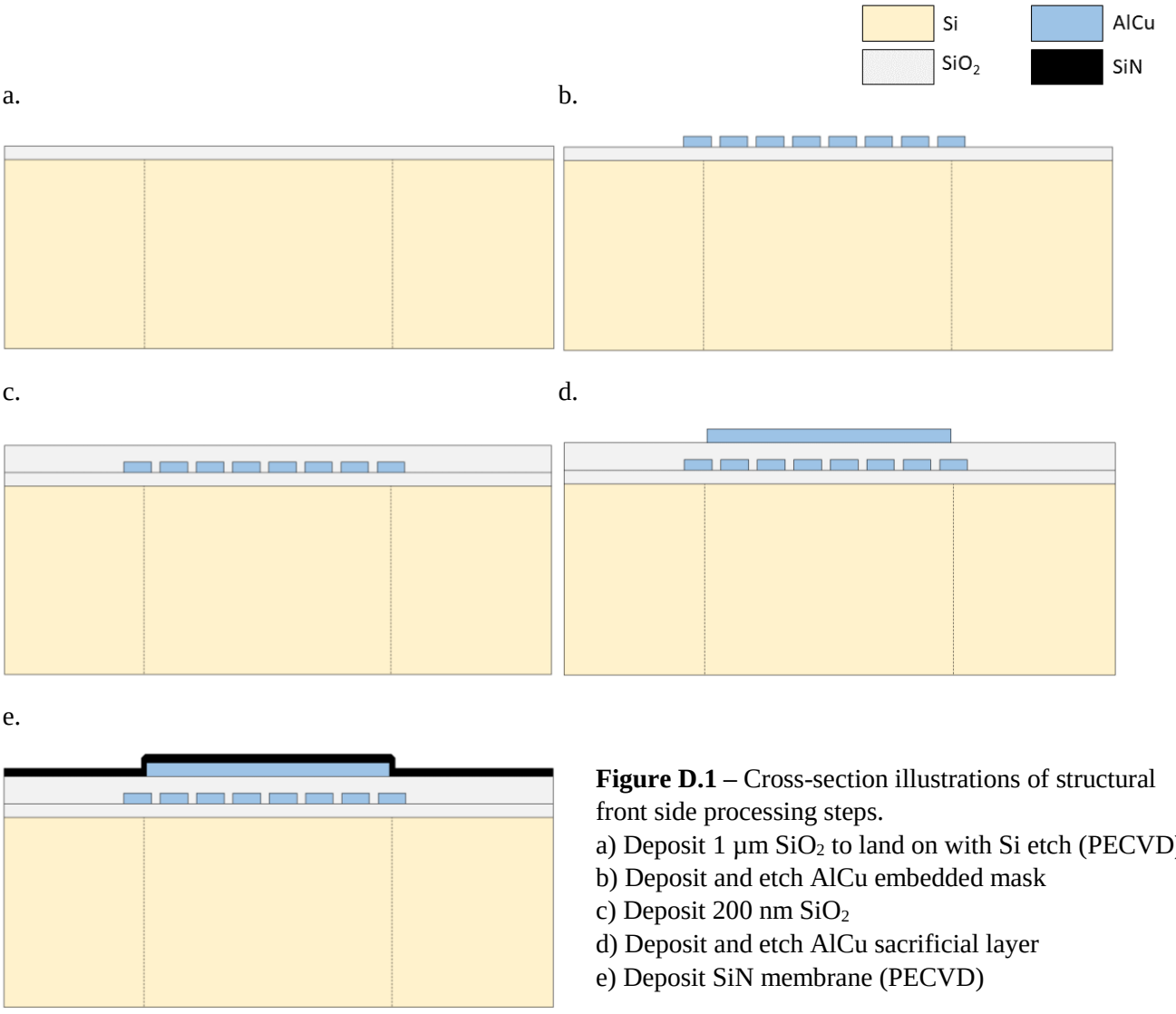

Figure D.1 – Cross-section illustrations of structural front side processing steps.
a) Deposit 1 µm SiO_2 to land on with Si etch (PECVD)
b) Deposit and etch AlCu embedded mask
c) Deposit 200 nm SiO_2
d) Deposit and etch AlCu sacrificial layer
e) Deposit SiN membrane (PECVD)

Appendix E: Backside Processing Cross-sections

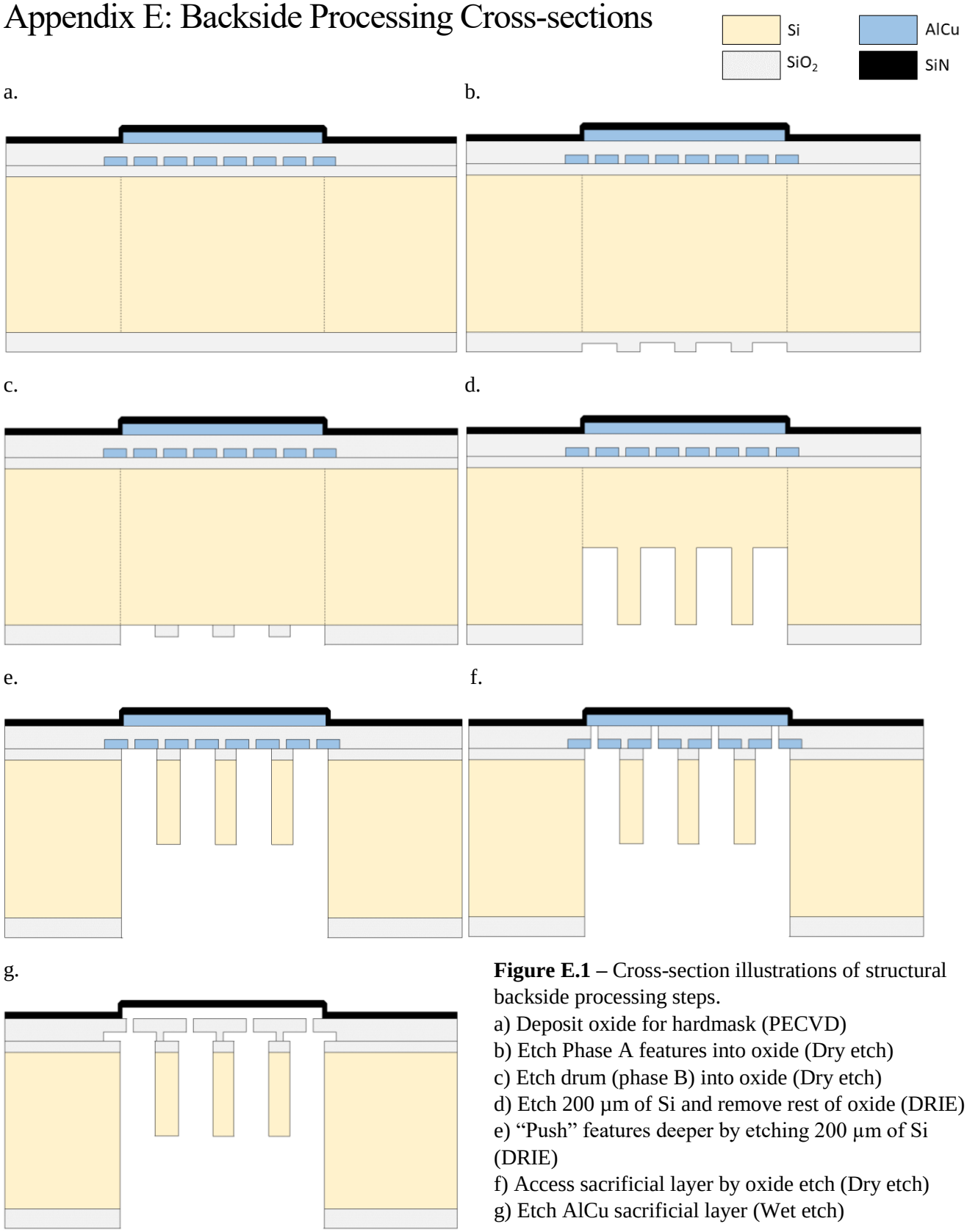

Figure E.1 – Cross-section illustrations of structural backside processing steps.
a) Deposit oxide for hardmask (PECVD)
b) Etch Phase A features into oxide (Dry etch)
c) Etch drum (phase B) into oxide (Dry etch)
d) Etch 200 µm of Si and remove rest of oxide (DRIE)
e) "Push" features deeper by etching 200 µm of Si (DRIE)
f) Access sacrificial layer by oxide etch (Dry etch)
g) Etch AlCu sacrificial layer (Wet etch)

References

Ahmad, M., Bozkurt, A., & Farhanieh, O. (2019). PMMA-Based Wafer-Bonded Capacitive Micromachined Ultrasonic Transducer for Underwater Applications. *Micromachines (Basel), 10*(5). doi:10.3390/mi10050319

Ai, L., Bansal, P., Mueller, J. K., & Legon, W. (2018). Effects of transcranial focused ultrasound on human primary motor cortex using 7T fMRI: a pilot study. *BMC Neurosci, 19*(1), 56. doi:10.1186/s12868-018-0456-6

Alvarez, O., & Latorre, R. (1978). Voltage-dependent capacitance in lipid bilayers made from monolayers. *Biophysical journal, 21*(1), 1-17.

Andersen, S. S., Jackson, A. D., & Heimburg, T. (2009). Towards a thermodynamic theory of nerve pulse propagation. *Progress in neurobiology, 88*(2), 104-113.

Bachtold, M. R., Rinaldi, P. C., Jones, J. P., Reines, F., & Price, L. R. (1998). Focused ultrasound modifications of neural circuit activity in a mammalian brain. *Ultrasound in medicine & biology, 24*(4), 557-565.

Bähring, R., & Bauer, C. K. (2014). Easy method to examine single nerve fiber excitability and conduction parameters using intact nonanesthetized earthworms. *Advances in physiology education, 38*(3), 253-264.

Bullock, T. H. (1945). Functional organization of the giant fiber system of Lumbricus. *Journal of Neurophysiology, 8*(1), 55-71.

Chapman, I., MacNally, N., & Tucker, S. (1980). Ultrasound-induced changes in rates of influx and efflux of potassium ions in rat thymocytes in vitro. *Ultrasound in medicine & biology, 6*(1), 47-49.

Colucci, V., Strichartz, G., Jolesz, F., Vykhodtseva, N., & Hynynen, K. (2009). Focused ultrasound effects on nerve action potential in vitro. *Ultrasound Med Biol, 35*(10), 1737-1747. doi:10.1016/j.ultrasmedbio.2009.05.002

Constans, C., Mateo, P., Tanter, M., & Aubry, J. F. (2018). Potential impact of thermal effects during ultrasonic neurostimulation: retrospective numerical estimation of temperature elevation in seven rodent setups. *Phys Med Biol, 63*(2), 025003. doi:10.1088/1361-6560/aaa15c

El Hady, A., & Machta, B. B. (2015). Mechanical surface waves accompany action potential propagation. *Nat Commun, 6*, 6697. doi:10.1038/ncomms7697

Erguri, A., Huang, Y., Zhuang, X., Oralkan, O., Yarahoglu, G. G., & Khuri-Yakub, B. T. (2005). Capacitive micromachined ultrasonic transducers: Fabrication technology. *IEEE transactions on ultrasonics, ferroelectrics, and frequency control, 52*(12), 2242-2258.

FDA. (2019). Marketing Clearance of Diagnostic Ultrasound Systems and Transducers.

Gavrilov, L. (1984). Use of focused ultrasound for stimulation of nerve structures. *Ultrasonics, 22*(3), 132-138.

Gavrilov, L. R., Gersuni, G. V., Ilyinski, O. B., Tsirulnikov, E. M., & Shchekanov, E. E. (1977). A study of reception with the use of focused ultrasound. I. Effects on the skin and deep receptor structures in man. *Brain Res, 135*(2), 265-277.

Guo, H., Hamilton, M., 2nd, Offutt, S. J., Gloeckner, C. D., Li, T., Kim, Y., . . . Lim, H. H. (2018). Ultrasound Produces Extensive Brain Activation via a Cochlear Pathway. *Neuron, 98*(5), 1020-1030 e1024. doi:10.1016/j.neuron.2018.04.036

Haller, M. I., & Khuri-Yakub, B. T. (1996). A surface micromachined electrostatic ultrasonic air transducer. *IEEE transactions on ultrasonics, ferroelectrics, and frequency control, 43*(1), 1-6.

Harvey, E. N. (1929). The Effect of High Frequency Sound Waves On Heart Muscle and Other Irritable Tissues

Hodgkin, A. L., & Huxley, A. F. (1952). A quantitative description of membrane current and its application to conduction and excitation in nerve. *The Journal of physiology, 117*(4), 500-544.

Huang, Y., Ergun, A., Haeggstrom, E., & Khuri-Yakub, B. (2002). *Fabrication of Capacitive Micromachined Ultrasonic Transducers (CMUTs) using wafer bonding technology for low frequency (10 kHz-150 kHz) sonar applications.* Paper presented at the OCEANS'02 MTS/IEEE.

Jérémy Vion-Bailly, W. A. N. D., Jean-Louis Mestas, Jean-Yves Chapelon. (2015). Feasibility and main mechanisms underlying in vivo ultrasound neurostimulation of the ventral nerve cord's giant axons of lumbricus terrestris.

Khedr, E. M., Kotb, H., Kamel, N. F., Ahmed, M. A., Sadek, R., & Rothwell, J. C. (2005). Longlasting antalgic effects of daily sessions of repetitive transcranial magnetic stimulation in central and peripheral neuropathic pain. *J Neurol Neurosurg Psychiatry, 76*(6), 833-838. doi:10.1136/jnnp.2004.055806

Khraiche, M. L., Phillips, W. B., Jackson, N., & Muthuswamy, J. (2008). *Ultrasound induced increase in excitability of single neurons.* Paper presented at the 2008 30th Annual International Conference of the IEEE Engineering in Medicine and Biology Society.

Knowles, K., & Van Helvoort, A. (2006). Anodic bonding. *International materials reviews, 51*(5), 273-311.

Lee, W., Chung, Y. A., Jung, Y., Song, I. U., & Yoo, S. S. (2016). Simultaneous acoustic stimulation of human primary and secondary somatosensory cortices using transcranial focused ultrasound. *BMC Neurosci, 17*(1), 68. doi:10.1186/s12868-016-0303-6

Legon, W., Ai, L., Bansal, P., & Mueller, J. K. (2018). Neuromodulation with single-element transcranial focused ultrasound in human thalamus. *Hum Brain Mapp, 39*(5), 1995-2006. doi:10.1002/hbm.23981

Lele, P. (1963). Effects of focused ultrasonic radiation on peripheral nerve, with observations on local heating. *Experimental Neurology, 8*(1), 47-83.

Menz, M. D., Ye, P., Firouzi, K., Nikoozadeh, A., Pauly, K. B., Khuri-Yakub, P., & Baccus, S. A. (2019). Radiation Force as a Physical Mechanism for Ultrasonic Neurostimulation of the Ex Vivo Retina. *J Neurosci, 39*(32), 6251-6264. doi:10.1523/JNEUROSCI.2394-18.2019

Menz, M. D., Ye, P., Firouzi, K., Pauly, K. B., Khuri-Yakub, B. T., & Baccus, S. A. (2017). Physical mechanisms of ultrasonic neurostimulation of the retina. doi:10.1101/231449

Merrill, D. R., Bikson, M., & Jefferys, J. G. (2005). Electrical stimulation of excitable tissue: design of efficacious and safe protocols. *J Neurosci Methods, 141*(2), 171-198. doi:10.1016/j.jneumeth.2004.10.020

Mihran, R. T., Barnes, F. S., & Wachtel, H. (1990). Temporally-specific modification of myelinated axon excitability in vitro following a single ultrasound pulse. *Ultrasound in medicine & biology, 16*(3), 297-309.

Mohammadjavadi, M., Ye, P. P., Xia, A., Brown, J., Popelka, G., & Pauly, K. B. (2019). Elimination of peripheral auditory pathway activation does not affect motor responses from ultrasound neuromodulation. *Brain Stimul, 12*(4), 901-910. doi:10.1016/j.brs.2019.03.005

Montgomery, J. C., & Macdonald, J. (1990). Effects of temperature on nervous system: implications for behavioral performance. *American Journal of Physiology-Regulatory, Integrative and Comparative Physiology, 259*(2), R191-R196.

Mueller, J., Legon, W., Opitz, A., Sato, T. F., & Tyler, W. J. (2014). Transcranial focused ultrasound modulates intrinsic and evoked EEG dynamics. *Brain Stimul, 7*(6), 900-908. doi:10.1016/j.brs.2014.08.008

Munhoz, R. P., Picillo, M., Fox, S. H., Bruno, V., Panisset, M., Honey, C. R., & Fasano, A. (2016). Eligibility Criteria for Deep Brain Stimulation in Parkinson's Disease, Tremor, and Dystonia. *Canadian Journal of Neurological Sciences / Journal Canadien des Sciences Neurologiques, 43*(4), 462-471. doi:10.1017/cjn.2016.35

Naor, O., Krupa, S., & Shoham, S. (2016). Ultrasonic neuromodulation. *Journal of neural engineering, 13*(3). doi:10.1088/1741-2560/13/3/031003

Ohl, C. D., Arora, M., Ikink, R., de Jong, N., Versluis, M., Delius, M., & Lohse, D. (2006). Sonoporation from jetting cavitation bubbles. *Biophys J, 91*(11), 4285-4295. doi:10.1529/biophysj.105.075366

Piech, D. K., Johnson, B. C., Shen, K., Ghanbari, M. M., Li, K. Y., Neely, R. M., . . . Muller, R. (2020). A wireless millimetre-scale implantable neural stimulator with ultrasonically powered bidirectional communication. *Nat Biomed Eng, 4*(2), 207-222. doi:10.1038/s41551-020-0518-9

Prieto, M. L., Oralkan, Ö., Khuri-Yakub, B. T., & Maduke, M. C. (2013). Dynamic response of model lipid membranes to ultrasonic radiation force. *PLoS One, 8*(10).

Qin, P., Xu, L., Hu, Y., Zhong, W., Cai, P., Du, L., . . . Yu, A. C. (2014). Sonoporation-induced depolarization of plasma membrane potential: analysis of heterogeneous impact. *Ultrasound Med Biol, 40*(5), 979-989. doi:10.1016/j.ultrasmedbio.2013.11.024

Sato, T., Shapiro, M. G., & Tsao, D. Y. (2018). Ultrasonic Neuromodulation Causes Widespread Cortical Activation via an Indirect Auditory Mechanism. *Neuron, 98*(5), 1031-1041.e1035. doi:10.1016/j.neuron.2018.05.009

Shannon, K. M., Gage, G. J., Jankovic, A., Wilson, W. J., & Marzullo, T. C. (2014). Portable conduction velocity experiments using earthworms for the college and high school neuroscience teaching laboratory. *Advances in physiology education, 38*(1), 62-70. Retrieved from https://www.physiology.org/doi/pdf/10.1152/advan.00088.2013

Stillings, D. (1971). The first use of electricity for pain treatment. *Medtronic Archive on Electro-Stimulation*.

Storey, K. G. (1989). Cell lineage and pattern formation in the earthworm. *Development, 107*(3), 519-531.

Taylor, G. J., Heberle, F. A., Seinfeld, J. S., Katsaras, J., Collier, C. P., & Sarles, S. A. (2017). Capacitive detection of low-enthalpy, higher-order phase transitions in synthetic and natural composition lipid membranes. *Langmuir, 33*(38), 10016-10026.

Tsui, P. H., Wang, S. H., & Huang, C. C. (2005). In vitro effects of ultrasound with different energies on the conduction properties of neural tissue. *Ultrasonics, 43*(7), 560-565. doi:10.1016/j.ultras.2004.12.003

Tyler, W. J., Tufail, Y., Finsterwald, M., Tauchmann, M. L., Olson, E. J., & Majestic, C. (2008). Remote excitation of neuronal circuits using low-intensity, low-frequency ultrasound. *PLoS One, 3*(10), e3511. doi:10.1371/journal.pone.0003511

Vion-Bailly, J., N'Djin, W. A., Suarez Castellanos, I. M., Mestas, J. L., Carpentier, A., & Chapelon, J. Y. (2019). A causal study of the phenomenon of ultrasound neurostimulation applied to an in vivo invertebrate nervous model. *Sci Rep, 9*(1), 13738. doi:10.1038/s41598-019-50147-7

Wahab, R. A., Choi, M., Liu, Y., Krauthamer, V., Zderic, V., & Myers, M. R. (2012). Mechanical bioeffects of pulsed high intensity focused ultrasound on a simple neural model. *Med Phys, 39*(7), 4274-4283. doi:10.1118/1.4729712

Westhoek, Y. (2020). Ultrasound Energy Transfer using Charged CMUTs. *TU Delft Repository*.

Wu, J. (2018). Acoustic Streaming and Its Applications. *Fluids, 3*(4). doi:10.3390/fluids3040108

Ye, P. P., Brown, J. R., & Pauly, K. B. (2016). Frequency Dependence of Ultrasound Neurostimulation in the Mouse Brain. *Ultrasound Med Biol, 42*(7), 1512-1530. doi:10.1016/j.ultrasmedbio.2016.02.012

Yoshida, K., Kurstjens, G. A. M., & Hennings, K. (2009). Experimental validation of the nerve conduction velocity selective recording technique using a multi-contact cuff electrode. *Medical Engineering & Physics, 31*(10), 1261-1270. doi:10.1016/j.medengphy.2009.08.005

Young, R. R., & HENNEMAN, E. (1961). Reversible block of nerve conduction by ultrasound: Ultrasonic blocking of nerve fibers. *Archives of neurology, 4*(1), 83-89.